# BEHAVIOUR OF PARTIALLY GROUTED NOMINALLY REINFORCED MASONRY SHEAR WALLS UNDER DYNAMIC LOADING

BY

TOMAS KASPARIK

B.Eng.

# BEHAVIOUR OF PARTIALLY GROUTED NOMINALLY REINFORCED MASONRY SHEAR WALLS UNDER DYNAMIC LOADING

By

TOMAS KASPARIK
B.Eng.

A Thesis
Submitted to the School of Graduate Studies
in Partial Fulfillment of the Requirements
For the Degree
**Master of Applied Science**

McMaster University

| | |
|---|---|
| MASTER OF APPLIED SCIENCE (2009)<br>(Civil Engineering) | McMaster University<br>Hamilton, Ontario |
| TITLE: | Behaviour of Partially Grouted Nominally Reinforced Masonry Shear Walls under Dynamic Loading |
| AUTHOR: | Tomas Kasparik, B.Eng. (McMaster University) |
| SUPERVISORS: | Dr. M. J. Tait<br>Dr. W. W. El-Dakhakhni |
| NUMBER OF PAGES: | xx, 189 |

# ABSTRACT

The current Canadian masonry standard CSA S304.1 (2004) deals with the design of unreinforced and reinforced concrete masonry shear walls. The use of one or the other type of wall construction is limited to a particular seismic activity zone based on the seismic hazard index. The code does not provide any provisions for partially grouted shear walls in regions with moderate seismic demand. The experimental program described in the thesis focuses on the dynamic performance of partially grouted nominally reinforced concrete masonry shear walls having less steel and larger spacing than specified by the Canadian masonry standard for the minimum seismic requirements.

A total of six reduced scale shear walls were designed and constructed to fail in flexure. A constant axial load was present throughout the test, which represented a single story building. The walls were grouped into three categories, Type I, II and III. Type I and III walls had reinforcement present only at the ends of the wall with vertical reinforcement ratios of 0.12% and 0.20%, respectively. Type II walls had an additional reinforcement located mid-length of the wall with a reinforcement ratio of 0.17%. Two identical walls were tested for each type with the exception of the Type III, where only one wall was tested. The walls were subject to dynamic loading of a scaled 1940 El-Centro earthquake N-S component. The experimental results were evaluated and discussed pertaining to behaviour, lateral load capacity, stiffness, period, displacement ductility and load reduction factors.

The general behaviour of the tested shear walls was dominated by rocking motion where a full length mortar joint crack developed, along with the yielding of reinforcement. The rocking motion was able to dissipate energy instead of the more common diagonal cracking and crushing of masonry. Type I and II walls had yields close the predicted values, while Type III wall had a lower yield point than predicted. All walls had similar trends of stiffness degradation. The period increased by a factor of 2 or more during the course of testing. An idealized bilinear envelope was used to calculate the displacement ductility. It was found to be greater than 2 with load reduction factors ranging from 1.9 to 2.6.

It was concluded that nominally reinforced partially grouted walls are potentially viable to be used in seismic zones where the seismic hazard index exceeds 0.35.

# DEDICATIONS

To my beloved Mother and Father

And

To the love of my life, Francesca

# ACKNOWLEDGEMENTS

I would like to express my sincere gratitude to Dr. M.J. Tait and Dr W.W. El-Dakhakhni for their patience, guidance and encouragement throughout my research as well as their assistance with the completion of my manuscript.

Acknowledgement is due to McMaster University, the Department of Civil Engineering and the Center for Effective Design of Structures for their financial support that made it possible for me to complete graduate studies. Acknowledgements are also extended to Canadian Masonry Design Centre for providing a mason to construct specimens over several days, to Canadian Concrete Masonry Producers Association for providing reduced scale masonry blocks and Blok-Lok Ltd. for donating wire used as vertical reinforcement.

Much appreciation to Niel Van Engelen for his assistance and help during the summer months with the setup and testing. Sincere thanks to David Perrett, Kent Wheeler, Rhys Westmoreland and Peter Koudys for their advice and assistance throughout the experimental program.

I would like to thank my parents who supported me not only through my professional studies but also my personal endeavours. Last, certainly not the least, I would like to say thank you to the love of my life, Francesca, who has shown compassion, love and support throughout these past years. Without her support, none of this would have been possible.

# TABLE OF CONTENTS

CHAPTER 1: INTRODUCTION

CHAPTER 2: EXPERIMENTAL PROGRAM

CHAPTER 3: EXPERIMENTAL RESULTS

CHAPTER 4: ANALYSIS

CHAPTER 5: SUMMARY AND CONCLUSIONS

APPENDIX

# LIST OF FIGURES

# LIST OF TABLES

# LIST OF SYMBOLS

| | |
|---|---|
| $A_e$ | Effective cross-sectional area of masonry |
| $A_g$ | Gross cross-sectional area of masonry |
| $A_{sc}$ | Area of vertical steel in compression |
| $A_s$ | Area of vertical steel in tension |
| $A_v$ | Area of horizontal steel |
| $b_w$ | Thickness of masonry wall |
| c | Distance from the extreme compression fibre to the neutral axis |
| C | Compression force |
| d | Distance from extreme compression fibre to centroid of vertical reinforcement |
| $d_u, d_y$ | Maximum post yield and yield displacements respectively |
| $d_v$ | Effective depth, need not be taken less than $0.8\ell_w$ |
| $E_m$ | Modulus of elasticity of masonry |
| $E_s$ | Modulus of elasticity of steel reinforcement |
| F, L, T | Fundamental dimensions of force, length and time |
| $F_a$ | Acceleration based site coefficient |
| $f_{cs}$ | Axial compressive stress |
| $f'_m$ | Compressive strength of masonry |
| $f_n$ | Natural frequency |
| $f_s$ | Stress of vertical reinforcement below yield stress |
| $f_t$ | Flexural tensile strength of masonry |
| $f_y$ | Yield strength of reinforcement |
| $G_m$ | Shear modulus |
| h | Height from the base of the wall to the center-of-gravity of the mass |
| $h_w$ | Height of wall |
| $I_E$ | Earthquake important factor of the structure |
| $I_E F_a S_a(0.2)$ | Seismic hazard index |
| $I_{initial}, I_{cr}$ | Initial (uncracked) and cracked moment of inertia respectively |
| $k_{initial}, k_{cr}$ | Initial (uncracked) and cracked stiffness of wall respectively |
| $k_m$ | Factor relating modulus to the compressive stress of masonry |
| kd | Depth of compression zone of a cracked cross-section |
| $\ell_w$ | Length of wall |
| m | Mass on top of wall |
| $m_p$ | Mass of prototype |
| $M_{cr}$ | Cracked moment capacity |
| $M_f$ | Moment from loading |
| $M_y$ | First yield moment capacity |
| $M_u$ | Ultimate moment capacity |
| $P_2$ | Compressive force acting normal to the sliding plane plus the tensile force at yield of vertical reinforcement |

| | |
|---|---|
| $P_d$ | Axial compressive load |
| $R_d$ | Load reduction factor |
| $s$ | Spacing of horizontal reinforcement |
| $S_a(0.2)$ | 5% damped spectral response acceleration at a period of 0.2 s |
| $S_i$ | Scale factor of a given quantity, i, given in Table 1.1 |
| $t$ | Time |
| $T$ | Tension force |
| $T_n$ | Natural period |
| $V$ | Lateral load resistance of the wall |
| $V_{cr}$ | Cracked shear capacity |
| $V_f$ | Shear from loading |
| $V_m$ | Shear strength of masonry wall provided by the horizontal steel |
| $V_r$ | Shear resistance of wall |
| $V_s$ | Shear strength of masonry wall provided by the masonry |
| $V_u$ | Ultimate lateral load capacity calculated from moment capacity |
| $V_y$ | First yield lateral load capacity |
| $u(t)$ | Displacement response |
| $y_t$ | Distance from neutral axis to the extreme compression fibre |
| $\beta_1$ | Ratio of depth of rectangular compression block to the depth of neutral axis |
| $\gamma_g$ | Factor to account for partially grouted walls |
| $\Delta_f, \Delta_s$ | Deflections due to moment and shear |
| $\Delta G$ | Additional mass to satisfy dynamic model |
| $\varepsilon_s$ | Strain of steel reinforcement below yield |
| $\varepsilon_u$ | Ultimate masonry strain |
| $\varepsilon_y$ | Yield strain of steel reinforcement |
| $\zeta$ | Critical damping coefficient |
| $\mu$ | Coefficient of friction |
| $\mu_\Delta$ | Displacement ductility |
| $v_m$ | Shear strength of masonry |
| $\pi_{np}, \pi_{np}$ | Non-dimensional products of the prototype and model |
| $\rho_v$ | Vertical reinforcing ratio |
| $\sigma_{gross}, \sigma_{net}$ | Gross and net cross-sectional area axial stress |
| $\sigma_y$ | Yield strength of reinforcement |
| $\phi_m$ | Resistance factor for masonry |
| $\phi_s$ | Resistance factor for reinforcing bars |
| $\chi$ | Factor to account for direction of compressive stress |
| $\omega_n, \omega_D$ | Natural and damped circular frequency |

# CHAPTER 1: INTRODUCTION

## 1.1 Introduction

Masonry is one of the oldest construction materials. It can resist large compressive forces and environmental impacts, making it very effective for construction. Masonry has been used to construct both public and residential buildings. Past masonry design and construction techniques did not account for seismic forces, which make masonry buildings perhaps the most susceptible to earthquake damage.

In addition to carrying gravity loads to the foundation, the main role of shear walls is to resist lateral loads due to wind and seismic forces. They have been popular in building design because of their large lateral stiffness and load resistance. During an earthquake, the walls are subject to both in-plane and out-of-plane lateral forces. The strength of masonry buildings is primarily provided by the in-plane shear/flexural resistance of the shear walls.

Although shear walls provide resistance to lateral shear loads, the name itself is somewhat misleading. Shear walls develop bending forces, as well as shear forces that are transmitted to the foundation. It is favourable for shear walls to fail in flexure as this is a ductile failure mode compared to the more brittle shear failure.

A better understanding of dynamic behaviour of masonry structures and components is needed in order to construct more economical and safer buildings. One approach to quantify seismic performance is to perform full scale testing of buildings under simulated earthquakes. However, this may not be practical due to space and test equipment limitations; thus, testing must be carried out on reduced scale structures. Once a model length scale is selected to mimic its full scale counterpart, dimensional analysis must be used to determine the scale factors for different physical quantities. Construction of reduced scale models have been proven to be effective in experimental masonry programs as an alternative to full scale testing (Mirza et al. 1979).

## 1.2 Shear Wall Behaviour

Several experimental investigations have been carried out focusing on the behaviour of in-plane concrete masonry shear walls. The behaviour of shear walls was found to be dependent upon several factors including:

- The amount and distribution of vertical and horizontal reinforcement;
- Level of applied axial load;
- Wall aspect ratio (height / length);
- Strength of the materials used in wall construction

The result of the varied parameters in experimental programs subjected to axial and lateral loads identified three types of failure modes; flexural, shear and sliding [Drysdale et al. (2005) and Voon (2007)]. The failures are shown in Figure 1.1.

### 1.2.1 Shear Failure

This type of failure mechanism is characterized by diagonal tension and compression cracking. It is undesirable for walls to fail in shear as it is a brittle type of failure, occurring without warning. The stiffness degradation of walls failing in shear is relatively large compared to that of walls failing in flexure (Drysdale et al. 2005).

The horizontal reinforcement shares in carrying the load before the onset of diagonal cracking. However, once diagonal cracks occur, the shear resistance is solely carried by the horizontal steel bars. When adequate shear reinforcement is provided, diagonal cracks do not open up excessively and they are able to distribute evenly across the wall.

Axial compressive load contributes to the masonry shear strength by enhancing the aggregate interlocking mechanism, which delays the initial cracking of masonry. The ductility of shear dominated walls is typically very limited and depends on the horizontal steel reinforcement ratio. In addition, a uniform reinforcement distribution will increase shear strength, facilitate better control of diagonal cracking and improve energy dissipation of the wall during cyclic loading.

According to the Canadian masonry design standard, CSA S304.1 (2004), the equations for calculating shear strength of reinforced masonry are:

$$V_r = V_m + V_s \qquad \text{Eq. 1.1}$$

$$V_r = \phi_m(v_m b_w d_v + 0.25P_d)\gamma_g + \phi_s\left(0.60A_v f_y \frac{d_v}{s}\right) \qquad \text{Eq. 1.2}$$

$$V_{r\,max} = 0.4\phi_m\sqrt{f'_m}b_w d_v \gamma_g \qquad \text{Eq. 1.3}$$

where $v_m = 0.16\left(2 - \frac{M_f}{V_f d_v}\right)\sqrt{f'_m}$

with $\frac{M_f}{V_f d_v} \geq 0.25$ and $\leq 1$

The in-plane shear resistance, $V_r$, is determined as the sum of the contributions from masonry,$V_m$, and steel, $V_s$. The shear strength of masonry is dependant on $v_m$, multiplied by $b_w$ and $d_v$, which accounts for the thickness of the wall and the effective depth, respectively, where the effective depth is not less than $0.8\ell_w$ (length of the wall). The axial compressive load, $P_d$, is multiplied by a factor of 0.25. The $\gamma_g$ factor accounts for the use of partially grouted or ungrouted shear walls. It is equal to 1 for fully grouted walls and fully filled mortar joints; otherwise, it is the ratio of $A_e/A_g$ but not greater than 0.5. A value of 0.5 is used because the non-solid sections provide a potential weak path for diagonal cracks. The effective area, $A_e$, is defined as the mortared and grouted section area of the wall and $A_g$ is the total gross section area of the wall. The shear contribution from horizontal reinforcement has additional factors, $f_y$ and s. These are defined as the yield strength and the spacing of the horizontal reinforcement, respectively. The term $M_f/(V_f d_v)$ accounts for the influence of flexural cracking on the shear strength, where $M_f$ and $V_f$ are the moment and shear at the section considered. The compressive strength of masonry is defined as $f'_m$. Resistance factors for masonry, $\phi_m$ and steel, $\phi_s$, are applied in design and are equal to 0.60 and 0.85, respectively.

Equation 1.3 restricts the maximum shear force used in design. For squat shear walls with low aspect ratio, the shear limit can be increased (Eq. 1.4) due to the potential of the wall having increased shear strength. The aspect ratio of the wall must be between 0.5 and 1.

$$V_{r\,\max} = 0.4\phi_m\sqrt{f'_m}b_w d_v \gamma_g \left(2 - \frac{h_w}{l_w}\right) \qquad \text{Eq. 1.4}$$

### 1.2.2 Flexural Failure

Flexural failure is characterized by the yielding of the vertical reinforcement, crushing of masonry near the wall toe and bed-joint cracking. Generally, this is the preferred failure mode, particularly under seismic loads, as the type of failure is ductile with the ability to effectively dissipate energy. A cantilever wall failing in flexure can withstand large inelastic deformations without significant loss of stiffness and strength. Shing et al. (1989) investigated the effect of applied axial load on the behaviour of reinforced masonry shear walls. From the test results, it was concluded that the applied axial load can change the behaviour of walls from a mixed flexure/shear to a more brittle shear failure mode. Although the applied axial load has the effect of increasing the flexural capacity and stiffness, the ductility is decreased due to the delayed yielding of tensile reinforcement and crushing of masonry.

The flexural strength of a vertically reinforced masonry wall is calculated by means of simple flexure theory. This theory is based on the assumption that plane sections remain plane after bending. According to the Canadian masonry design code, CSA S304.1 (2004), the equations for calculating flexural strength are:

$$P_d = C - \sum T \quad \text{Eq. 1.5}$$

$$P_d = \phi_m 0.85\chi f'_m b_w \beta_1 c - \sum_{i=1}^{n} \phi_s A_{si} f_{si} \quad \text{Eq. 1.6}$$

where $\beta_1 = 0.8 - 0.1\left(\frac{f'_m - 20}{10}\right) \leq 0.8$

$$M_u = \phi_m 0.85\chi f'_m b_w \beta_1 c\left(\frac{l_w}{2} - \frac{\beta_1 c}{2}\right) + \sum_{i=1}^{n}\left[\phi_m A_{si} f_{si}\left(d_i - \frac{l_w}{2}\right)\right] \quad \text{Eq. 1.7}$$

$$V_u = M_r / h \quad \text{Eq. 1.8}$$

where strain compatibility: $f_{si} = E_s \varepsilon_u \frac{d_i - c}{c}$ for $f_{si} < f_y$ Eq. 1.9

$$f_{si} = E_s \varepsilon_y \text{ for } \varepsilon_{si} \geq \varepsilon_y \quad \text{Eq. 1.10}$$

Using the force equilibrium equation (Eq. 1.5 and 1.6), the distance, c, from the extreme compression fibre to the neutral axis is calculated based on the axial load, $P_f$, the compression force from the masonry, C and the tension force due to the steel, T. The masonry compressive force is determined from the compressive strength of masonry, $f'_m$, the width of the wall, $b_w$ and the equivalent rectangular stress block, $\beta_1 c$. For walls having continuous and uninterrupted grout, $\chi$ is equal to unity, which is always the case for walls. The steel compressive force is determined from the area of the steel, $A_s$ and its corresponding yield strength, $f_s$. Resistance factors for masonry, $\phi_m$ and steel, $\phi_s$, are applied in design and are equal to 0.60 and 0.85, respectively.

The ultimate moment resistance of the wall is calculated from the moment equilibrium about the centroid of the wall (Eq. 1.7). The length of the wall is defined as $\ell_w$ and the position of the steel reinforcement from the extreme compression fibre is defined as $d_i$. The lateral shear resistance is calculated by dividing the moment resistance by the height of the wall (Eq. 1.8). The force in the reinforcement steel depends upon its strain, which is calculated by its location from the neutral axis, c. Equation 1.9 is applicable to bars that have not yielded. The strain obtained from Eq. 1.9 is multiplied by the elastic modulus, $E_s$, to find the corresponding strength, $f_s$. Equation 1.10 is applicable when the strain of the reinforcement bar is larger than its yield strain, $\varepsilon_y$.

### 1.2.3 Sliding Failure

Sliding failure is characterized by the movement of parts of the wall or the whole wall over a mortar bed joint or its base. It is resisted by the dowel action of the vertical reinforcement and by friction due to axial load. This type of failure may occur when there is a low friction coefficient between the wall and its base or when there is inadequate dowel resistance from vertical steel reinforcement (e.g. unreinforced masonry shear walls). Equation 1.11 is used to determine sliding shear strength (Drysdale et al. 2005).

$$V_r = \emptyset_m \mu P_2 \qquad \text{Eq. 1.11}$$

The sliding resistance has two factors contributing to the overall resistance. The first factor is the coefficient of friction between the sliding plane of the two materials in question, μ, and the second factor, $P_2$, is the total force from the axial load and tensile force of the vertical reinforcement or dowels (if present at the base).

## 1.3 Research Significance and Objectives

The current Canadian masonry design standard, CSA S304.1 (2004), deals with only unreinforced and reinforced shear walls. Unreinforced concrete masonry walls have been used extensively in low-rise building construction where seismic activity is limited. On the other end of the spectrum are reinforced concrete masonry walls, which were an improvement upon unreinforced walls by introducing reinforcing steel bars. The use of reinforcement increased the overall ductility and energy dissipating characteristics.

The code does not provide any provisions pertaining to design of concrete masonry walls that fall in between the unreinforced and reinforced categories; specifically, partially grouted nominally reinforced masonry walls. Nominally reinforced masonry walls are defined as having less area of steel and larger spacing than specified in Clause 10.15.2 by the CSA S304.1 (2004), for a seismic hazard index ($I_E F_a S_a(0.2)$) equal or greater to 0.35. Masonry shear walls must be reinforced horizontally and vertically with a minimum total steel area of $0.002A_g$ and distributed in each direction with a minimum area of $0.00067A_g$. The spacing of the reinforcement is not to exceed six times the nominal thickness of the wall or 1,200 mm, whichever is less.

A reinforced wall in a seismic zone with a seismic hazard index equal or greater to 0.35 must be fully grouted but not necessarily fully reinforced, as long as the spacing and area requirements are satisfied. The use of partially grouted masonry is not permitted to be used in these seismic zones. However, the literature indicates that the use of partially grouted masonry has yielded good results. These provisions of reinforcement area, spacing and partial grouting limits the construction of masonry walls to reinforced walls only, although, it may be possible that the same target performance in specific regions can be accomplished with the use of partially grouted nominally reinforced walls.

The experimental program carried out in the thesis focuses on the performance of partially grouted nominally reinforced concrete masonry shear walls having less steel and larger spacing than specified by the CSA S304.1 (2004) for seismic requirements. Reduced scale walls were constructed to study their behaviour under dynamic loading of the 1940 El-Centro earthquake N-S component. Key aspects of the wall were examined pertaining to in-plane lateral load carrying capacity, stiffness, period, displacement ductility and load reduction factors. The results from this study are intended to contribute to the research on partially grouted and nominally reinforced shear walls by introducing new supporting evidence based on dynamic testing.

## 1.4 Literature Review

### 1.4.1 Small Scale Modeling

#### 1.4.1.1 Small Scale Structural Models

A structural model is defined as a physical representation of a structure or a structural component built usually to a reduced scale for which laws of similitude are applied. Structural models have been very useful and in some cases necessary due to the size of the prototype structure being studied. A prototype is defined as a full scale structure or structural component. The use of reduced scale models also depends on the type of loading being studied. When dynamic loading is to be used, a reduced scale model of the prototype structure may need to be constructed due to the limitations of the shake table capacity.

There are a number of structural models used in research depending on the intended function. To study the complete behaviour of a structure or a structural component, including the elastic and inelastic behaviour up to failure, a strength model is utilized, which by definition, is also a direct model (Harris and Sabnis 1999). A strength model is also called a realistic model or replica model and is made of materials that are similar to the prototype materials satisfying the similitude conditions for a prototype material. A direct model is defined as having similar geometrically properties and application mechanics as in the prototype. The dynamic model in this study is a direct model.

#### 1.4.1.2 Dimensional Analysis and Similitude Requirements

Any structural model must be designed, loaded and the results interpreted according to a set of similitude requirements derived from dimensional analysis and similitude theory. Dimensional analysis was first developed by the 19th century French mathematician, Joseph Fourier. A basic concept was introduced, where the physical units could be represented by their fundamental dimensions of force, length, and time, (F, L, T). Physical laws, such as $F = ma$, must be valid regardless of the choice of units in which the variables are measured, so long as the units are consistent. This is referred to as dimensional homogeneity. The key theorem used in dimensional analysis is Buckingham's $\pi$ theorem. It states that any dimensionally homogeneous equation involving certain physical quantities can be reduced to an equivalent equation involving a complete set of dimensionless products ($\pi$ terms).

A model that satisfies all similitude requirements imposed by dimensional analysis is known as a true model maintaining complete similarity. All the dimensionless products are the same in both the model and the prototype, thereby, satisfying $\pi_{nm} = \pi_{np}$, where *nm* and *np* are the model and prototype products, respectively. In order to form the scale factors, dimensionally independent quantities must be chosen, which facilitates the expression of all other variables. The number of independent variables chosen depends on the number of dimensions. For a dynamic problem, there are three dimensions; F, L and T. Hence, three independent variables are chosen involving all dimensions. These are the gravitational acceleration, length and modulus of elasticity scale quantities. All other variables are expressed in terms of these quantities. Once the $\pi$ terms are formed, they are equated to $\pi_{nm} = \pi_{np}$ and solved for scale factors, $S_i = i_p/i_m$, where *i* is the quantity and the subscripts *p* and *m* refer to the prototype and model, respectively.

### 1.4.1.3 Dynamic Scaling

At any given time under dynamic loading, a structure is in a force equilibrium state. The forces acting on the structure are time-dependent and consist of:

a. Inertia forces (mass and acceleration);

b. Resisting forces (stiffness dependent);

c. Damping forces (energy dissipation);

d. Gravity forces

As stated above, the dynamic behaviour of a model is fully described by three dimensional quantities; force (F), length (L), and time (T). Hence, three independent significant quantities are chosen while all other variables are expressed in terms of these three quantities. The scale factors obtained from similitude considerations for earthquake loading are shown in Table 1.1. The length scale factor is defined as $S_L = \frac{L_{prototype}}{L_{model}}$ and the modulus of elasticity scale factor as $S_E = \frac{E_{prototype}}{E_{model}}$, while the acceleration scale factor, $S_a$, is unity. Since the same material is used in the model as in the prototype, $S_E$, is also unity. The true replica model column in Table 1.1 satisfies all inertial, gravitational and restoring forces, as required by Froude and Cauchy scaling requirements (Harris and Sabnis 1999). This is very difficult to accomplish, particularly satisfying the mass density of the model. Due to the difficulty associated with increasing the mass density of a material while keeping other material properties the same, an artificial mass simulation model is often used to account for the extra mass density. The alternate scaling factors for artificial mass simulation are presented in the fourth column in Table 1.1. To account for the increased density, extra mass is added either in lumped or distributed form. There has been considerable success in testing reduced scale structures on shake tables where extra non-structural mass was added to satisfy the scaled density of the model (Mirza et al. 1979). The scale factor for the mass density in a true model is $S_E/S_L$ as shown in Table 1.1. Since the material used in the model will exhibit the same strength and modulus of elasticity as the prototype material, $S_E$ will be unity. The additional mass that must be added to the model is calculated from the following equation, $\Delta G = m_p(\frac{1}{S_L^2} - \frac{1}{S_L^3})$. It is derived from the ratio of all masses that should be present on the model (scale factor $S_L^2$) and the actual mass of the model calculated from the volume of the material (scale factor $S_L^3$). To simulate the axial load, the force scale factor, $S_q = S_E S_L^2$ is applied to the model. The scale factor already accounts for the extra density. However, if the length dimension needs to be satisfied as well, then additional mass will need to be added to the model.

### 1.4.1.4 Scaling of Additional Components

A masonry structure is constructed from several components; block, mortar, grout and reinforcement. Each component must satisfy the similitude requirements in order to achieve representative masonry elastic and inelastic behaviour. The similitude of the block is attained by scaling down the dimensions. The type of concrete mix and curing conditions may have to be modified to achieve the necessary strength. In addition, the model mortar and grout mix is satisfied by removing larger particle sizes. The modeling of reinforcement is the most important element in a reduced scale model. Proper similitude must be obtained for the stress-strain relationship and bond characteristics. This includes the yield, ultimate strength, extent of yield plateau, and strain hardening. The last two properties are the most important in modeling dynamic behaviour (Harris and Sabnis 1999).

#### 1.4.1.5 Size Effects

Size effect is a phenomenon that influences strength when the specimen size is decreased, especially in heterogeneous material. The use of reduced scale specimens will lead to higher strengths and possibly greater scatter of strength. Two main statistical theories were developed to characterize and study the random heterogeneity of materials; Classical Theory of Bundled Strength and The Weakest Link Theory (Harris and Sabnis 1999).

The concept of bundled strength theory states that the strength of an element is influenced by the strength of the surrounding elements. The model assumes that the specimen consists of parallel elements and the failure of one element will not lead to a total fracture. Instead, the stresses from the weakest element containing the failure will be transferred to the higher strength elements. Unless the elements are arranged in an order of their consecutive failure, total failure will not occur. Since the fracture process is represented by a bundle model, volume does not have a pronounced effect on the mean strength and variance.

The second concept is the weakest link theory, which states that the overall strength of a specimen is determined by the strength of the weakest element present. A single severe defect in any of the constituent elements will lead to a total failure of the specimen. The theory takes into account the volume of the specimen; the larger the volume, the greater the probability of failure in a brittle material, along with a decrease in strength and variance.

These theories ignore the size effect caused by the stress redistribution prior to failure and energy released during crack propagation (Harris and Sabnis 1999). In addition, the weakest link theory only applies to structures that fail right at the initiation of a microscopic fracture, such as metal structures (Bazant and Chan 1996). Thus, to better describe size effects of quasi-brittle materials (i.e. concrete and masonry), fracture mechanics theory should be utilized. Further details of fracture mechanics are summarized by Long (2006).

The variations in the strength of concrete specimens are influenced by several factors (Noor and Boswell 1992); compaction and density, water gain/loss, aggregate grading, curing, drying, and strain rates. The effect of higher strain or loading rates will result in higher strengths. An experimental study was conducted by Farrar e al. (1994) to examine the similitude of dynamic parameters pertaining to resonant frequency, mode shapes and modal damping of reinforced concrete replica models. Results had shown that the frequencies and mode shapes of a prototype structure can be accurately predicted from one-third scale model structures. The variations of the equivalent viscous damping ratios between the model and prototype were found to be greater than other dynamic parameters. However, all damping ratios were less than 2% of critical and would not significantly alter the response of the structure.

### 1.4.2 Small Scale Testing of Structures

Structural laboratories do not typically have the facilities or equipment to accommodate testing of full scale specimens, especially on shake tables. The main advantage of studying structures at reduced scales is to minimize costs associated with testing equipment and construction of test specimens.

In the early 90's, Abboud et al. (1990) conducted a two part study regarding the feasibility of using one-quarter scale concrete masonry blocks. The first part of the study evaluated the applicability of direct small scale models using masonry assemblages. The direct model specimens were geometrically similar to the prototypes, with identical loading conditions as that of the full scale specimens. Data was collected from axial compression, joint shear and splitting tension tests. The behaviour of the scaled masonry assemblages were correlated with the full scale specimens. The results had shown excellent correlation of component material and masonry assemblages to available prototype test data. The second part of the study dealt with the application process of implementing the use of reduced scale model blocks in wall construction. Fourteen one-quarter scale models of reinforced concrete block masonry walls were constructed and tested under monotonic and out-of-plane loading, with and without eccentric axial load. The walls had similar behaviour to that of the full scale walls. It was concluded that the direct modeling of concrete block masonry is feasible.

Abrams et al. (1991) conducted dynamic testing on two one-quarter scale masonry structures that were vertically and horizontally reinforced. They were placed on a shake table and loaded under increasing amplitudes of the 1940 El-Centro earthquake N-S component. The structures were three-storey high and differed in the layout of window and door openings. The objective of the test was to determine whether reduced scale model structures can be utilized to predict the overall structural response under dynamic loading. Flexural behaviour was chosen as the target failure mode to demonstrate that masonry can respond in a ductile manner in the non-linear range. Several significant properties were studied, including the stress-strain relationships of the model reinforcement, compressive strength and stiffness of the model masonry, bond characteristics of the model reinforcement and grout, and shear strength. The amplitude of the base accelerations were varied for each test run to achieve a specific response; before cracking, after cracking, before yielding of reinforcement, at yield of reinforcement and at the ultimate limit state. The results of this study had shown well correlated results between the intended and measured response. This indicated that reduced scale structural models can be used to predict inelastic response.

Shake table tests were also performed by Zarnic et al. (2001) on one-quarter scale masonry in-filled concrete frame models. Two models were built; a one-storey and a two-storey building. Both models satisfied the true replica dynamic scaling laws. The walls were shaken with increasing sin-dwell amplitude motions, which can occur in extreme conditions as aftershocks following an earthquake. The input signal of a sine-dwell is an acceleration sinusoidal signal that is maintained at certain amplitude for a certain period of time. It was found that the response of the models were similar to the global behaviour provided by analysis. The use of reduced scale models satisfying true replica scaling laws to study the global behaviour of structures were shown to be feasible.

El Gawady et al. (2005) reported on the testing of five one-half reduced scale unreinforced brick masonry walls under earthquake loading. The walls were 1,570 mm long at varying heights of 700 mm and 1,600 mm. A separate structure with a moveable mass was used to simulate the inertia mass of the floor above the model walls. In addition, the walls were post-tensioned with steel bars, to simulate an additional 30 kN superimposed load. The loading was simulated with a synthetic earthquake time-history at increasing amplitudes until a predetermined degree of damage was attained. The walls were able to withstand large displacements without significant damage, even after numerous rocking cycles. It was concluded that rocking can be classified as a stable and favourable post-cracking behaviour for unreinforced masonry walls.

### 1.4.3 Summary of Full Scale Dynamic Shake Table Testing

A number of full scale shake table tests were conducted in the masonry field. One such shake table study is summarized below. Other full scale dynamic tests are referenced by Harris and Sabnis (1999).

Turek et al. (2007) performed in-plane shake table tests on eight full scale unreinforced concrete block walls. Three walls were unreinforced and five were strengthened with glass fiber reinforced plastic. The walls were constructed at a height of 2,400 mm and a length of 3,000 mm on a concrete base beam. The last course was fully grouted in order to create a bond beam. A surcharge load was placed on the wall that consisted of several steel plates. Each unreinforced wall was subject to a different test. The first specimen was loaded under an impulse type load, the second specimen was loaded under a 1995 Kobe earthquake record and the last specimen was loaded under an extreme level synthetic earthquake. The results of the test had shown the failure modes of the first two walls were primarily shear dominated with a minor flexural component. The third unreinforced masonry wall formed diagonal cracks and collapsed soon after the onset of the earthquake.

### 1.4.4 Summary of Previous Work on Partially Grouted Masonry Shear Walls

One of the first papers published on partially grouted masonry shear walls was by Thurston and Hutchinson (1982) in New Zealand. Eight 2.4 m high, 1.6 m long and 140 mm wide reinforced walls were tested, which ranged from partially grouted and reinforced to fully grouted and fully reinforced masonry.

The objective was to assess the performance of the walls during inelastic loading conditions through the analysis of the effect of vertical preload, extent of grouting and distribution of reinforcement. The walls had a loading system designed to apply moments of equal magnitude at both ends of the wall (double curvature), resulting in a point of contraflexure at mid-height. Three of the eight walls were partially grouted. Wall 2 was partially reinforced at the ends and mid-length of the wall with horizontal reinforcement present in every four courses. Wall 4 had the same vertical steel arrangement as Wall 2, except without any horizontal reinforcement. Wall 5 had the same vertical reinforcement layout as Walls 4 and 2, except with horizontal reinforcement present in every two courses. Walls 2 and 4 were reported to perform well with gradual strength degradation. The comparison between the hysteresis loops of Wall 5 and its fully grouted counterpart showed that the fully grouted wall was only 20% stronger than the partially grouted wall. Both walls displayed relatively the same ductility but a direct conclusion was not possible due to the use of different loading histories for each specimen. The partially grouted walls demonstrated sufficient ductility, even at lower ultimate strength and stiffness than compared to that of the fully grouted walls. In addition, none of the partially grouted walls exhibited sliding failure characteristics. The study also concluded that using smaller bars at closer spacing had resulted in better inelastic performance compared to using bigger bars at larger spacing.

Partially grouted shear walls were also studied by Matsumura (1987). Tests were conducted on full and reduced scale specimens that were both fully and partially grouted. It was concluded that the shear strength of the partially grouted walls was lower. In addition, it was found that the shear reinforcement was less effective in partially grouted shear walls.

In the 1990's, research on partially grouted masonry shear walls increased. Hamid and Chandrakeerthy (1992) studied the effect of extent of grouting on the compressive strength. Twenty-four three block high wall specimens were constructed from one-third reduced scale blocks, ranging from ungrouted, partially grouted and fully grouted configurations at varying lengths. It was concluded from the test data, that the compression load per unit length wall was increased and the variability of the material was reduced as the grout spacing decreased.

Ghanem et al. (1993) investigated the effect of vertical stress on the in-plane response of partially reinforced masonry walls. The experimental program consisted of three identical masonry shear walls subjected to monotonic loading under different levels of axial stress. The first wall had zero axial stress, the second wall had an axial stress of 0.69 MPa and the third wall had an axial stress of 1.38 MPa. All walls had the same vertical and horizontal reinforcement ratios of 0.12%. The tested walls had three separate and distinct failure modes. The first wall (with no axial stress) failed in flexure and sliding along the base. The second wall (with axial stress of 0.69 MPa) had a mixed flexural/shear failure with significant flexural yielding, toe crushing and diagonal cracking. The last wall (with the highest axial stress of 1.38 MPa) failed in shear governed by diagonal cracking. The test results indicated that increasing the axial stress will result in higher stiffness and strength, followed by a rapid loss of lateral load resisting capacity after the maximum strength was attained. The cracking strength of the wall was shown to increase with higher axial stress due to the increase of the aggregate-interlock force. The ductility was found to decrease with increasing axial stress. It was concluded that increasing the axial stress will change the behaviour of the wall from a ductile flexural failure to a brittle shear failure mode. To avoid the brittle shear failure, it was suggested that the axial stress should not exceed more than 5% of the masonry compressive strength.

Fattal (1993a) developed a modified empirical expression, first proposed by Matusmura (1987), for predicting shear strength of fully grouted and partially grouted masonry shear walls. The expression was evaluated from a variety of experimental data. Measurable improvements in shear strength predictions were obtained from the modified expression.

A preliminary research program, initiated at the National Institute of Standards and Technology (NIST), was drafted by Fattal (1993b) in order to study the effect of partially grouted masonry on the seismic performance of masonry shear walls. In addition, parameters pertaining to horizontal and vertical reinforcement ratio, aspect ratio and axial stress were to be included in the parametric test. The second objective was to verify the modified empirical expression by Fattal (1993a).

From the NIST research program first proposed by Fattal (1993b), an experimental study was conducted by Shultz (1996) pertaining to partially grouted shear walls. Six specimens were constructed with only the end cells of the wall reinforced. All walls were 1,422 mm high with varying lengths. A single bond beam was placed at the mid-height of the wall, which contained varying amounts of horizontal reinforcement. The walls were subject to cyclic drift histories. The hysteresis loops were stable with high initial stiffness and satisfactory energy dissipation. Increasing the height-to-length aspect ratio had a beneficial effect on the ultimate strength but a negative impact on strength deterioration, deformation and energy dissipation capacity. It was concluded that partially grouted masonry is a viable lateral load resisting system for regions of moderate to low seismic risk.

Ingham et al. (2001) reported on several studies pertaining to partially grouted shear walls with an objective to evaluate the vertical reinforcement requirements specified in New Zealand's masonry design standard. The first study consisted of quasi-static in-plane cyclic load tests on twelve nominally reinforced cantilever concrete masonry walls. Nine walls were partially grouted and three were fully grouted. The vertical reinforcement spacing was 800 mm center-to-center except for two walls, which had 600 mm center-to-centre spacing. No axial load was used throughout testing. Two types of failure modes were observed; diagonal tension and rocking/sliding. The lack of horizontal shear reinforcement caused the walls to fail in diagonal tension rather than by rocking/sliding. The second study was an extension of the previous work. Varying configurations of window and doorway openings were added, along with an applied axial compression load. The largest wall (4,200 mm long) had both window and doorway openings. All walls had the same vertical reinforcement spacing as that of the previous reported work. The third study reported on two additional partially reinforced walls that were post-tensioned. They were found to have little or no ductility. Overall, the test results from the three studies of the 16 partially grouted concrete masonry walls showed positive results. The walls had gradual strength degradation and were able to develop a sufficient ductility level of two. It was also concluded that it is better to neglect the development of frame action due to the presence of the bond beam when there are openings in partially grouted masonry walls. Instead, piers on the sides of the openings should be treated as separate vertical cantilevers.

Elshafie at al. (2002) studied the effect of openings on the shear response of reduced scale masonry shear walls. Thirteen one-third reduced scale model walls were fully grouted with varying arrangement of openings. Vertical reinforcement was placed either in every cell or every other cell. The walls were designed to fail in a flexure dominated mode by forming plastic hinges at the top and bottom of the walls. As a result of the tests, a simple analytical approach was refined to predict the failure mechanism and ultimate load capacity, which took into account plastic hinge failure mechanisms for single-storey shear walls with openings. This led to very good predictions of ultimate lateral load capacities and failure mechanisms compared to the experimental results. It was concluded that the wall strength and stiffness were reduced proportionally due to the effect of openings, meaning that the percentage reduction in stiffness attributed to the openings is equal to the percentage of reduction in strength.

Haider and Dhanasekar (2004) evaluated the performance of wide spaced reinforced masonry shear walls. The walls were constructed from full scale hollow clay blocks as single leaf walls (2,870 mm long) and were tested monotonically to failure. Six walls were designed with varied vertical reinforcement spacing ranging between 800 mm and 2,000 mm. The reinforcement consisted of four bars with a constant reinforcing ratio of 0.14%. Among the six walls tested, one was an unreinforced wall to be used as a control specimen. The reinforcement configurations consisted of constant end cell reinforcement with varying mid-wall cell reinforcement. The first wall configuration had two single vertical bars placed in the cells of a single block mid-length of the wall. The spacing of the two vertical bars initially placed in the cells of the center block were increased until the last configuration had two bars in each cell at the ends of the wall. No horizontal reinforcement was provided. A constant vertical compressive stress of 0.50 MPa was applied during testing. It was found that the widely spaced reinforced walls dissipated most of the shear load through diagonal cracking with some heel and toe deformations. On the other hand, the unreinforced wall dissipated the shear load through rigid body motion, which resulted in a rocking mode with large heel and toe deformations. In addition, the walls with uniform spacing arrangements had attained higher ductility and lower stiffness degradation rate than compared to the walls with non-uniform distribution of vertical reinforcement.

A study previously reported by Ingham et al. (2001) was expanded by Voon and Ingham (2005) and Voon (2007). Eight partially grouted nominally reinforced concrete masonry walls with a range of openings were tested under cyclic lateral loading. The spacing of the vertical reinforcement was the same as reported by Ingham et al. (2001). The test results were also similar; the masonry walls showed gradual strength degradation and were able to attain a displacement ductility level of two. It was concluded that a strut-and-tie model should be used to evaluate the strength masonry piers.

In a recent study, Maleki (2008) evaluated the performance of partially grouted shear walls having larger reinforcement spacing than specified by the minimum seismic requirements in the Canadian masonry design standard (CSA S304.1 2004). Five partially grouted shear walls were constructed with varying aspect ratios and reinforcement spacing arrangements while the total reinforcement area of the walls was constant. The walls were tested under fully reversed cyclic lateral loading with constant axial load applied by two hollow cylindrical hydraulic jacks. Direct small scale modeling using one-half reduced scale concrete masonry units were utilized for testing and analysis. The experimental results had shown that the walls were dominated by a shear failure mode. Close agreement was obtained between the estimated and predicted shear resistance values. In addition, the walls had satisfactory energy dissipation and higher attained load reduction factors than suggested by the CSA S304.1 (2004).

## 1.5 Thesis Organization

The first chapter of the thesis summarizes shear wall behaviour followed by the problem statement and the objectives of this study. The literature review presents discussion on the theory of dimensional analysis and summary of previous work pertaining to the reduced scale testing of structures, full scale dynamic shake table testing and partially grouted masonry shear walls.

The second chapter describes the design and construction of the test wall specimens, constituent testing of mortar, grout and steel reinforcement followed by prism and pull-out tests. Procedures and results are discussed. The setup of the testing frame is presented in detail. The loading procedure is discussed and a sample of the 1940 El-Centro earthquake N-S component is presented.

The results of the individual walls are presented in Chapter 3, which including test observations, load-displacement response, mode shape, frequency and damping.

Chapter 4 discusses the analysis of results pertaining to overall hysteretic response, capacity, stiffness, period, displacement ductility and load reduction factors.

The final chapter concludes this study, briefly summarizing each chapter and the main findings. The final conclusion is presented with some recommendations for future work.

## 1.6 Closure

Failure modes of masonry shear walls have been discussed pertaining to shear, flexure and sliding. The code does not provide any provisions pertaining to design of concrete masonry walls that fall in between the unreinforced and reinforced categories. It may be possible that the same target performance in specific regions can be accomplished with the use of partially grouted nominally reinforced walls.

The literature review presents the general theory of similitude and the scaling factors associated with dynamic loading. Reduced scale models of blocks, specimens, walls and buildings under cyclic and dynamic loadings have been discussed. Previous work found in literature on partially grouted concrete masonry shear walls was summarized. The results obtained from previous studies had shown that partially reinforced walls with large reinforcement spacing can achieve sufficient ductility.

Table 1.1: Earthquake response scale factors

| **Scaled Quantities** | **Dimension** | **Scale Factors** | |
|---|---|---|---|
| | | **True Replica Model** | **Artificial Mass Simulation** |
| Force (Q) | F | $S_E S_L^2$ | $S_E S_L^2$ |
| Pressure (q) | $FL^{-2}$ | $S_E$ | $S_E$ |
| Acceleration (a) | $LT^{-2}$ | 1 | 1 |
| Gravitational acceleration (g) | $LT^{-2}$ | 1 | 1 |
| Velocity (v) | $LT^{-1}$ | $S_L^{1/2}$ | $S_L^{1/2}$ |
| Time (t) | T | $S_L^{1/2}$ | $S_L^{1/2}$ |
| Length (l) | L | $S_L$ | $S_L$ |
| Displacement (δ) | L | $S_L$ | $S_L$ |
| Frequency (ω) | $T^{-1}$ | $S_L^{-1/2}$ | $S_L^{-1/2}$ |
| Modulus (E) | $FL^{-2}$ | $S_E$ | $S_E$ |
| Stress (σ) | $FL^{-2}$ | $S_E$ | $S_E$ |
| Strain (ε) | - | 1 | 1 |
| Poisson's ratio (ν) | - | 1 | 1 |
| Mass density (ρ) | $FL^{-4}T^2$ | $S_E/S_L$ | * |
| Energy (EN) | FL | $S_E S_L^3$ | $S_E S_L^3$ |

* satisfied with the addition of distributed or lumped mass

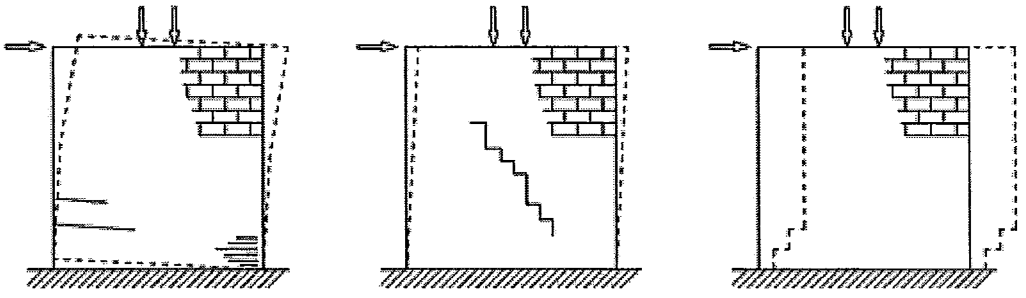

a) Flexural b) Diagonal Shear c) Sliding

Figure 1.1: Types of failures

# CHAPTER 2: EXPERIMENTAL PROGRAM

## 2.1 Introduction

The experimental program was designed to study the behaviour and performance of partially grouted nominally reinforced concrete block walls under seismic loading. A matrix of six test specimens was constructed to study the effects of vertical reinforcement area and spacing without the use of horizontal reinforcement. The amount of reinforcement in the walls had less area and larger spacing than required by Canadian masonry design standard, CSA S304.1 (2004), with the exception of two walls where the spacing requirement was satisfied due to a third reinforcing bar present mid-length of the wall. Five walls were included in the final test matrix due to reinforcement anchorage problems.

## 2.2 Design of Test Wall Specimens

### 2.2.1 Selection of Wall Parameters

The parameters chosen to study the behaviour of partially grouted reinforced shear walls were the amounts of vertical reinforcement and reinforcement spacing. All other key parameters were kept constant. This included the aspect ratio and level of axial load.

A full scale wall length of 1.8 m (four and a half masonry blocks) was chosen as this provided symmetrical distributions of vertical reinforcement and allowed for larger spacing of that reinforcement than specified by the CSA S304.1 (2004). An aspect ratio (height/length) of 1.9 was selected to ensure a flexural dominated behaviour. No horizontal reinforcement was provided, since the calculated shear capacity of each test wall was greater than its flexural capacity. The level of axial load selected was approximately based on a one story building having a 150 mm thick concrete roof with a tributary area of 8 m × 1.8 m and a live load of 2.4 kPa. The final stress of the wall, after the placement of the mass discussed later in the chapter, was approximately 0.29 MPa based on the gross cross-sectional area and 0.50 MPa based on the net cross-sectional area.

### 2.2.2 Selection of Blocks

The reduced scale blocks used in the construction of walls were manufactured by Besser Company in Alpena, Michigan, USA. Geometric data was recorded and compression testing was conducted to determine block strength.

#### 2.2.2.1 Geometric Properties

The block used in the wall specimens represented a full size standard 20 cm hollow stretcher unit complete with frogged-ends and cells. A photograph of the block is presented in Figure 2.1. The blocks had a scale factor of 3.33 based on outer dimensions, which resulted in a 30% reduction of a full size block. The outside dimensions of the block were 117 mm (length) × 57 mm (width) × 57 mm (height) with in a tolerance of ± 1 mm. However, the inside dimensions of the face shells and the webs of the model blocks were wider than expected, as such, they did not have the same scale factor as the outer dimensions of the block. The scale factors of the face shell, web ends and middle web of the block were 2.3, 1.8 and 2, respectively. Block dimensions are presented in Figure 2.2. The wider face shells and webs increased the solid area of the blocks, which were still able to satisfy the CSA A165.1 (2004a) requirement of having less than 75% solid area in order for the blocks to be classified in the Hollow (H) category.

#### 2.2.2.2 Compressive Strength

Compressive tests were performed on the reduced scale units following CSA A165.1 (2004a) and ASTM C140 (2009) standards. The average area representative of the blocks was determined earlier in order to calculate the compressive strength of blocks. Measured dimensions were taken on top and bottom of the block due to face shell tapering. The area of the block was 4,441 mm$^2$ and 4,703 mm$^2$ at the top and bottom, respectively. The average of both areas (4,572 mm$^2$), represented the area at mid-height of the block. Compressive strength results are presented in Table 2.1. Two specimens marked with an asterisk were removed from statistical analysis due to their unusually lower reported strength. This was based on a 15% or larger variation from the mean of the included values.

### 2.2.3 Wall Specimen Description

The original test matrix consisted of six partially grouted masonry walls. The firs tested wall was not included in the test matrix reported herein due to reinforcement anchorage complications, thus leaving five walls in the new test matrix presented in Table 2.2. Sketches of the wall types are shown in Figure 2.3. The original specimens were 18 courses high (1,080 mm) and four and a half blocks long (538.5 mm). After the addition of a concrete base, the specimens were reduced to a height of 17 courses (1,014 mm). The wall's reinforcing ratios of 0.12%, 0.17% and 0.20% were grouped into three category types corresponding to Type I, II, and III walls, respectively. Types I and III had the end cells of the wall reinforced with spacing of 469 mm (corresponding to 1,563 mm at full scale). This spacing exceeded the limit permitted by the Canadian masonry standard, CSA S304.1 (2004). Type II walls had smaller spacing of 235 mm (corresponding to 782 mm at full scale) since an additional reinforcing bar was present mid-length of the wall. All walls had less total reinforcement area than specified by the code. Each specimen was designated by a two letter coding for identification purposes; the first letter represented the wall Type (I, II, or III) and the second letter (A or B) represented the first or second specimen of that type. Two identical walls were tested for each type with the exception of Type III where only one wall was tested. A constant axial load of 8.76 kN was placed on the top of the wall, corresponding to a stress of 0.29 MPa based on gross cross-sectional area. The stress for two and three cell walls based on net cross-sectional area was 0.50 MPa and 0.47 MPa, respectively.

### 2.2.4 Predicted Strength

The flexural capacities at first yield and ultimate conditions, as well as shear capacities were calculated in accordance with Canadian masonry standard, CSA S340.1 (2004). The capacities are presented in Table 2.3. Flexural strengths were calculated based on simple beam theory, while first yield incorporated a linear stress distribution. Compression steel was included in the first yield calculations. However, it was ignored at the ultimate state because the vertical reinforcement was unconfined. All material reduction factors in the design calculations were ignored. The ultimate strain of the masonry was assumed to be 0.0025. The compression depth block factor, $\beta_1$, was less than 80% due to a higher $f'_m$. As determined from prism tests, the grouted masonry had a $f'_m$ and $E_m$ of 27.8 MPa and 16,770 MPa, respectively, while the ungrouted masonry had a $f'_m$ and $E_m$ of 34.8 MPa and 20,038 MPa, respectively. The width of the ungrouted and grouted portion of the wall was taken as 26 mm (face shells) and 57 mm, respectively. The yield strength and elastic modulus of the 3.66 mm diameter vertical reinforcement was 393 MPa and 181,955 MPa, respectively, while the 4.76 mm diameter reinforcement had a yield strength and elastic modulus of 516 MPa and 206,266 MPa, respectively.

The shear capacities of the walls were calculated for diagonal cracking and sliding. All walls were expected to reach a flexural failure mode and first yield before reaching shear failure. The details of flexural and shear strength calculation are presented in the Appendix.

## 2.3 Wall Construction

### 2.3.1 Test Specimens

The original wall specimens were constructed on steel channels by a certified mason provided by Canada Masonry Design and Training Center, Mississauga, ON. The steel channels had the vertical reinforcement bent (at 90°)

and anchored in place through holes drilled in the steel base. Figure 2.4 shows the steel channel base with the vertical reinforcement. Strain gauges were attached at a 10 mm height from the base of the channel on the outer reinforcement bars. The walls were constructed over a period of two days. After the first day, the mason finished laying nine courses for all six walls. Grout was mixed and poured in the cells each day after the mason completed laying the blocks. The water was added slowly to the dry ingredients in order to achieve a proper and consistent mix. Figure 2.5 shows the absorption of water after grouting the walls.

To ensure a weak mortar joint was not created between the ninth and tenth courses constructed on the first and second day respectively, grout was filled to the middle of the last course on the first day. In addition, the top course of the wall was grouted in order to create a bond beam. This was accomplished by placing a fine mesh on the last mortar joint. Figure 2.6 shows the completed construction of two walls. The vertical reinforcement was longer than the height of the walls. After the curing of the walls, the reinforcement was bent 90° and placed in a layer of hydrostone on top of the wall. This made certain that the reinforcement was fully anchored. The hydrostone layer also created a level surface for the mass to be placed on top of the wall.

It was found that the reinforcing bars were fracturing due to high localized stresses around the steel channel base. A concrete base was added to the walls after testing two wall specimens. This would allow for proper anchoring of the reinforcement at the base of the wall.

### 2.3.2 Reinforced Concrete Base Beam

In order to replace the steel base by a concrete foundation, the steel channel and base course were removed. The base course was removed in order to provide sufficient reinforcement development length. As a result of the removal of the base course and mortar joint, the wall height was reduced to 1,014 mm. The concrete foundation replacement was carried out in a three step process; steel base removal, base course removal and casting of the concrete foundation.

The extra length of steel reinforcement that became available after the removal of the base course was shaped into a hook. Strain gauges were placed as close to the base of the wall as possible, as shown in Figure 2.7. While the wall was placed on end supports, the original steel channel was placed inside the wooden formwork, (686 mm length × 152 mm width × 78 mm height) and under the base of the wall at a predetermined height. Details of the reinforced concrete base are presented in Figure 2.8. The reinforcement bar hooks that extended from the base of the wall were placed around the transverse #10M (Area = 100 mm$^2$) reinforcing bars which were welded to the sides of the channels. Four #D4 (Area = 26 mm$^2$) longitudinal bars were placed in the concrete base; two bars 13 mm from the top and bottom. The longitudinal reinforcement was held in place by formwork. In addition, six 13 mm bolts were welded inside the channel. After the curing of the concrete base, they were tightened with nuts in order to prestress the concrete base and help carry tension during testing. Figure 2.9 shows the complete concrete formwork with all the reinforcement and bolts. Before the pouring of concrete, two plastic tubes were coated with grease and placed in the predrilled holes in the steel base to make through holes for the concrete base. Once the concrete hardened, the plastic tubes were removed.

The concrete bases were cast one a time with three days in between castings. Fine aggregate was used for the concrete mix due to tight spacing of the reinforcement inside the formwork. Three cylinder test specimens were casted for each base poured. Compressive strength and slump tests were conducted. The results of the tests are present in Table 2.4.

## 2.4 Constituent Material Properties

### 2.4.1 Mortar

The model mortar mix used in the construction of the walls and prisms was Type S mortar, similar to that as previously used in reduced scale experimental work by Abboud et al. (1990). The mix was reported to work well in simulating prototype specimens and produced excellent correlated results. The dry proportions by weight used were 1.0:0.213:3.83 (Portland cement: lime: masonry sand). In order to create the reduced scale 3 mm joints, particle sizes greater than 1.10 mm (U.S. No. 16 sieve) had to be removed from the masonry sand. The water to cement ratio used was approximately unity with a target mortar flow of 120%. Nine mortar batches were required for the construction of the walls, prisms and mortar cubes. For each batch, a mortar flow test was completed, along with the preparation of three mortar cubes (50.8 mm × 50.8 mm × 50.8 mm). The mortar cubes were tested in compression according to CSA A179 (2004). The results presented in Table 2.5 show the average strength and mortar flow for each mortar batch.

### 2.4.2 Grout

Fine mix was used to grout the walls with particle sizes greater than 1.10 mm (U.S. No. 16 sieve) removed from the sand. The same model grout mix was successfully used by Abboud et al. (1990). The dry proportions by weight used were 1.0:0.043:2.89 (Portland cement: lime: masonry sand). The grout mix was very fluid with slumps of 280 mm and 275 mm for the first and second day batches, respectively. It was necessary to have fluid grout in order to fill all the cells along the height of the wall. Ten cylinder and block moulded specimens were cast over two days of construction for compressive strength tests. The cylinder test specimens had a diameter of 102 mm and a height of 203 mm. The block moulded specimens had same dimensions as that of the model blocks. All grout specimens were tested according to ASTM C1019 (2003). Results of compressive tests are presented in Table 2.6.

### 2.4.3 Masonry Prisms

There were a total of eleven prisms tested (six grouted and five ungrouted) according to CSA A369.1 (1990) requirement to determine the compressive strength, modulus of elasticity and the ultimate strain at failure. The prisms were four blocks high by one block long. They were constructed from one full and one half-block length unit. The frogged ends of the half-blocks were oriented outwards to better represent the actual construction of the wall. The layout of the prisms is presented in Figure 2.10. During handling, one of the ungrouted prisms broke, thus leaving only five prisms available for testing. The net area of the ungrouted prisms was 3,042 mm$^2$ based on the face shell mortar bedding area. The grouted prisms had a net area of 5,879 mm$^2$ based on the face shells, outside webs and cells. The prisms were tested in a Tinius Olsen machine before the start of the wall specimen tests. Two 13 mm linear potentiometers were rigidly attached to a magnetic base and placed under the loading plate on both sides of the prism. The gauge length was taken as the total height of the specimen at the time of testing, including the height of the hydrostone cap. The instrumentation setup is shown in Figure 2.11.

### 2.4.3.1 Ungrouted Prisms

The mason had difficulty laying the blocks and some of the prisms were constructed with accidental eccentricity. Five ungrouted prisms were tested. Two of the ungrouted prisms had a loose fourth course caused by a weak mortar joint. They were still tested as three course high prisms. The average ungrouted strength was 34.8 MPa with an average ultimate strain of 0.0025. The results of the tests are presented in Table 2.7. Figure 2.12 shows the individual stress-strain curves as well as an average curve. There was significant variation in the stress-strain curves of each specimen caused by the eccentricities in the constructed prisms. The first specimen had local spalling in the third course as well as a curved vertical crack in the second course. The failure of the first prism is shown in Figure 2.13. The second specimen had splitting, local spalling and diagonal cracking failures. The last two specimens, 4 and 5 were tested as three course high prisms. Specimen 4 had a combination of vertical cracking and local spalling failures in the top course. The failure mode of specimen 5 consisted of cone and shear failure and vertical web splitting. Specimen 5 attained higher strengths compared to the other prisms. It is interesting to note that both specimens 4 and 5 had the same modulus of elasticity until a certain strain was attained. After that point, there was a significant reduction of the modulus of elasticity in Specimen 4 caused by the eccentricity in the top course. It is clearly shown that eccentricity has a large effect on the strength of the prisms.

The modulus of elasticity for ungrouted masonry was determined to be 20,038 MPa. It was taken as the secant modulus between 5% and 33% of the measured mean compressive strength for each specimen. The modulus of elasticity and compressive strength was substituted into the equation $E_m = k_m f'_m$, where $k_m$ relates the modulus to the compressive stress of masonry. The average $k_m$ value from these specimens was calculated to be 558, which agreed with the results obtained by Hamid at al. (1987).

### 2.4.3.2 Grouted Prisms

Six grouted specimens were tested. The web ends of the grouted prisms were mortared to prevent grout from spilling out of the prism ends. The accidental eccentricities in the prisms were still present but they were not as severe compared to that of the ungrouted prisms. The average grouted strength was determined to be 27.8 MPa with an average ultimate strain of 0.0021. Stress-strain curves of the grouted prisms test are shown in Figure 2.14 and the results are summarized in Table 2.8. All prisms failed by diagonal shear and face shell separation. The fourth specimen had a conical failure mode in addition to diagonal cracking. Figure 2.15a and 2.15b shows the photographs of Specimens 4 and 5 with their associated conical and shear failure modes, respectively.

The modulus of elasticity for grouted masonry was determined to be 16,770 MPa. It was taken as the secant modulus between 5% and 33% of the measured mean compressive strength for each specimen. The average $k_m$ value relating the modulus of elasticity and compressive strength was calculated to be 606, which agreed well with the $k_m$ values obtained by Hamid at el. (1987). It is interesting to note the large difference between the coefficients of variations between the ungrouted and grouted specimens. The compressive strength c.o.v. was 24.9% and 8.2% and the modulus of elasticity c.o.v. was 42.6% and 4.5% between the ungrouted and grouted prisms, respectively. The ultimate strain c.o.v. of the ungrouted and grouted specimens was 9.1% and 5.1%, respectively.

### 2.4.4 Pull-Out Tests

Eighteen pull-out tests were completed to test the bond strength between the reinforcement and grout. One, two and three high half-block specimens were constructed with each type having 6 specimens. Each specimen was designated by a two letter coding system for identification purposes; the first letter represented the construction day (A - first day of construction, B - second day of construction) and the second letter represented the use of a smaller or larger diameter reinforcement bar. The specimens were placed on a steel plate with a layer of hydrostone in between the specimen and the plate. This levelled the specimen and allowed for even distribution of stresses during loading. The steel plate had a small hole drilled in the center to allow the reinforcement pass through and clamp in the Tinius Olson machine. Figure 2.16 shows the test setup of the specimens.

The results from the pull-out tests are reported in Table 2.9. Specimens marked with an asterisk were removed from statistical analysis due to their unusually lower reported strength. This was based on a 15% or larger variation from the mean of the included values. The average ultimate load attained by one-course, two-course and three-course high specimens were 2.2 kN, 3.2 kN and 5.7 kN, respectively. The trend shows that the pull-out capacity was increased as additional courses were added to the specimens.

After testing was completed, the bond between the grout and the reinforcement was examined. Three specimens from the three-course high type had the bottom cells ungrouted. In addition, two specimens from the two-course high type had the bottom cells ungrouted. All of the one-course high specimens were fully grouted. The ungrouted portions may be attributed to the grout having difficulty flowing past the excess mortar inside the cells of the half-blocks.

### 2.4.5 Steel Reinforcement

Two sizes of steel reinforcing wire (3.66 mm and 4.76 mm diameter) were used as vertical reinforcement in the walls. Three random samples, 700 mm in length of each size were tested in a Tinius Olsen machine to determine their yield stress and elastic modulus. The steel was ordered from Blok-Lok Ltd., Toronto and was manufactured from smooth cold drawn steel wire conforming to the tensile strength requirements of ASTM 82 (2007). Since the wire was smooth, deformations were put in place manually by squeezing the steel wire between two threaded rods. Deformations in the wire would better represent and simulate the bond between the grout and reinforcement. Preliminary test data showed that the deformations did not change the wire properties.

The stress-strain curves for reinforcement sizes of 4.76 mm and 3.66 mm diameter are shown in Figure 2.17 and Figure 2.18, respectively. The curves had a linear portion in the elastic range before any yielding started. The offset method at 0.2% was used in order to find the yield and modulus of elasticity. The larger diameter reinforcement showed a more distinct yield point than its smaller counterpart. Table 2.10 reports the yield and modulus of elasticity from the offset method.

## 2.5 Test Setup

To provide support for the mass placed on top of the walls, an out-of-plane testing rig was constructed. A front view of the complete setup is show in Figure 2.19 and Figure 2.20a with an additional side view shown in Figure 2.21. An

892.5 kg mass was placed on top of the walls. It was built from six steel plates, three side by side, which were each 510 mm long × 513 mm wide × 65 mm high. Two sets of plates (three in each set) were bolted together to a single plate (1,143 mm long × 408 mm wide × 25 mm high). The plates were bolted using eight 13 mm threaded rods, four in each set of plates. In addition, six steel angles with through holes were bolted to the threaded rods at top of the mass in order for the mass to be easily lifted by the crane chain. To complete the mass setup, eight ball bearings were attached to the final mass. Four 13 mm thick steel plate strips were cut to the height of the mass and two ball bearings were bolted to the steel plate strips. The steel plates were tack welded to the mass at four locations (two on each end). This allowed the mass to move in-plane within the channel guides during earthquake loading while restraining out-of-plane motion. In an actual building, the out-of-plane motions would have been restrained by the diaphragm. The front view of the setup in Figures 2.19 shows the placement of the bearings. A close-up side of view of the bearings is shown in Figure 2.22.

In order to transfer inertia force to the wall, the mass was attached to the top of the wall through a fixed connection. This was accomplished by the use of steel angles. The angles were attached rigidly to both sides of the wall by the use of epoxy and three bolts. The holes for the bolts were predrilled in the bond beam and the angles.

The extra length of reinforcement at the top of the wall was bent 90° and placed in a layer of hydrostone. This made certain that the reinforcement was fully anchored. The hydrostone layer also created a level surface for the mass to be placed on top of the wall. Once this was completed, the wall was placed on the shake table. A final thin layer of hydrostone was spread on the top of the dry layer and the mass was lowered into place as illustrated in Figure 2.22. Final tack welding was done at three spots on each side of the mass as shown in Figure 2.24.

The second part of the setup involved the construction of the out-of-plane test rig. The purpose of the rig was to provide out-of-plane support for the mass and to carry the load of the mass during testing if the wall suddenly failed. The rig was built by first erecting a primary I-beam, spanning 5.25 m in length between the columns of the shake table in the E-W direction. The beam was placed in the center of the shake table, above and in-plane to the wall specimen. A lateral member was welded perpendicular to the span center of the primary I-beam and adjacent channel (south of the primary I-beam). The addition of the lateral member reduced the unsupported length, thereby increasing the strength and stability of the primary I-beam. Figure 2.21 shows the location of the lateral support member from a side view. To provide additional safety, a through hole was created on top of the I-beam by welding together two angles flush to the center of the primary I-beam. A chain was attached in each E-W direction from the welded angle to the adjacent columns. This allowed for the columns to carry additional load if the mass collapsed. The front view of the setup in Figures 2.20 shows the placement of the chains.

The final stage in the test rig setup was the construction of a box frame for the mass. It was constructed from two channels and two secondary I-beams as shown in Figure 2.21, along with a close-up view in Figure 2.22. The secondary I-beams were bolted perpendicular to the main I-beam. The channels were bolted in-plane to the secondary I-beams, which provided a guide for the mass during earthquake loading. The channels could be easily adjusted as slotted holes were created in the secondary I-beams. The final photographs of the rig setup are shown in Figures 2.23a and 2.23b.

### 2.6 Instrumentation and Measurements

Three types of measurements were recorded during testing; accelerations, deflections and strains. Data was recorded at 0.005 second intervals by a 16 channel data acquisition system. All 16 channels were utilized in recording measurements. The final placement of the instrumentation is shown in Figure 2.25. The labels AC and SP represent the accelerometers and string potentiometers, respectively. The table displacements and accelerations were labelled SPT and SPA, respectively. The strain gauges were designated by SE and SW, representing east and west directions, respectively.

#### 2.6.1 String Potentiometers

To measure the deflections of the wall, a reference frame was built on the west side independent from the shake table. The reference frame is shown in Figure 2.20a. Four string potentiometers were attached to the frame which measured total deformations at the center of gravity of the mass (SP 1), mid-height of the top course (SP 2), center of the ninth course (SP 3) and mid-height of the second course (SP 4). Lower placement of the string potentiometers was not possible due to test setup restrictions. A fifth string pot (SPT) was mounted on the frame of the actuator which measured the total displacement of the table. The relative deformations of the wall were found by subtracting table displacements from string potentiometer readings.

### 2.6.2 Linear Potentiometers

The vertical displacements were measured by four ±13 mm stroke linear potentiometers. They were mounted 29 mm from the ends of the wall with the shafts of the linear potentiometers facing down. The first set, LP1 (east) and LP3 (west), was placed on the fifth course at a height of 260 mm from the base. The second set, LP2 (east) and LP4 (west), was placed on the third course at a height of 137 mm from the base. The vertical displacements were captured by the use of steel frames, which were welded on both ends of the concrete slab, as shown in Figure 2.26. This allowed for accurate measurements, otherwise not possible with the use of a string connected to the shaft and wall.

### 2.6.3 Strain Gauges

Strain gauges were placed on the vertical reinforcing bars located at the ends of the wall. A smaller gauge length of 2 mm was selected because of limited space available for mounting the gauge. The bars were cleaned in the area where the gauge was to be attached. After attachment, the gauges were coated with a sealer coating for water and damage proofing. Neoprene rubber was wrapped around the gauges to provide extra physical protection.

### 2.6.4 Accelerometers

The in-plane forces were measured by two accelerometers placed at center of gravity of mass (AC 1) and the mid-height of the top course of the wall (AC 2). They had a ±1.7 g range, which was adequate as the wall response accelerations were not to exceed ±1.0 g. Each accelerometer required two channels since accelerometers also measured accelerations in the transverse direction.

A third accelerometer was attached on the shake table (ACT). The accelerometer had a range of ±2 g and only needed one channel to measure accelerations. The table accelerations were compared to the target accelerations and target response spectra.

## 2.7 Model Earthquake

The displacement time-history of the 1940 El-Centro Imperial Valley Irrigation District N-S component was used to simulate the earthquake. Table 2.11 presents ground motion specifications of the earthquake at full scale and model scale. The prototype displacements of the earthquake were scaled by a factor of 3.33 and time was compressed by a factor of $\sqrt{3.33}$. The displacement time-history was re-sampled to 500 Hz as the final input signal to the MTS 407

Controller. The acceleration and displacement time-history along with the response spectrum of El-Centro earthquake are shown in Figure 2.27.

## 2.8 Loading Procedure

All walls were subjected to nine scaled El-Centro earthquakes time-histories increasing in amplitude. The target accelerations and displacements of the earthquake are presented in Table 2.12. The purpose of the incremental amplitude increase was to show progressive damage of the wall specimens. The shake table was displacement controlled, hence, the displacement time-history of the El-Centro was used to reproduce the target ground accelerations. The first run had a PGD (peak ground displacement) of 3.7 mm with an estimated PGA (peak ground acceleration) of 0.04 g. It was chosen to keep the wall within its elastic limit. The second run was double of the first run and the next six runs had incremental amplitude increases of 25% from their previous runs. The final run was increased by 12.5% in order not to exceed the capacity of the actuator.

## 2.9 Closure

The experimental program discussed the design of the wall specimens pertaining to the selection of parameters and predicted shear and flexural strengths. Construction of the shear walls was discussed, along with the concrete base replacement. The constituent material, prism and pull-out test data were reported. Details of the test setup were provided. The last three sections discussed the instrumentation setup, loading procedure and the model earthquake.

Table 2.1: Compressive strength of masonry units

| **Specimen** | **Ultimate Load (kN)** | **Compressive Strength[1] (MPa)** |
|---|---|---|
| 1 | 192.0 | 42.0 |
| *2 | *155.5 | *34.0 |
| *3 | *130.3 | *28.5 |
| 4 | 200.3 | 43.8 |
| 5 | 165.0 | 36.1 |
| 6 | 200.0 | 43.7 |
| 7 | 172.5 | 37.7 |
| 8 | 201.3 | 44.0 |
| **Average** | 188.5 | 41.2 |
| **c.o.v. (%)** | 8.4% | |

[1] Average area = 4,572 $mm^2$

* Excluded from statistical analysis

Table 2.2: Test matrix of wall specimens and full scale comparison

| | | **Model Scale** | | | **Full Scale** | | |
|---|---|---|---|---|---|---|---|
| **Wall Type** | | **I** | **II** | **III** | **I** | **II** | **III** |
| **# of Specimens** | | 2 | 2 | 1 | | | |
| **Dimensions (mm)** | **Height** | 1,014 | 1,014 | 1,014 | 3,380 | 3,380 | 3,380 |
| | **Length** | 539 | 539 | 539 | 1,795 | 1,795 | 1,795 |
| | **Aspect Ratio (H/L)** | 1.9 | 1.9 | 1.9 | 1.9 | 1.9 | 1.9 |
| **Reinforcement** | **Spacing (mm)** | 469 | 235 | 469 | 1,563 | 782 | 1,563 |
| | **Size (Ø mm)** | 3.66 | 3.66 | 4.76 | 12 | 12 | 16 |
| | **Area ($mm^2$)** | 10.5 | 10.5 | 17.8 | 117 | 117 | 198 |
| | **Ratio (%)** | 0.12 | 0.17 | 0.2 | 0.12 | 0.17 | 0.20 |
| **Axial Stress (MPa)** | **Net Area** | 0.50 | 0.47 | 0.50 | 0.50 | 0.47 | 0.50 |
| | **Gross Area** | 0.29 | 0.29 | 0.29 | 0.29 | 0.29 | 0.29 |

Table 2.3: Predicted flexural and shear strength

| **Wall Type** | **Flexural Strength (kN)** | | **Shear Strength (kN)** |
|---|---|---|---|
| | **Yield** | **Ultimate** | |
| I | 3.6 | 3.9 | 7.9[1] |
| II | 3.9 | 4.8 | 9.3[2] |
| III | 5.6 | 6.0 | 7.9[1] |

[1] Sliding dominated

[2] Shear dominated

Table 2.4: Concrete base compressive strength and slump

| **Specimen** | **Compressive Strength (MPa)** | **Slump (mm)** |
|---|---|---|
| IA | 57.6 | 220 |
| IIA | 53.3 | 240 |
| IIIA | 58.5 | 220 |
| IB | 62.4 | 172 |
| IIB | 59.0 | 245 |
| **Average** | 58.1 | 219 |
| **c.o.v. (%)** | 5.6% | 13.2% |

Table 2.5: Mortar batch strength and flow

| **Batch** | **Load (kN)** | **Strength (MPa)** | **Mortar Flow (%)** |
|---|---|---|---|
| 1 | 46.2 | 17.9 | 111 |
| 2 | 42.6 | 16.5 | 119 |
| 3 | 44.2 | 17.1 | 128 |
| 4 | 43.4 | 16.8 | 123 |
| 5 | 36.5 | 14.1 | 116 |
| 6 | 59.9 | 23.2 | 126 |
| 7 | 44.4 | 17.2 | 124 |
| 8 | 45.2 | 17.5 | 123 |
| 9 | 49.3 | 19.1 | 118 |
| **Average** | 45.7 | 17.7 | 121 |
| **c.o.v. (%)** | 13.8% | | 4.4% |

Table 2.6: Specimen grout strength

| **Specimen** | **Strength (MPa)** | |
|---|---|---|
| | **Cylinder** | **Block Moulded** |
| A | 22.7 | 30.2 |
| D | 30.5 | 34.7 |
| C | 23.3 | 30.3 |
| D | 23.8 | 33.0 |
| E | 24.4 | 31.9 |
| F | 28.0 | 33.0 |
| G | 22.8 | 34.2 |
| H | 32.5 | 34.1 |
| I | 26.3 | 32.9 |
| J | 33.5 | 35.4 |
| **Average** | 26.8 | 33.0 |
| **c.o.v. (%)** | 15.4 | 5.3 |

Table 2.7: Ungrouted prism stress, strain and modulus of elasticity

| **Prism** | **Max Strength $f'_m$ (MPa)** | **E (MPa)** | **k ($E / f'_m$)** | **Ultimate Strain$\times 10^{-3}$** |
|---|---|---|---|---|
| 1 | 22.8 | 8,893 | 390 | 2.460 |
| 2 | 34.4 | 17,619 | 512 | 2.789 |
| 3 | 36.2 | 29,063 | 802 | 2.653 |
| 4* | 33.6 | 16,429 | 489 | 2.214 |
| 5* | 47.2 | 28,184 | 597 | 2.376 |
| **Average** | 34.8 | 20,038 | 558 | 2.498 |
| **c.o.v. (%)** | 24.9 | 42.6 | 27.8 | 9.1 |

* 3 Course high prisms

Table 2.8: Grouted prism stress, strain and modulus of elasticity

| **Prism** | **Max Strength $f'_m$ (MPa)** | **E (MPa)** | **k ($E / f'_m$)** | **Ultimate Strain $\times 10^{-3}$** |
|---|---|---|---|---|
| 1 | 30.5 | 17,537 | 574 | 2.184 |
| 2 | 25.6 | 16,791 | 655 | 1.867 |
| 3 | 27.9 | 16,246 | 583 | 2.037 |
| 4 | 27.3 | 15,841 | 580 | 2.090 |
| 5 | 30.2 | 17,767 | 588 | 2.033 |
| 6 | 25.1 | 16,439 | 656 | 2.084 |
| **Average** | 27.8 | 16,770 | 606 | 2.049 |
| **c.o.v. (%)** | 8.2 | 4.5 | 6.4 | 5.1 |

Table 2.9: Ultimate capacity of pull-out specimens

a) One-course high specimens

| **Specimen** | **Ultimate Load (kN)** |
|---|---|
| *AL | *3.4 |
| AS | 2.3 |
| BL | 2.2 |
| BS | 2.1 |
| *BS | *4.0 |
| *AL | *0.8 |
| **Average** | 2.2 |
| **c.o.v. (%)** | 4.6 |

* Excluded from statistical analysis

b) Two-course high specimens

| **Specimen** | **Ultimate Load (kN)** |
|---|---|
| BL | 3.3 |
| *AL | *1.3 |
| AS | 3.1 |
| *BS | *2.6 |
| BS | 3.6 |
| AS | 3.3 |
| **Average** | 3.3 |
| **c.o.v. (%)** | 6.2 |

* Excluded from statistical analysis

c) Three-course high specimens

| **Specimen** | **Ultimate Load (kN)** |
|---|---|
| *BS | *4.6 |
| *BL | *8.5 |
| AL | 5.0 |
| BS | 5.0 |
| AS | 5.3 |
| AL | 5.9 |
| **Average** | 5.7 |
| **c.o.v. (%)** | 8.0 |

* Excluded from statistical analysis

Table 2.10: Steel yield strength and modulus of elasticity

| **Specimen** | **Yield Strength (MPa)** | | **Modulus of Elasticity (MPa)** | |
|---|---|---|---|---|
| | **3.66 mm Ø** | **4.76 mm Ø** | **3.66 mm Ø** | **4.76 mm Ø** |
| 1 | 390 | 520 | 180,688 | 202,512 |
| 2 | 395 | 520 | 179,403 | 208,820 |
| 3 | 395 | 508 | 185,773 | 207,466 |
| **Average** | 393 | 516 | 181,955 | 206266 |
| **c.o.v. (%)** | 0.7 | 1.3 | 1.9 | 1.6 |

Table 2.11: Ground motion specifications

| **Specification** | **Full Scale (Original Record)** | **0.3 Scale (Max Amplitude)** |
|---|---|---|
| Direction | S00E (N-S) | |
| Station | 117 USGS | |
| PGA (g) | 0.348 | 0.329 |
| PGV (mm/s) | 337.5 | 177 |
| PGD (mm) | 108.0 | 31.6 |
| Duration (s) | 53.73 | 29.9 |

Table 2.12: Acceleration and displacement amplitudes of runs

| **Run** | **Target PGA (g)** | **Target PGD (mm)** |
|---|---|---|
| A | 0.04 | 3.7 |
| B | 0.08 | 7.4 |
| C | 0.10 | 9.2 |
| D | 0.12 | 11.5 |
| E | 0.15 | 14.4 |
| F | 0.19 | 18.0 |
| G | 0.23 | 22.5 |
| H | 0.29 | 28.1 |
| I | 0.33 | 31.6 |

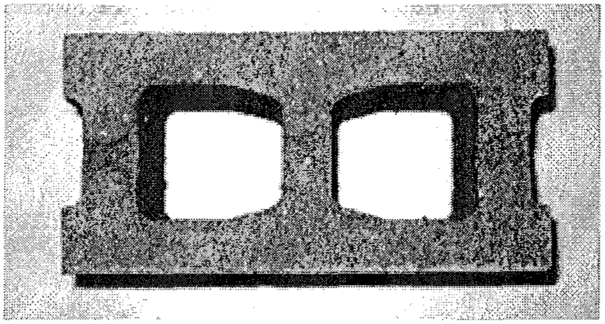

(117 mm long × 57 mm wide × 57 mm high)

Figure 2.1: Model scale block plan view

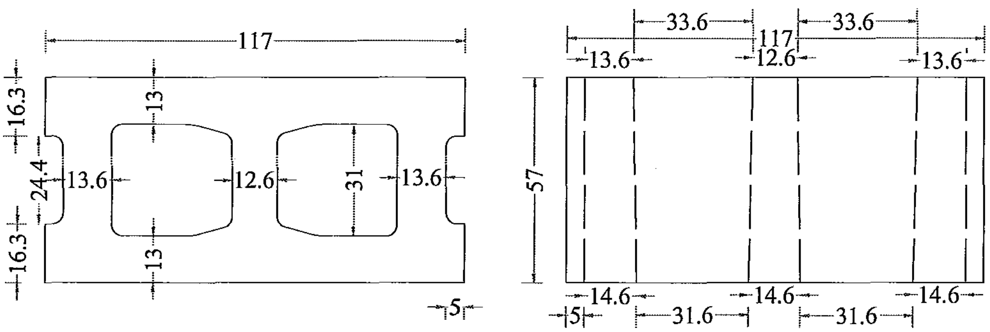

(all dimensions in mm)

a) Plan View b) Elevation View

Figure 2.2: Model scale block dimensions

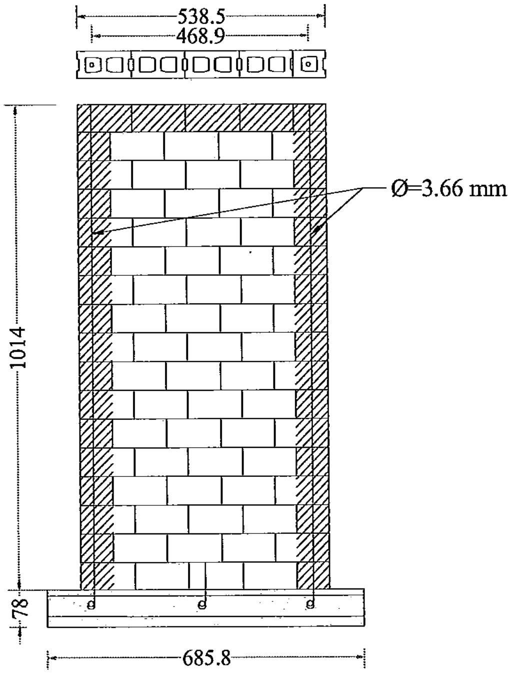

a) Type I Wall: Ø=3.66 mm end-cell reinforced
(all dimensions in mm)

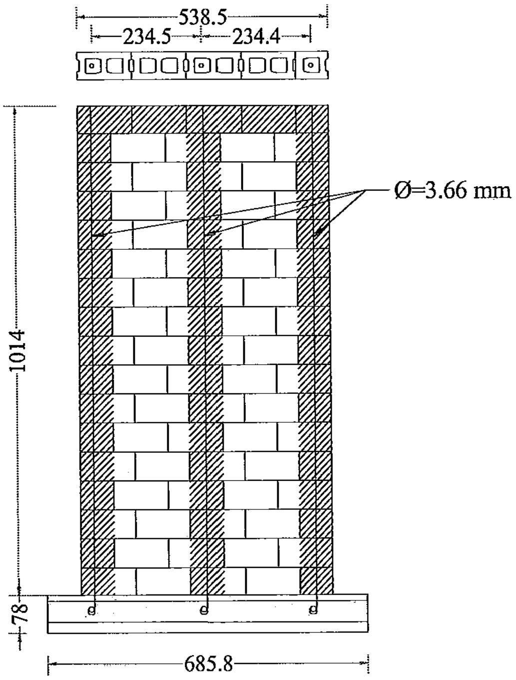

b) Type II Wall: Ø=3.66 mm end and mid-cell reinforced
(all dimensions in mm)

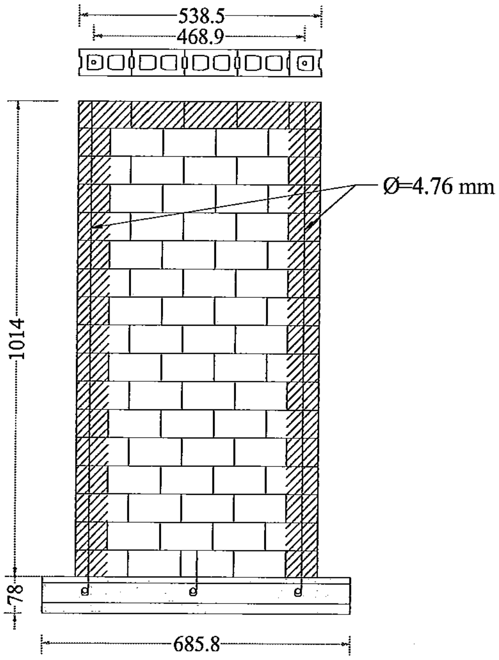

c) Type III Wall: Ø=4.76 mm end-cell reinforced
(all dimensions in mm)

Figure 2.3: Wall type reinforcement arrangements

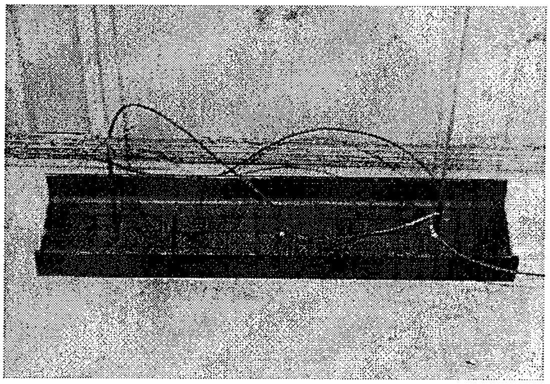

Figure 2.4: Base channel for wall specimens

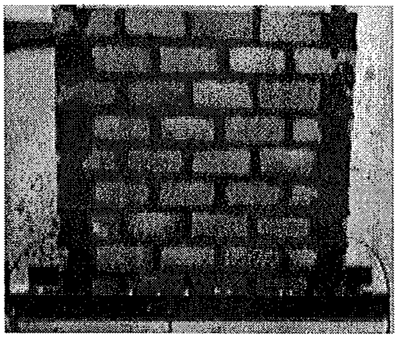

Figure 2.5: Absorption of water after grouting

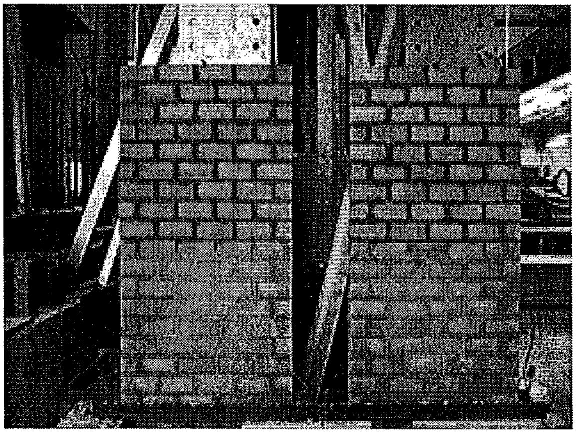

Figure 2.6: Completed construction of walls

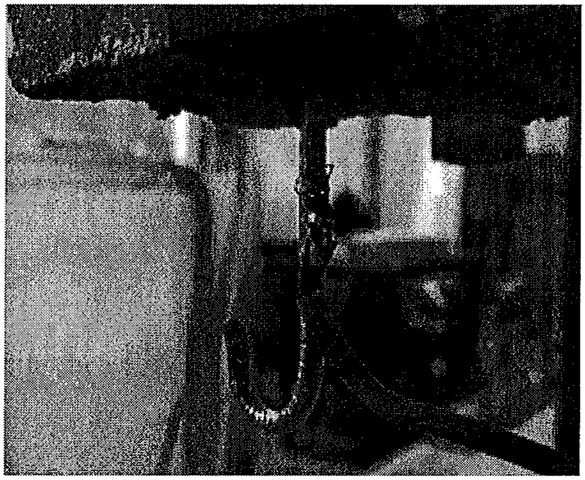

Figure 2.7: Placement of strain gauges

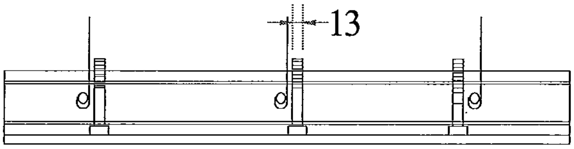

a) Elevation view

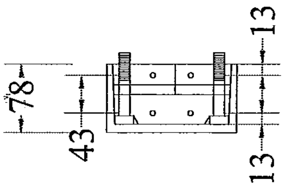

b) Side view

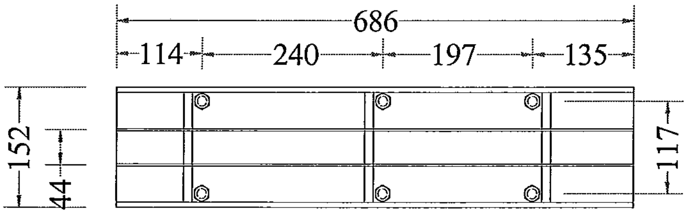

c) Plan view

Figure 2.8: Reinforced concrete base layout

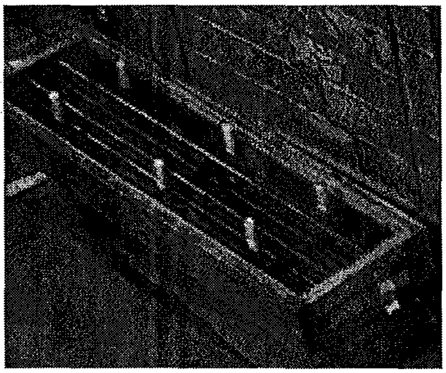

Figure 2.9: Formwork with reinforcement and welded bolts

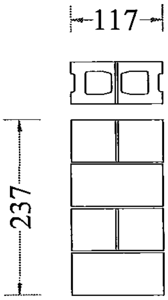

(all dimensions in mm)

Figure 2.10: Details of prism construction

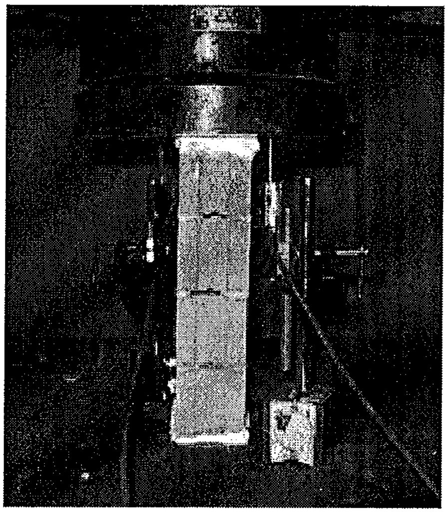

Figure 2.11: Prism instrumentation setup

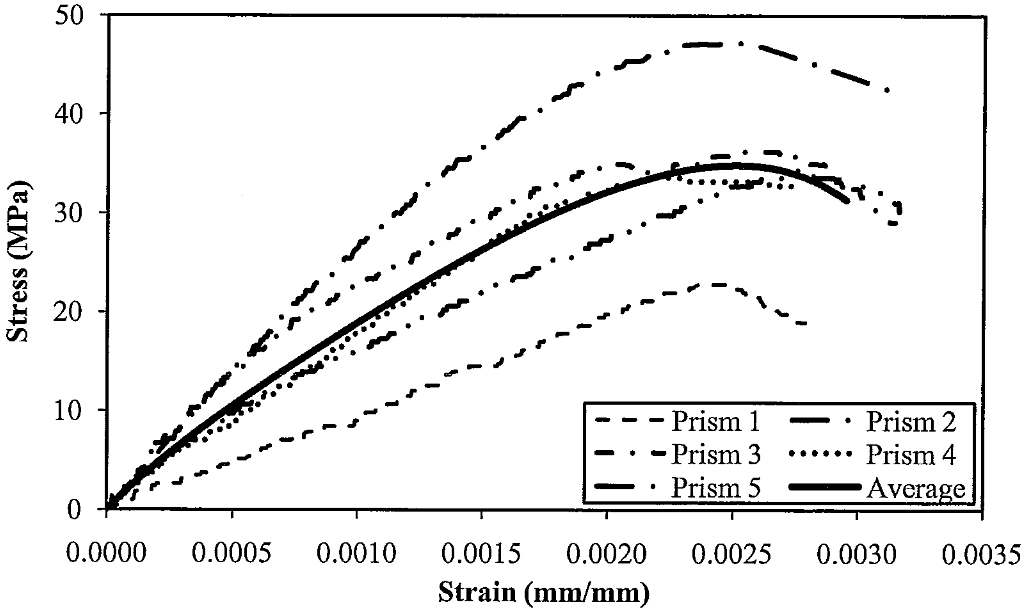

Figure 2.12: Ungrouted stress-strain curves

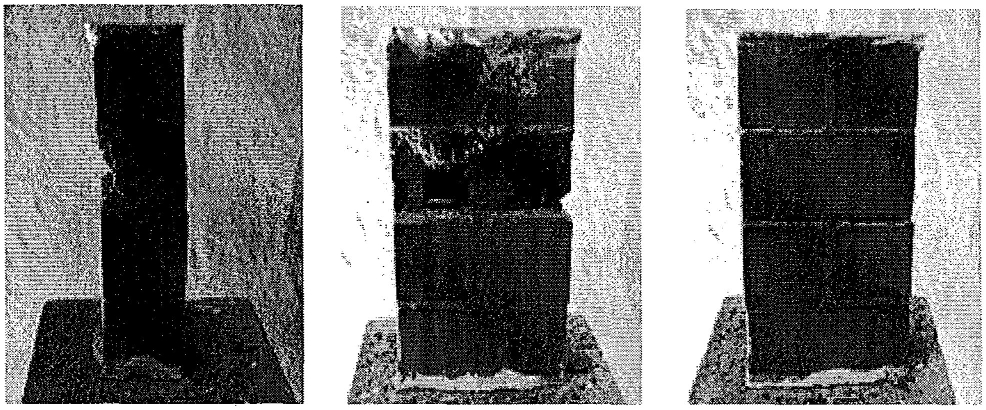

Figure 2.13: Eccentric failure of specimen 1

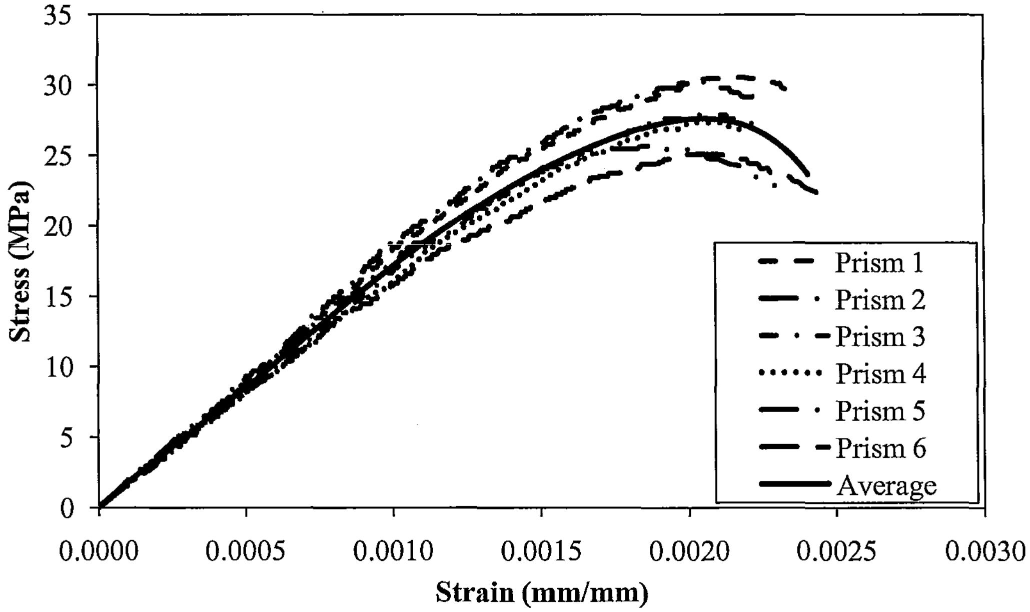

Figure 2.14: Grouted stress-strain curves

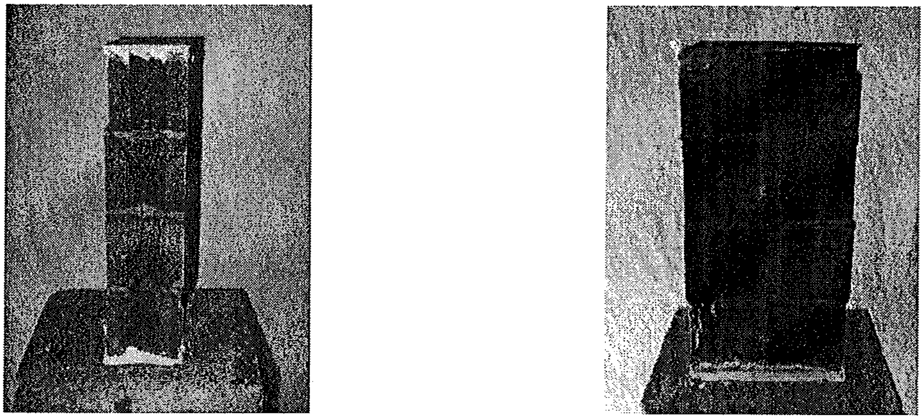

a) Specimen 4: conical failure b) Specimen 5: shear failure

Figure 2.15: Failure of grouted specimens

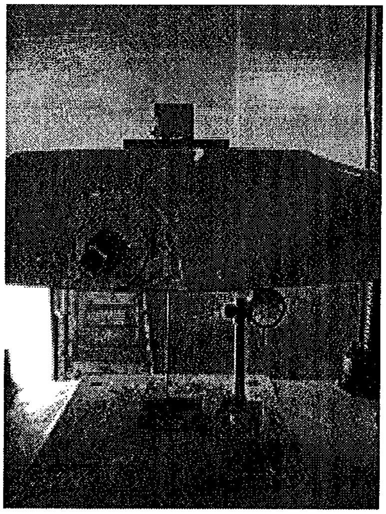

Figure 2.16: Pull-out test

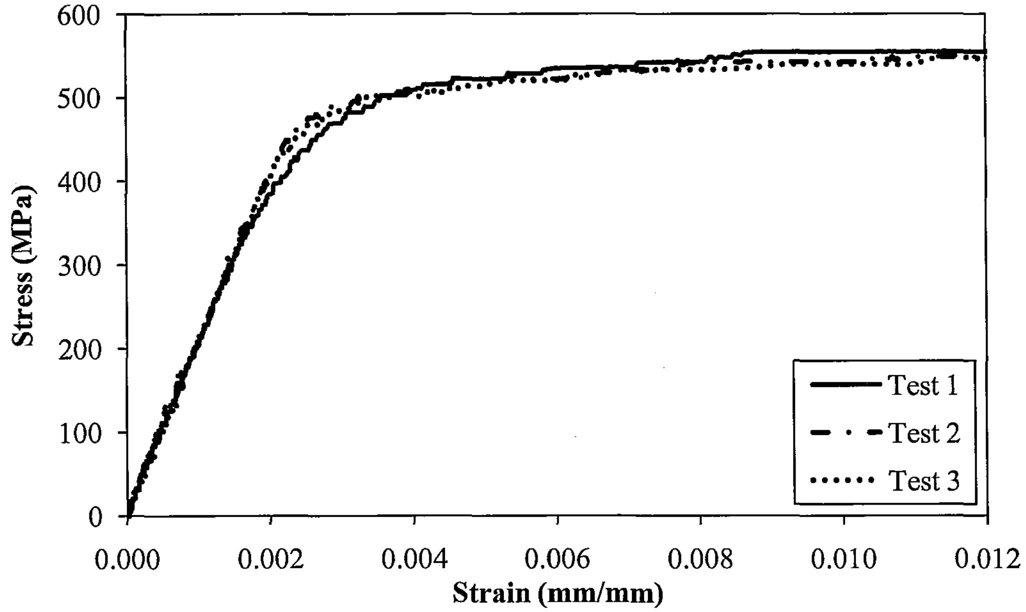

Figure 2.17: Stress-strain curves for Ø=4.76 mm wire reinforcement

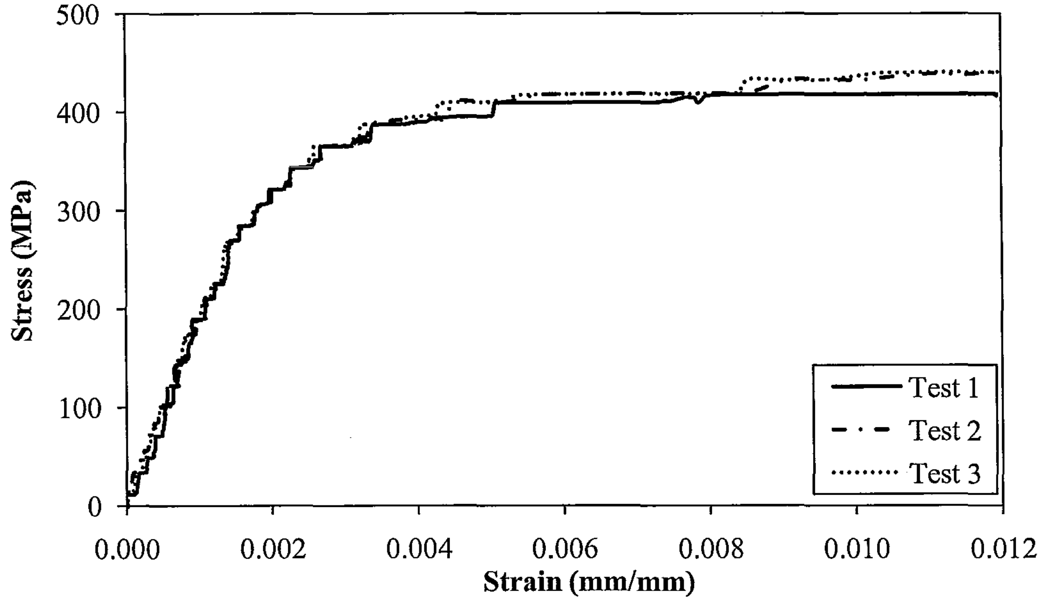

Figure 2.18: Stress-strain curves for Ø=3.66 mm wire reinforcement

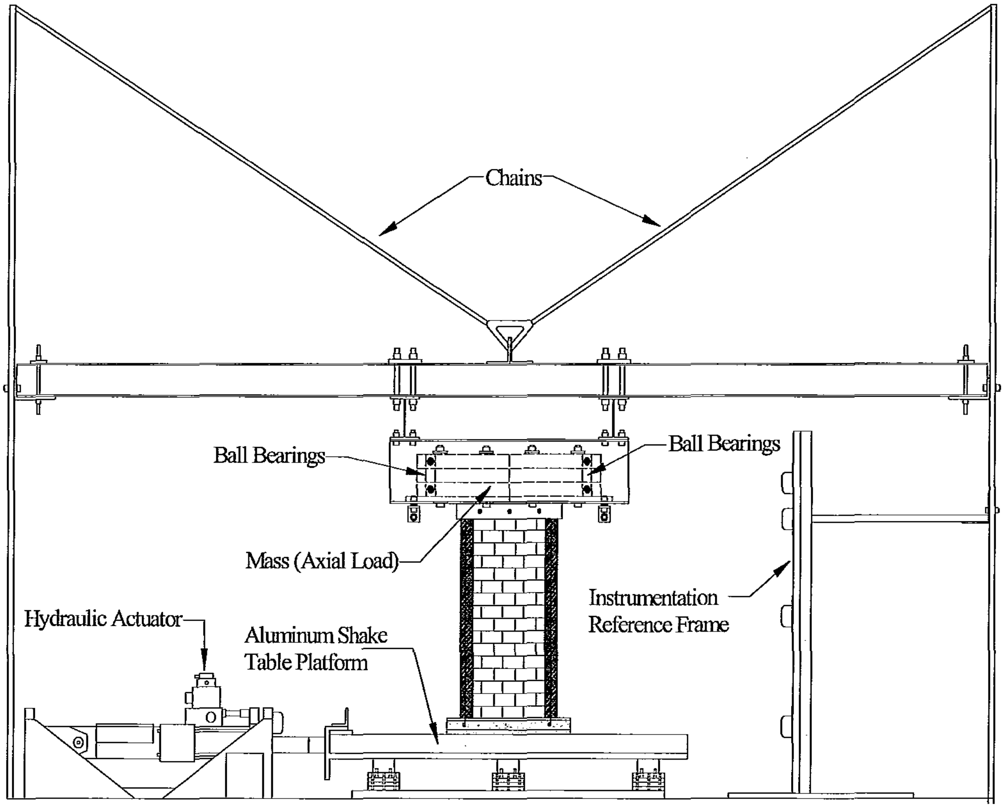

Figure 2.19: Front view of test setup

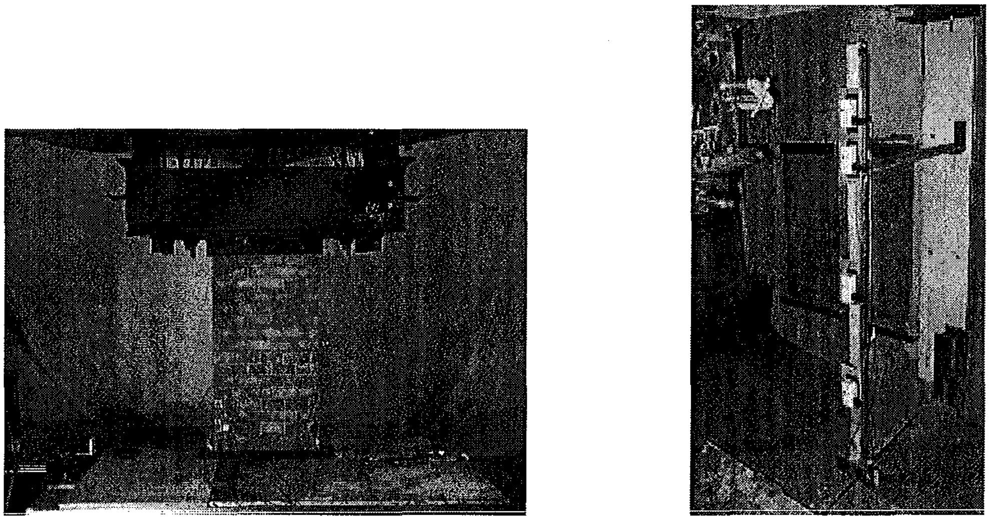

a) Specimen on shake table platform b) Instrumentation reference frame

Figure 2.20: Front view of wall specimen on the shake table and instrumentation reference frame

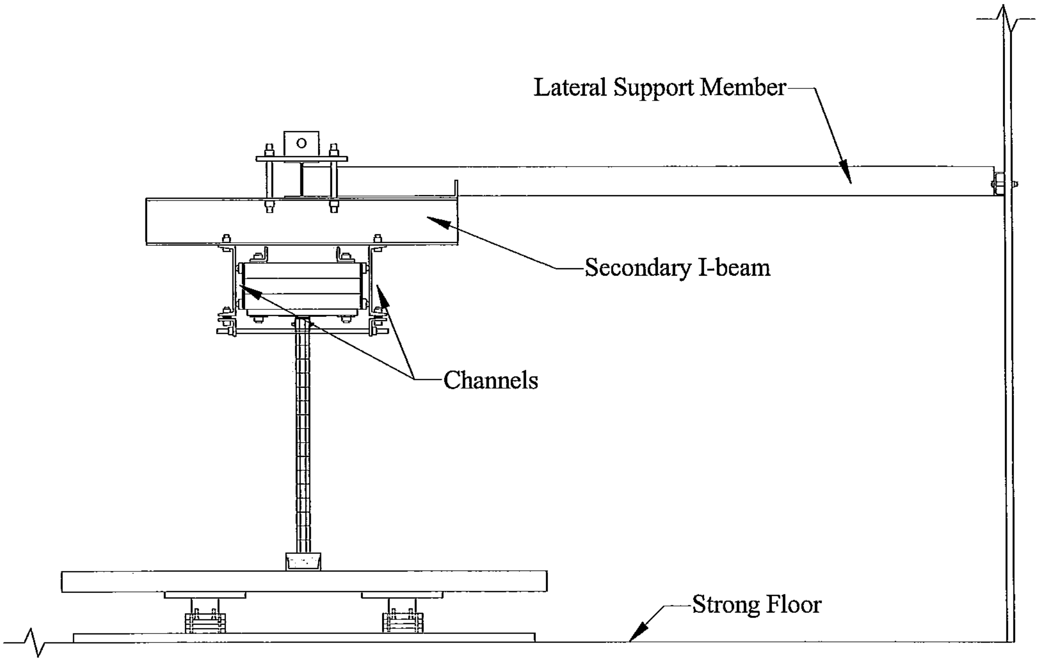

Figure 2.21: Side view of test setup

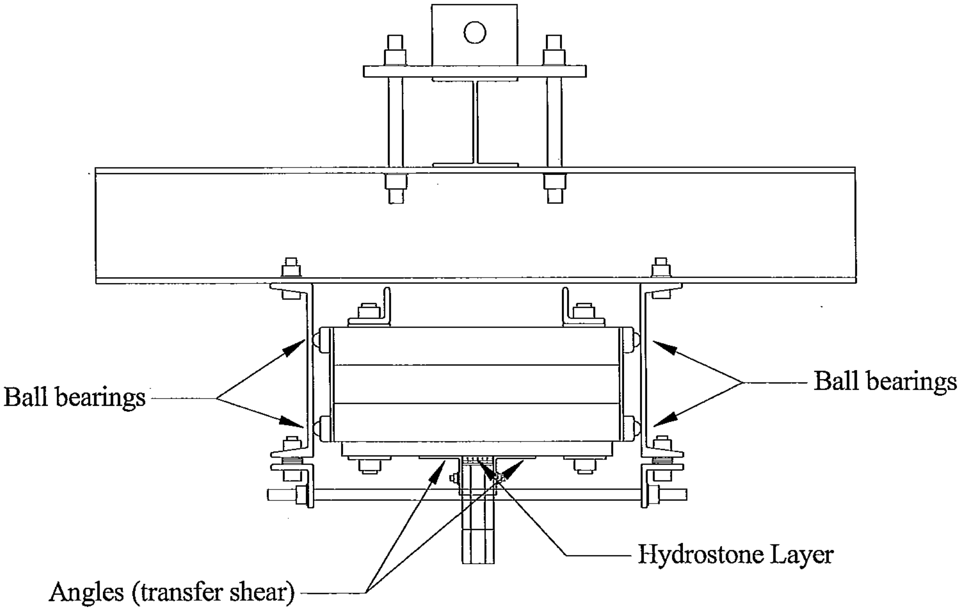

Figure 2.22: Close-up side view

a) Mass inside the rig setup b) Out-of-plane test rig

Figure 2.23: Alternate side views of test setup

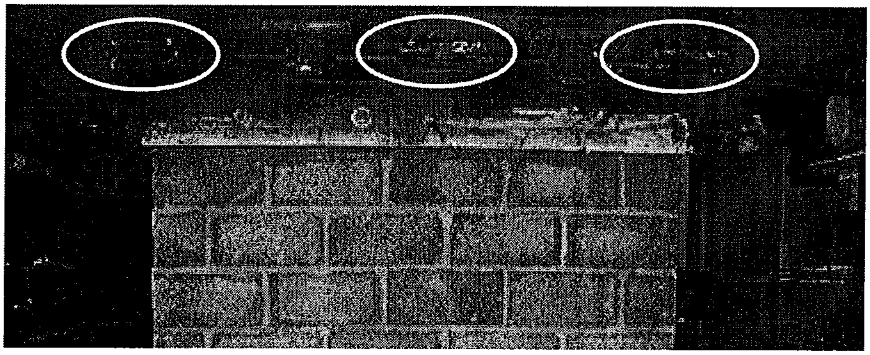

Figure 2.24: Tack welded mass to angle

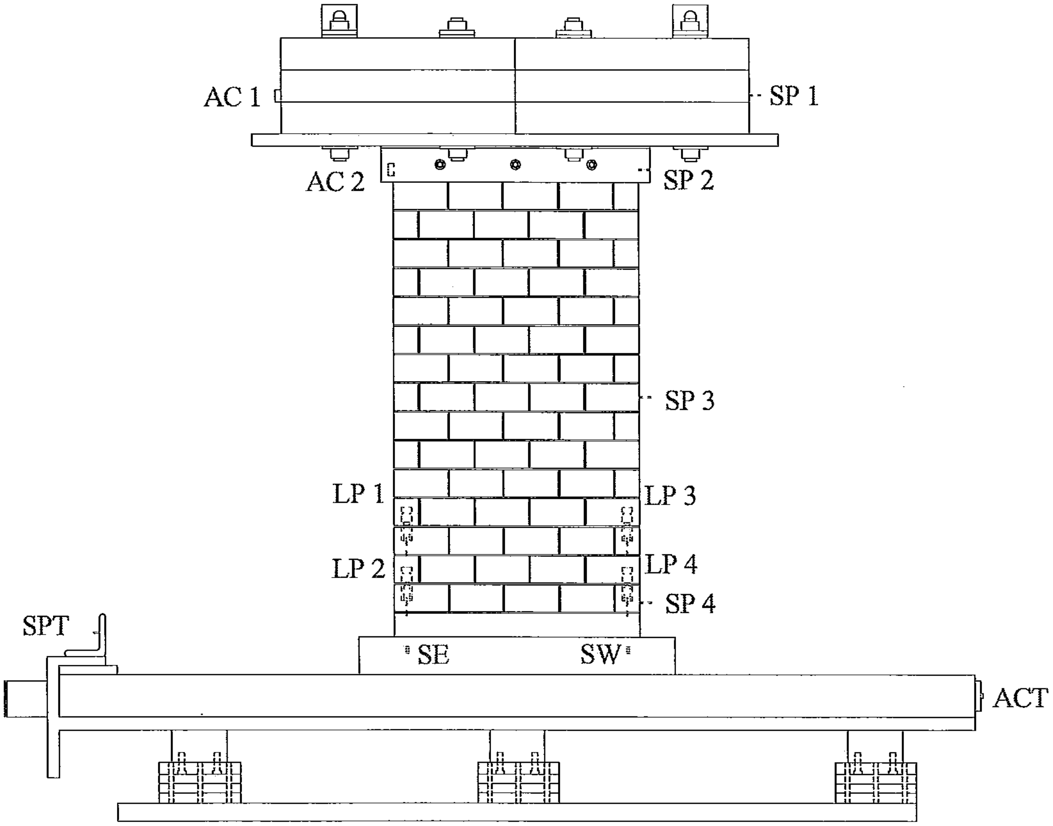

Figure 2.25: Instrumentation setup

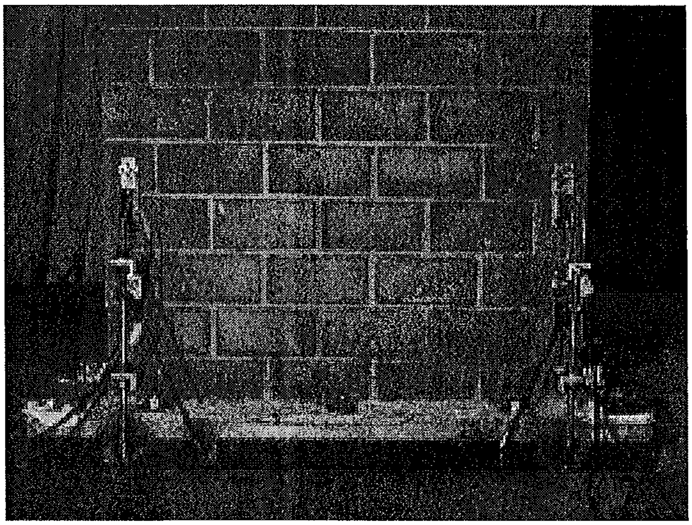

Figure 2.26: Instrumentation setup of linear potentiometers

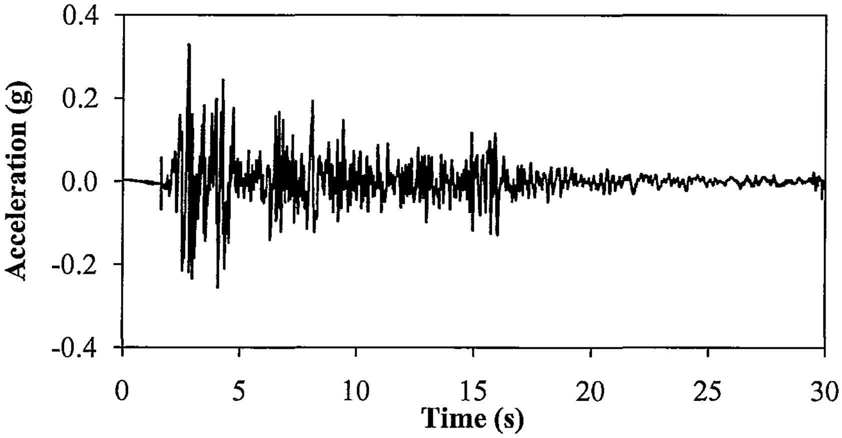

a) Acceleration time-history

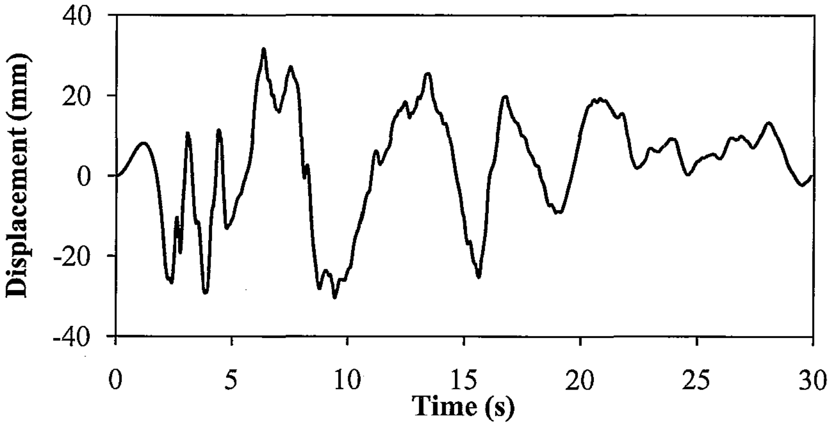

b) Displacement time-history

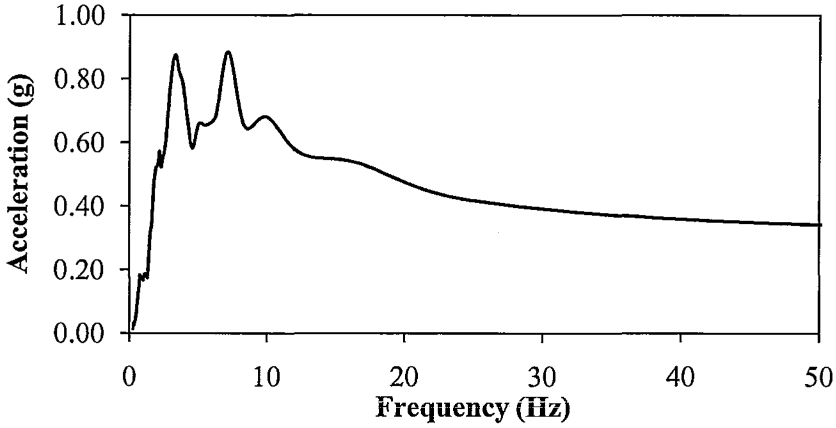

c) Response spectrum

Figure 2.27: El-Centro earthquake time-history and response spectrum

# CHAPTER 3: EXPERIMENTAL RESULTS

## 3.1 Introduction

The results of the dynamic tests are presented in this chapter. Originally, six walls were tested and grouped into three types, corresponding to Type I, II and III based on their vertical reinforcing ratios and configurations. Two identical walls were tested from each type; however, only the results from one of the Type III walls are included. The wall specimens are labelled by a roman numeral followed by a letter coding, A or B, representing the wall type and specimen identification (first or second specimen). For example, Type I Wall A will be referred to as Wall IA. For each wall, a discussion is presented pertaining to the progression of failure, load-displacement response, mode shape, frequency and damping. Figure 3.1 shows the direction labels used throughout the thesis. The positive displacements will be referred as the "positive region" and negative displacements will be referred to as the "negative region". In addition, the North face of the wall refers to the camera face where the progression of the damage is discussed in the General Observation sections. The South face refers to the opposite face of the camera. All photographs will be of the North face unless stated specifically.

Before any data was presented, the raw captured data of the walls were passed through a low-pass filter at a cut-off frequency of approximately 15 Hz to attenuate high-frequency noise.

The lateral force acting on the wall was calculated using the accelerations at the center-of-gravity of the mass and the accelerations at the mid-course of the bond beam. The accelerations were multiplied by the mass on top of the wall and the mass of half of the bond beam, respectively. The forces were added to estimate the final force acting at the mid-height of the bond beam, 29 mm from the top of the wall. The forces along with the displacements mid-height of the bond beam were used to plot the load-displacement graphs.

The mode shape of the wall was calculated from the measured lateral displacements captured by the string potentiometers attached to a reference frame at three points along the height of the wall; mid-height of the bond beam, mid-height of the wall and mid-height of the second course. The displacements of the walls were passed through an additional band-pass filter to attenuate noise around the natural frequency of the wall. The mode shape profiles are shown for the largest amplitude Run, I (PGD of 31.6 mm and PGA of 0.33 g). Three highest response profiles in each direction were selected and averaged to calculate the final mode shape of the wall.

From the rocking motion of the wall, the deflections at mid-height of the bond beam were calculated using the vertical displacements from the two linear potentiometers located on the fifth course. The vertical displacements at the ends of the wall were subtracted from each other and divided by their length to calculate the angle of rotation. The angle was multiplied by the height of the wall from the location of the crack to mid-height of the bond beam. Small angle approximation ($\tan\theta = \theta$) was used since the rotations were small. The calculated lateral deflections from the vertical linear potentiometers were compared to the measured lateral deflections of the wall.

The frequencies of the walls were measured from the hammer tap tests. While the wall was stationary, the mass on top of the wall would be struck with a rubber mallet, while the acceleration response of the wall was recorded. The corresponding frequency was found from the FFT of the response. Six hammer tap tests were performed before the start of testing and after each additional run.

The natural frequencies of the walls determined by the hammer tap test correspond to ambient level vibration amplitudes. As the frequency is amplitude dependent, ambient vibrations from the hammer tap test result in higher stiffness and frequency than expected for larger amplitude response, such as an earthquake. Although, the frequency from the hammer tap test was not representative of the natural frequency during the earthquake motion, a change of frequency was shown from the hammer tap tests that indicated the damage state of the wall was changing.

As a verification and estimate of the natural frequency of the wall, a Fast Fourier Transform (FFT) was taken between the acceleration response of the wall and the ground acceleration motion during the runs. The results from the FFT were able to show the peak Fourier amplitude near a specific frequency, which corresponded to the natural frequency of the wall. The FFT was able to estimate a more representative natural frequency at higher displacement amplitudes.

Typically, the peak Fourier amplitude was concentrated around a single frequency; however, the peak Fourier amplitude would be concentrated around several frequencies if the stiffness of the wall changed significantly during the same run.

The initial frequency of the wall was estimated by the FFT method from the response of the first Run, A, along with the initial hammer tap test. Since the walls had not sustained any damage, both methods were able to estimate a representative initial frequency.

The damping was calculated from the exponential curve fitted to the peaks of the sinusoidal acceleration response from the hammer tap tests and its associated natural frequency. The solution to under-damped systems is $\mathrm{u(t)} = \mathrm{e}^{-\zeta\omega_\mathrm{n}\mathrm{t}}(\mathrm{A}\cos\omega_\mathrm{D}\mathrm{t} + \mathrm{B}\sin\omega_\mathrm{D}\mathrm{t})$ where $\omega_\mathrm{D} = \sqrt{1-\zeta^2}\omega_\mathrm{n}$. The damped natural frequency, $\omega_D$, is less than the undamped natural frequency but for small damping ratios the difference is negligible. Both terms are used interchangeably for small damping ratios.

## 3.2 Type I Walls

Type I walls were vertically reinforced with 3.66 mm diameter steel bars in the two end cells ($\rho_v$= 0.12%) with a spacing of 469 mm (1.6 m at full scale). An axial load of 8.76 kN was placed on top of the wall during testing. No horizontal reinforcement was utilized in the wall. Two walls of Type I were tested under the same loading condition with letter coding of A and B, representing the first and second wall of that type tested.

### 3.2.1 Wall A

#### 3.2.1.1 General Observations

This was the first and only wall tested with the steel base. A vertical crack appeared in the bond beam during the final run. It was located in the flange part of the block and ran the whole length of the wall. It had most likely appeared during the rocking of the wall. In addition, a step crack formed on the east end of the wall, along with a horizontal bed joint crack in the first course, which extended the full length of the wall. After the initial set of tests with the steel base, a concrete base was added. Once the base course of the wall was removed, the existing cracks were no longer an issue.

Upon removal of the base course, a very thin mortar crack appeared in the second mortar joint course starting on the east side and ending in the third mortar joint course on the west side of the wall. This may be attributed to the fact that the mortar joint was weakened from the previous tests and during the removal of the base course. It is worth noting that the end cells were found to be fully grouted around the reinforcement when the base course was removed. The crack pattern after the addition of the concrete base is shown in Figure 3.2a.

Test runs were repeated with the concrete base. Besides the horizontal crack running through the second and third course mortar joints and the step crack in the lower east end of the wall, the first four Runs, A, B, C and D did not produce any new visible damage. The maximum lateral forces attained during Run A were 0.7 kN and 0.8 kN in the positive and negative displacement regions with maximum displacements of 0.2 mm and 0.1 mm, respectively. The lateral force continued to increase during the next three runs. During Run D, the maximum lateral forces were 2.3 kN and 1.9 kN in the positive and negative displacement regions, respectively, with maximum displacements of 1.0 mm in both directions.

The maximum lateral forces during Run E were 3.1 kN and 2.6 kN in the positive and negative displacement regions with maximum displacements of 1.7 mm and 1.6 mm, respectively. The horizontal mortar crack that was already present in the wall before the start of testing was opening up as much as 0.5 mm on the east side of the wall.

The first visible mortar crack from the new set of tests was found during Run G. It was located in the vertical mortar joint on the second course, mid-length of the wall. The crack extended from the already present bed joint crack. The maximum lateral loads were 3.6 kN and 3.4 kN in the positive and negative displacement regions with maximum displacements of 2.6 and 2.5 mm, respectively. The rocking of the wall on the second and third course mortar joint started to become visible during the run. Maximum vertical displacements of 1.0 mm and 0.7 mm were recorded on the east and west side of the wall, respectively.

In the final Run, I, the vertical mortar joint crack from Run G was extended horizontally in the west direction and continued down through the next vertical mortar joint all the way down to base. The maximum lateral loads were 3.7 kN in both the positive and negative displacement regions with maximum displacements of 4.1 and 3.3 mm, respectively. The forces attained during this run were approximately the same as in Run H with the exception of larger attained displacements. The final crack pattern of the wall up to and including Run I, is shown in Figure 3.2b.

Upon removal of the mass, the wall was slightly tilted out-of-plane about the second and third course mortar joint where the wall was separated from the bottom courses due to the horizontal mortar crack. Full collapse of the wall was prevented due to the vertical reinforcement holding the wall in place. The concrete base performed well during testing and did not show any signs of cracking.

#### 3.2.1.2 Load-Displacement Response

The overall hysteresis is shown in Figure 3.3. The response of the wall was non-symmetric due to the nature of the earthquake with higher displacements attained in the positive direction. The envelope response of the wall was linear elastic up to a load of 0.7 kN in the positive direction and 0.8 kN in the negative direction with displacements of 0.2 mm in both directions. Following the peak elastic loads, the stiffness decreased gradually for both displacement regions. A plateau was reached in the positive direction where the force remained constant under increased displacements. No defined yield point was attained in either direction.

A maximum lateral force of 3.7 kN was attained in the positive direction during the second last Run, H. The same maximum lateral force was attained in the negative direction but occurred during the last Run, I. The hysteresis loops of the runs started to develop noticeable stiffness degradation during the fifth Run, E, as shown in Figure 3.4. The response of the wall had a combination of high stiffness at smaller displacements and low stiffness at higher displacements due to the nature of the earthquake. It is worth noting that the hysteresis response in the negative region for the last two Runs, H and I, had almost the same response and stiffness. This was not the case in the positive direction where the last two runs had different stiffness degradation and energy dissipation response.

The loops before Run E were thin with negligible energy dissipation. During Run E and onwards, the area inside the loops started to increase in the positive displacement region, which indicated larger energy dissipation of the wall. As a result of the rocking motion, the wall was able to dissipate energy. Besides rocking, there was little damage to the wall, which accounted for the low energy dissipation before the fifth Run, E. In addition, larger loops developed in the positive region. This may be attributed to the non-symmetric earthquake and the variability of the material.

From the strain time-history profile recorded by the two end reinforcement strain gauges placed in top of the concrete base, it was difficult to identify at the exact point when the reinforcement in the wall had yielded. Selected run strain time-histories are shown in Figure 3.5. The east strain gauge had shown plastic strains throughout most of the runs. By Run G, the east strain gauge readings were starting to have an increased number of peaks at the same amplitude. This may have indicated a possible fault with the gauge. The west strain gauge had the opposite behaviour. However, both strain gauges were still able to record reasonable maximum strains. The east and west strain gauges reached yielding stains of $1.05\varepsilon_y$ and $1.00\varepsilon_y$, respectively.

### 3.2.1.3 Mode Shape

The mode shape of the wall is presented in Figure 3.6 as an average between negative and positive displacement regions of the last Run, I. The graph shows a linear mode shape, which is the result of the wall developing rocking motion on the second and third courses where a full length mortar crack developed. As there was no heel or toe crushing of the masonry and diagonal cracking, the wall was capable of retaining a linear shape.

The calculated displacements due to the rocking of the wall are presented in Figure 3.7. They are shown as a comparison to the measured displacements of the wall captured by the top wall string potentiometer (SP 2). The rocking motion had significant contributions to the lateral displacements of the wall. The displacements were in-phase but did not attain the same peak amplitudes. The measured displacements were higher, which included additional lateral displacements from the flexure and shear deformations that were not captured by the rocking motion.

### 3.2.1.4 Frequency and Damping

The initial average frequency of the wall before and after the addition of a concrete base was 7.4 Hz and 10.3 Hz, respectively. The addition of the concrete base increased the frequency by 39%.

The plot of the hammer tap test frequency is presented in Figure 3.8. With each additional run, the frequency of the wall was found to decrease. The final average frequency of the wall was 8.5 Hz. The hammer tap test was only able to determine the frequency at ambient vibrations; however, the frequencies were still found to decrease, thus, showing that the wall was progressively accumulating damage after each additional run. A plot of the representative frequency of the wall at larger earthquake amplitudes is presented in Figure 3.9 for selected runs. They were calculated by the FFT between the wall acceleration response and the ground acceleration. Run A had a peak amplitude at 9.1 Hz, which was close to the initial hammer tap test frequency. The final frequency of the wall was 5.3 Hz, as presented in Figure 3.9d. Figure 3.10 shows all the FFT frequencies superimposed on the same graph. The frequencies obtained by the FFT and hammer tap test method are summarized in Table 3.1.

The damping values are presented in Figure 3.11. The initial average critical damping was estimated to be 1.8% from the hammer tap test. The graph shows a positive trend in the progression of damping values. The last damping value is slightly smaller than the previous value. This may be due to the fact that the hammer tap test was not able to induce higher response in the walls to account for any increase in damping. The final average damping of the wall after Run I was 4.2%. One must keep in mind that the damping values obtained from the hammer tap test are at ambient vibrations and are not representative damping values that would be obtained during earthquake displacements. The ambient damping values only show a change within the wall caused by the accumulated damage.

### 3.2.2 Wall B

#### 3.2.2.1 General Observations

Upon inspection of the wall before testing, the South face was found to have several mortar joint chips. Figure 3.12 shows the location of the mortar chips, along with a close-up view in Figure 3.13. They were thought not to have any significant influence over the test results as they were located higher up the wall. Most likely they were attributed to mortar shrinkage.

During the initial Run, A, no cracking was found. The wall experienced maximum lateral forces of 0.7 kN and 0.8 kN in the positive and negative directions with maximum displacements of 0.2 mm and 0.3 mm, respectively. The lateral forces imposed on the wall were still within the cracking limit of 1.3 kN.

The second Run, B, caused two mortar cracks to appear in the head joints. They were located in the first and third courses, two block lengths from the west end of the wall, as shown in Figure 3.14a. The maximum lateral forces acting on the wall were 1.3 kN and 1.4 kN in the positive and negative directions, respectively, with maximum displacements of 0.3 mm in both directions.

A horizontal bed mortar joint crack five mm in length started to appear during Run C. It was located in the third mortar joint course at the east end of the wall. The crack did not propagate any further during additional runs. The maximum lateral forces were 1.7 kN and 1.6 kN in the positive and negative directions with maximum displacements of 0.3 mm and 0.4 mm, respectively.

During the fourth Run, D, the maximum lateral loads were increased to 2.2 kN and 2.12 kN in the positive and negative directions with maximum displacements of 0.9 mm and 0.7 mm, respectively. The positive displacement had increased by 159% while the negative displacement only increased by 69%. New horizontal joint cracks appeared in the fourth mortar joint course on the east end of the wall and in the third mortar joint course on the west end of the wall. Three additional vertical joint cracks were seen in the third, eight and eleventh courses, along with two other small vertical mortar cracks. The complete cracking pattern of the wall up to and including Run D, is shown in Figure 3.14b. The maximum uplifts at both ends of the wall were 0.2 mm.

During Run E, the only new damage observed was a horizontal mortar crack in the third mortar joint course located near the top of the wall on the west side. The maximum lateral loads were 3.0 kN and 2.3 kN in the positive and negative directions with maximum displacements of 1.1 mm and to 1.0 mm, respectively. The maximum uplift of the wall increased to 0.3 mm.

During Run F, two significant cracks appeared on the wall. The first crack propagated from an existing vertical joint crack found in Run D. The second vertical joint crack was located in the fifth course from the top of the wall. Other small cracks appeared in the joints throughout the wall. The crack pattern up to and including Run F, is shown in Figure 3.14c. The maximum lateral forces were increased to 3.3 kN and 2.5 kN in the positive and negative directions with maximum displacements of 1.5 mm and 1.2 mm, respectively. The maximum uplifts were increased to 0.4 mm and 0.3 mm on the east and west ends, respectively.

There was no new damage observed during Run G. However, the maximum lateral loads were reduced to 3.2 kN and 2.4 kN in the positive and negative directions, respectively. The lateral displacements remained identical to the previous run.

During Run H, a horizontal mortar joint crack appeared in the first mortar course spanning the whole length of the wall. The maximum uplifts on both sides of the wall were almost 1 mm. The wall was seen rocking on the first course. The maximum resisting lateral loads were increased to 3.7 kN and 3.2 kN in the positive and negative directions with maximum displacements of 3.0 mm and 2.4 mm, respectively.

In the last Run, I, the wall continued to rock on the first course. A vertical step crack formed on the east end of the wall propagating from an existing horizontal crack. The maximum recorded lateral forces were 3.9 kN and 3.6 kN in the positive negative directions with maximum displacements of 5.2 mm and 4.4 mm, respectively. The final crack pattern of the wall up to and including Run I, is shown in Figure 3.14d.

#### 3.2.2.2 Load-Displacement Response

The overall hysteresis is shown in Figure 3.15. The response of the wall was non-symmetric due to the nature of the earthquake with larger displacements occurring in the positive direction. The hysteresis envelope showed a linear elastic behaviour up to loads of 1.5 kN and 2.1 kN in the positive and negative directions with of displacement of 0.3 mm and 0.5 mm, respectively. The maximum loads attained in the positive and negative direction were 3.9 kN and 3.6 kN, respectively. The hysteresis loops started to develop noticeable stiffness degradation during Run D, as shown in Figure 3.16.

Prior to Run H, the hysteresis loops were thin with little energy dissipation. Negligible amount of damage was present in the wall and rocking had not yet initiated. Upon development of the horizontal mortar crack running the full length of the wall, higher energy dissipation was observed, as seen by the larger size hysteresis loops in Figure 3.17.

The strain profile was recorded by the two end reinforcement strain gauges located just below the base of the wall. The east end reinforcement strain gauge did not capture accurate results as it was damaged during the pouring of the concrete base. Selected strain time-history profiles are presented in Figure 3.18. Maximum strains of $0.17\varepsilon_y$, $0.77\varepsilon_y$, and $1.27\varepsilon_y$ were attained for Runs G, H and

I, respectively. All three strain profiles had progressive increase in strain, as well as a permanent strain deformation after the onset of the most intense ground motion.

### 3.2.2.3 Mode Shape

The mode shape of the wall is presented in Figure 3.19 as an average between the negative and positive displacement regions of the last Run, I. The profile shows a linear mode shape due to rocking motion of the wall.

The deflections from the rocking motion of the wall were calculated and compared to the measured top displacements. They are presented in Figure 3.20. The rocking of the wall took place about the first course and had large contributions to the lateral displacement of the wall. The displacements between the measured and calculated values are in-phase; however, the calculated values had slightly lower amplitudes. This was due to the exclusion of lateral displacements attributed to flexure and shear deformations that were not captured by the rocking motion.

### 3.2.2.4 Frequency and Damping

The plot of the frequency from the hammer tap tests is presented in Figure 3.21. The initial and final average frequency of the wall was 11.9 Hz and 10.6 Hz, respectively. With each progressive run, the wall experienced a decrease in frequency. The change between the initial and final frequency was 1.4 Hz. A more representative frequency of the wall at larger earthquake amplitudes is calculated by the FFT between the wall acceleration response and the ground acceleration. The frequency for selected runs is presented in Figure 3.22. The initial frequency of Run A was 12.5 Hz. This value agreed well the initial hammer tap test frequency. The final frequency was estimated to be between 5 Hz and 7 Hz. There was a range of values, since there were several peak amplitudes present across a range of frequencies due to the change in stiffness of the wall in the same run. Figure 3.23, shows all the FFT frequencies superimposed on the same graph. In addition, Table 3.2 presents the frequencies obtained from the FFT and hammer tap test method.

The damping values from the hammer tap test are presented in Figure 3.24. An initial average damping value of 2% was estimated. After Run A, the average damping of the wall decreased to 1.2%. The damping values followed an increasing positive trend after Run A. The final average damping value of the wall was 1.9%. These damping values only show a change between the state of the wall at ambient vibrations.

## 3.3 Type II Walls

Type II walls were vertically reinforced with 3.66 mm diameter steel bars in the two end cells and mid-length of the wall ($\rho_v$= 0.17%) with even spacing of 235 mm (782 mm at full scale). An axial load of 8.76 kN was placed on top of the wall during the testing. No horizontal reinforcement was utilized in the wall. Two walls of Type II were tested under the same loading condition with letter coding of A and B, representing the first and second wall of that type tested.

### 3.3.1 Wall A

#### 3.3.1.1 General Observations

Upon inspection of the South face, four vertical mortar joints were found separated from the block. The mortar joint separation is shown in Figure 3.25. No defects were found on the North face.

The first Run, A, did not produce any damage. The maximum lateral load forces were 1.0 kN and 1.2 kN in the positive and negative directions, respectively, with maximum displacements of 0.2 mm in both directions.

During Run B, the wall was found to vibrate in the out-of-plane direction. The lateral supports ensured that the mass did not tip over and cause damage to the wall. The maximum lateral load forces were 1.7 kN and 1.8 kN in the positive and negative directions, respectively, with maximum displacements of 0.3 mm in both directions.

No visible damage occurred during Runs C, D and E. The maximum lateral forces during Run D were 3.6 kN and 3.3 kN in the positive and negative directions with displacements of 0.8 mm and 0.7 mm, respectively. Run E had the maximum lateral force increase to 3.7 kN in the positive direction and decrease to 3.1 kN in the negative direction with maximum displacements of 0.9 mm in both directions.

During the sixth Run, F, no damage was observed upon the inspection of the wall. The maximum lateral forces were 3.5 kN in the positive direction (decrease of 3.7% from the previous run) and 3.7 kN (increase of 18.9% from the previous run) in the negative direction with maximum displacements of 1.3 mm and 0.9 mm, respectively.

Four new mortar joints cracks (five mm in length) appeared during Run G. The first crack was found in the head mortar joint located in the first course mid-length of the wall. The second horizontal bed joint crack was located in the second course mid-length of the wall. The last two mortar cracks were located around the corner of the second course half-block on the west end of the wall. The crack pattern of the wall up to and including Run G, is shown in Figure 3.26a. The maximum lateral forces were 4.5 kN and 3.9 kN in the positive and negative directions with maximum displacements of 1.1 mm and 1.6 mm, respectively. The maximum uplifts on the east and west ends of the wall were 0.4 mm and 0.2 mm, respectively.

After Run H, several new vertical mortar cracks appeared in the head joints located in the first two courses. The cracking pattern up to and including Run H, is shown in Figure 3.26b. The maximum lateral forces were 3.8 kN (15.6% decrease from the previous run) in the positive direction and 4.1 kN (5.1% increase from the previous run) in the negative direction with maximum displacements of 1.2 mm and 1.7 mm, respectively.

During the last Run, I, several new cracks were observed. A step crack developed in the lower east end of the wall that consisted of a vertical and horizontal mortar joint crack. Another step crack formed on the west end of the wall from an already existing crack in the third mortar joint course. The cracking pattern up to and including Run I, is shown in Figure 3.26c. As a result of the horizontal cracks, the maximum uplifts were 0.6 mm and 0.3 mm at the east and west ends, respectively. The maximum lateral forces acting on the wall were 4.4 kN (15.7% increase from the previous run) in the positive direction and 4.1 kN (no change from the previous run) in the negative direction with maximum displacements and 2.4 mm and of 1.5 mm, respectively.

The wall had not developed a full length horizontal crack and thus, no rocking motion of the wall observed. The wall was subjected to a tenth run. A full length horizontal mortar joint crack formed and the wall started to rock. The results from the extra test are not included since the other walls were not subject to the additional run.

### 3.3.1.2 Load-Displacement Response

The overall hysteresis is shown in Figure 3.27. The response of the wall was non-symmetric due to the nature of the earthquake with larger displacements attained in the positive direction. The wall was observed to have linear behaviour up to a higher force and displacement values than compared to that of Type I walls. The wall had linear stiffness up to 3.6 kN and 3.8 kN in the positive and negative directions, respectively, with displacements of 0.7 mm in both directions. After the peak elastic force was attained in the positive direction, the stiffness changed abruptly due to a decrease in lateral load carrying capacity. A sudden loss in load carrying capacity was also present in the negative direction after reaching the maximum load. Neither direction developed a plateau of constant force, which suggested that the wall had not reached its ultimate strength.

The maximum lateral loads in the positive and negative directions occurred at different runs. In the positive direction, the maximum lateral load was 4.4 kN, recorded during the last Run, I. The maximum lateral load in the negative direction was 4.5 kN, recorded during last third Run, G. The last two Runs, H and I, had a constant lateral force of 4.1 kN in the negative region at displacements of 1.2 mm and 1.5 mm, respectively. The wall had started to develop noticeable stiffness degradation during Run F as shown in Figure 3.28. The size of the loops was small, which indicated a lack of energy dissipation. This was due to the undamaged state of the wall with no significant rocking motion.

The strain time-history profile of the end reinforcement is shown in Figure 3.29. The strain profile is only presented for the last Run, I, as there was not any significant change between any of the other runs. The maximum strain reading before the last run was $0.05\varepsilon_y$. During the last Run, I, the strains in the east and west end reinforcements were $0.73\varepsilon_y$ and $0.53\varepsilon_y$, respectively. The steel had not yielded near the base of the wall.

### 3.3.1.3 Mode Shape

The mode shape of the wall is presented in Figure 3.30 as an average between negative and positive displacement regions of the last Run, I. The graph shows an almost linear mode shape. This may be attributed to the wall not developing significant rocking motion.

The deformations at the top of the wall are shown in Figure 3.31 as a comparison between the calculated and measured lateral deflections. The wall did not undergo as intense rocking motion as for the previous walls; hence, the measured lateral deflections from the rocking were significantly lower than the measured values. Only several instances were found where the calculated values had significant contributions to the lateral displacements.

#### 3.3.1.4 Frequency and Damping

The frequency from the hammer tap tests is shown in Figure 3.32. The average initial frequency of the wall was 12.0 Hz. For the first four Runs, A through D, the frequency of the wall remained relatively the same. Starting at Run E, the average frequency decreased to 11.9 Hz, which indicated that the wall started to sustain some damage that was able to be captured by the hammer tap test. The final average frequency of the wall was 11.2 Hz. A plot of the natural frequency calculated by the FFT between the acceleration response of the wall and the ground acceleration is presented in Figure 3.33 for selected runs. The FFT is able to show a more representative frequency of the wall at larger earthquake amplitudes. The initial frequency was 11.9 Hz, which agreed well with the initial hammer tap test frequency. During Run E, the frequency decreased to 10.9 Hz. The final Run, I, had a frequency range between 7 Hz and 10.5 Hz, as shown in Figure 3.34b. Figure 3.34 shows all the FFT frequencies superimposed on the same graph. In addition, Table 3.3 presents the frequencies obtained from the FFT and hammer tap test method.

The damping values from the hammer tap test are shown in Figure 3.35. The average initial damping value of the wall was 1.2%. However, after the first Run, A, the damping decreased to an average value of 1.0%. In addition, the damping of Runs, F and H, were larger than the last run damping value. The general trend showed an increase in the damping values.

### 3.3.2 Wall B

#### 3.3.2.1 General Observations

The initial inspection of the wall revealed four mortar joint defects where the mortar was chipped or de-bonded from the block. These defects may have been cosmetic, thus, would have no effect on the response of the wall. The locations of the defects on the North face are shown in Figure 3.36a. Two were located near the top of the wall, one mid-height of the wall and the other was located in the third course from the base. The opposite face of the wall (South face) revealed the same type of defects with many of them present in the mid and top portions of the wall.

The first Run, A, did not cause any damage. The wall experienced maximum lateral loads of 0.8 kN and 0.7 kN in the positive and negative directions, respectively, with maximum displacements of 0.2 mm in both directions.

During Run B, new mortar chippings were found in the east and west corners of the wall. On the South face, the previous mortar defects became larger and deeper. At one location, the mortar chipped off completely through the width of the face shell. The mortar chips did not deteriorate any further as testing continued. The maximum lateral forces experienced by the wall were 1.5 kN and 1.3 kN in the positive and negative directions with maximum displacements of 0.4 mm and 0.3 mm, respectively.

No visible damage was found during Runs, C and D. The maximum lateral forces and maximum displacements became larger as the amplitude of the simulated earthquake was increased. By Run D, the maximum lateral loads experienced by the wall in the positive and the negative directions were identical at 2.0 kN with maximum displacements of 0.6 mm in both directions.

After the inspection of Run E, new mortar joint cracks had formed, which were concentrated in the fourth and fifth courses located on both ends of the wall. The cracking pattern up to and including Run E, is shown in Figure 3.36b. The maximum lateral forces acting on the wall were 2.7 kN and 2.4 kN in the positive and negative directions with maximum displacements of 0.8 mm and 0.9 mm, respectively. The maximum uplifts recorded on the east side and west side of the wall were both 0.1 mm.

Three new mortar cracks appeared during Run F. The cracking pattern up to and including Run F, is shown in Figure 3.36c. The first crack was located mid-length of the wall. The second crack was located near the top east end of the wall and the third crack was located near the bottom west of the wall. The maximum lateral forces acting on the wall were 3.2 kN and 2.7 kN in the positive and negative directions, respectively, with maximum displacements of 1.1 mm in both directions.

A crack was observed at the base of the wall after Run G. The maximum uplift of the wall was 0.2 mm. The already present mortar cracks were progressively increasing in width. The maximum lateral loads were 4 kN and 3.3 kN in the positive and negative directions with maximum displacements of 1.4 mm and 1.3 mm, respectively.

During Run H, a full length crack formed at the base of the wall, which resulted in rocking. The maximum uplifts were 0.5 mm on both east and west sides of the wall. An additional mortar crack formed around the corner of the first course block located at the east end of the wall. The maximum lateral loads were decreased to 3.8 kN (5% decrease from the previous run) in the positive direction and increased to 4.4 kN (33% increase from the previous run) in the negative direction with maximum displacements of 2.0 mm and 2.2 mm, respectively.

By the end of Run I, the wall was rocking on the concrete base with maximum uplift of 1.3 mm. The maximum lateral loads were 4.6 kN (4% increase from the previous run) in the positive direction and 4.2 kN (5% decrease from the previous run) in the negative direction with maximum displacements of 3.3 mm and 3.8 mm, respectively. The cracking pattern up to and including Run I, is shown in Figure 3.36d.

### 3.3.2.2 Load-Displacement Response

The overall hysteresis is shown in Figure 3.37. The response of the wall was non-symmetric due to the nature of the earthquake. Higher displacements were attained in the negative direction. From the hysteresis envelope, the wall remained essentially linear elastic up to loads of 3.8 kN and 1.6 kN in the positive and negative directions with displacements of 1.0 mm and 0.4 mm, respectively. Both displacement regions lacked a constant plateau, which suggested the ultimate capacity of the wall was not reached. In the positive direction, a maximum lateral force of 4.6 kN was attained during the last Run, I, with displacement of 3.3 mm. In the negative direction, a maximum lateral force of 4.4 kN was attained during the second last Run, H, with displacement of 2.1 mm. This was followed by a decrease in lateral force to 4.2 kN during the last Run, I. There was also gap in the positive displacement region where the response of the wall did not fully develop during Run H.

The only noticeable stiffness degradation was during Runs H and I. The hysteresis of both runs is presented in Figures 3.38a and 3.38b. The hysteresis loops were narrow until rocking motion developed during Run H. Both Runs, H and I, had large hysteresis loops associated with the onset of energy dissipation. More prominent and larger size loops were present in the negative displacement region.

Only the east reinforcement strain gauge was operational. The strain time-history profile of the last two runs is presented in Figure 3.39. In the final Run, I, the maximum strain was $0.46\varepsilon_y$.

### 3.3.2.3 Mode Shape

The mode shape of the wall is presented in Figure 3.40 as an average between the negative and positive displacement regions of the last Run, I. The wall had a linear mode shape due to the rocking motion of the wall on top of the concrete base.

Figure 3.41 shows the comparison between the measured and calculated lateral deflections of the wall caused by the rocking motion. The rotations were multiplied by the full height of the wall minus half the bond beam course since the rocking occurred at the base. The same peak amplitudes were not attained; however, the rocking of the wall had significant contributions to the lateral deflections of the wall.

### 3.3.2.4 Frequency and Damping

The hammer tap test frequency of is presented in Figure 3.42. The initial and final average frequency of the wall was 11.9 Hz and 10.6 Hz, respectively. A plot of the natural frequency calculated by FFT between the acceleration response of the wall and ground acceleration is presented in Figure 3.43 for selected runs. The FFT method was able to estimate representative frequencies of the wall at higher earthquake amplitudes unlike the hammer tap test. The initial frequency of

Run A was 10.9 Hz. The difference between the initial hammer tap test and FFT frequency can be attributed to the cracks that were present in the wall before start of testing. The hammer tap test was only able to induce ambient amplitudes in the wall, thus, the cracks do not have any effect on the stiffness. The FFT frequency of the wall remained identical for Runs A, B, and C. It was slightly decreased during Run D and remained identical for Runs E, F and G. It was not until Runs H and I, where the frequency had decreased significantly due to the rocking motion. The final frequency of the wall was 5.4 Hz. Figure 3.44 shows the FFT frequencies superimposed on the same graph. In addition, Table 3.4 presents the frequencies obtained from the FFT and hammer tap test method.

The average damping values from the hammer tap test are presented in Figure 3.45. The initial damping of the wall was 1.9%. The first Run, A, had an average damping value of 1.2%, which was lower than the initial value. A positive trend was found between the increasing damping values after Run A. This indicated that the wall was accumulating damage. The final average damping was 1.9%.

### 3.4 Type III Wall

Type III wall was vertically reinforced with 4.78 mm diameter steel bars in the two end cells ($\rho_v$= 0.20%) with spacing of 469 mm (1.6 m at full scale). An axial load of 8.76 kN was placed on top of the wall during testing. No horizontal reinforcement was utilized in the wall. Originally, two walls of this type were built but only one wall with the concrete base was included in the results. The other wall with the steel base was too damaged to be tested again with the concrete base. The wall had a letter coding of A, representing the first and only wall of that type tested.

### 3.4.1 Wall A

#### 3.4.1.1 General Observations

Upon inspection of the wall, the mortar had de-bonded from the block at several locations. The observed defects were only present on the North face of the wall. The locations of de-bonding are shown in Figure 3.46a.

The first mortar cracks appeared in the wall during the second Run, B. An existing de-bonded mortar joint was extended the full length of the block. The crack was located in the third course on the west side of the wall. The maximum lateral forces were 1.3 kN and 1.0 kN in the positive and negative directions with maximum displacements of 0.4 mm and 0.5 mm, respectively.

During the next Run, C, the horizontal mortar crack from the previous run was extended another full block length to join an already present vertical de-bonded joint. The cracking pattern up to and including Run C, is shown in Figure 3.46b. The maximum lateral forces were 1.6 kN and 1.3 kN in the positive and negative directions, respectively, with maximum displacements of 0.6 mm in both directions.

A new horizontal joint crack, half a block in length appeared during Run D. It was located in the sixth course on the east end of the wall. The maximum lateral forces were 2.1 kN and 1.5 kN in the positive direction and negative directions with maximum displacements of 0.8 mm and 0.7 mm, respectively.

Run E had caused the existing cracks to become wider. The maximum uplift displacements were 0.3 mm at both ends of the wall. The maximum lateral forces were 2.9 kN and 2.3 kN in the positive and negative directions with maximum displacements of 1.3 mm and 1.1 mm, respectively.

During Run F, a bed joint mortar crack appeared in the second mortar course located on the east end of the wall. The crack extended one and a half block lengths from the edge of the wall. The cracking pattern up to and including Run F, is shown in Figure 3.46c. The maximum uplift was 0.5 mm at both ends of the wall, double of the previous run. The maximum lateral forces were 3.5 kN and 3.0 kN in the positive and negative directions, respectively, with maximum displacements of 1.9 mm in both directions.

The next higher amplitude Run, G, resulted in the extension of four previous mortar joint cracks. The maximum lateral forces were 3.8 kN and 3.4 kN in the positive and negative directions with maximum displacements of 2.5 mm and 2.3 mm, respectively.

During Run H, two horizontal cracks located on the east and west ends were fully extended across the whole length of the wall, which resulted in rocking. The cracking pattern up to and including Run H, is presented in Figure 3.46d. The maximum uplifts were 1.3 mm and 1.2 mm on the east and west ends of the wall, respectively. The maximum lateral force was 4.1 kN with a displacement of 3.5 mm in both directions.

The last Run, I, had a set of steps cracks form, which extended from a previous horizontal crack to the bottom of the foundation. The final crack pattern of the wall up to and including Run I, is presented in Figure 3.46e. The maximum lateral loads were increased to 4.4 kN (6.5 % increase from the previous run) in the positive direction and decreased to 4.0 kN (3.7 % decrease from the previous run) in the negative direction with maximum displacements of 6.8 mm and 6.1 mm, respectively.

### 3.4.1.2 Load-Displacement Response

The overall hysteresis is shown in Figure 3.47. The response of the wall was non-symmetric due to the nature of the earthquake with higher displacements attained in the positive direction. The wall had a linear elastic behaviour up to a load of 0.7 kN with displacement of 0.2 mm in both directions. The hysteresis envelope was smooth with progressively decreasing stiffness until a constant plateau developed. The positive direction had a longer yield plateau than that of the negative direction where there was a slight reduction in force.

A maximum positive lateral load of 4.4 kN with displacement of 6.8 mm was attained during the last Run, I. In the negative direction, a maximum lateral force of 4.1 kN with displacement 4.1 mm was attained during the second last Run, H. This was followed by a reduction in lateral force to 4.0 kN with displacement of 6.1 mm.

The response of the last two Runs, H and I, had noticeable stiffness degradation and energy dissipation. The hysteresis of Runs H and I, are presented in Figure 3.48. The loops had become significantly larger after rocking initiated. This indicated that the wall was able to dissipate energy through the rocking motion. The last Run, I, had the widest loops and hence, the largest energy dissipation.

The strain time-history of the end reinforcement is presented in Figure 3.49 for the last two Runs, H and I. Only the strain gauge located on the east end was functioning. Runs H and I, had maximum strains of $0.67\varepsilon_y$ and $2.50\varepsilon_y$, respectively. After reaching the maximum strain during Run I, the gauge stopped recording data.

### 3.4.1.3 Mode Shape

The mode shape of the wall is presented in Figure 3.50 as an average between negative and positive displacement regions of the last Run, I. The wall had a linear mode shape due to the rocking motion of the wall on the second and third courses.

Figure 3.51 shows the comparison between the measured and calculated lateral deflections of the wall. The peak amplitudes between the measured and calculated lateral deflection were not the same; however, the rocking motion had significant contributions to the lateral deflections.

#### 3.4.1.4 Frequency and Damping

The hammer tap test frequency is presented in Figure 3.52. The average initial frequency of the wall was 9.1 Hz and gradually decreased to 7.0 Hz (Run G). After the run, the frequency of the wall increased slightly. The final average frequency of the wall was 7.8 Hz (Run I). A plot of the natural frequency calculated by FFT between the acceleration response of the wall and ground acceleration is presented in Figure 3.53 for selected runs. The initial frequency was 8.8 Hz, which was similar to initial frequency obtained from the hammer tap test. All the FFT frequencies had a single peak except the last Run, I, where several peak amplitudes were concentrated between 4 Hz and 6 Hz. Figure 3.54 shows all the FFT frequencies superimposed on the same graph. In addition, Table 3.5 presents the frequencies obtained from the FFT and hammer tap test method.

The damping values from the hammer tap test are presented in Figure 3.5. The initial average damping of the wall was 2.4%. After the first Run, A, the damping decreased slightly to an average of 2.3% and then gradually increased to a maximum damping value of 4.3% (Run G). The final average damping was 3.7% (Run I). The damping values followed a similar mirror trend as that of the hammer tap test frequencies.

### 3.5 Closure

The results of the walls were reported in detail. The observation and progression of cracking was discussed. The walls had rocking motion when a full length mortar crack developed in the lower courses. No diagonal cracking or crushing of the masonry was observed during testing. The rocking motion had significant contributions to the lateral deflections of the wall with the exception of Wall IIA where the wall did not rock as severely. Load-displacement hysteresis loops were presented and discussed. All the walls had yielded and developed inelastic deformations. The ultimate response of the walls was not attained due to the limited capacity of the actuator. Sample strain profiles of the reinforcement were presented and had shown to yield at larger amplitude runs. All the walls had a linear mode shape due to the rocking motion. The last section discussed the frequency and damping values. The frequencies were shown to decrease due to the mortar joint cracks and rocking of the wall. The walls were able to dissipate energy through the rocking motion at higher amplitude runs.

Table 3.1: Wall IA frequencies and damping from the hammer tap test and FFT

| **Run** | **Hammer Tap Test** | | **FFT** |
|---|---|---|---|
| | **Frequency (Hz)** | **Critical Damping (%)** | **Frequency (Hz)** |
| Initial | 10.3 | 1.8 | n/a |
| A | 9.6 | 2.4 | 9.2 |
| B | 9.2 | 3.3 | 8.3 |
| C | 9.1 | 3.5 | 8.3 |
| D | 9.0 | 3.7 | 7.7 |
| E | 9.0 | 3.7 | 7.5 |
| F | 9.0 | 4.0 | 7.0 |
| G | 8.7 | 4.0 | 6.2 |
| H | 8.4 | 4.2 | 5.5 |
| I | 8.4 | 4.0 | 5.3 |

Table 3.2: Wall IB frequencies and damping from the hammer tap test and FFT

| **Run** | **Hammer Tap Test** | | **FFT** |
|---|---|---|---|
| | **Frequency (Hz)** | **Critical Damping (%)** | **Frequency (Hz)** |
| Initial | 11.9 | 2.0 | n/a |
| A | 11.9 | 1.2 | 12.5 |
| B | 11.8 | 1.3 | 11.8 |
| C | 11.5 | 1.3 | 11.8 |
| D | 11.6 | 1.5 | 10.6 |
| E | 11.6 | 1.4 | 10.7 |
| F | 11.5 | 1.5 | 10.5 |
| G | 11.5 | 1.6 | 11.6 |
| H | 10.9 | 1.7 | 6.2 |
| I | 10.6 | 1.9 | 6.3 |

Table 3.3: Wall IIA frequencies and damping from the hammer tap test and FFT

| **Run** | **Hammer Tap Test** | | **FFT** |
|---|---|---|---|
| | **Frequency (Hz)** | **Critical Damping (%)** | **Frequency (Hz)** |
| Initial | 12.0 | 1.3 | n/a |
| A | 12.0 | 1.0 | 11.9 |
| B | 12.0 | 1.3 | - |
| C | 12.0 | 1.5 | 11.9 |
| D | 12.0 | 1.3 | 11.8 |
| E | 11.9 | 1.7 | 10.9 |
| F | 11.8 | 2.9 | 10.6 |
| G | 11.7 | 1.9 | 10.3 |
| H | 11.2 | 3.1 | 8.5 |
| I | 11.2 | 1.9 | 8.3 |

Table 3.4: Wall IIB frequencies and damping from the hammer tap test and FFT

| **Run** | **Hammer Tap Test** | | **FFT** |
|---|---|---|---|
| | **Frequency (Hz)** | **Critical Damping (%)** | **Frequency (Hz)** |
| Initial | 11.9 | 2.0 | n/a |
| A | 11.9 | 1.2 | 10.9 |
| B | 11.8 | 1.3 | 10.6 |
| C | 11.5 | 1.3 | 9.8 |
| D | 11.6 | 1.5 | 9.3 |
| E | 11.6 | 1.4 | 8.8 |
| F | 11.5 | 1.5 | 8.5 |
| G | 11.5 | 1.6 | 7.9 |
| H | 10.9 | 1.7 | 6.3 |
| I | 10.6 | 1.9 | 5.4 |

Table 3.5: Wall IIIA frequencies and damping from the hammer tap test and FFT

| **Run** | **Hammer Tap Test** | | **FFT** |
|---|---|---|---|
| | **Frequency (Hz)** | **Critical Damping (%)** | **Frequency (Hz)** |
| Initial | 9.1 | 2.4 | n/a |
| A | 9.0 | 2.2 | 8.9 |
| B | 8.8 | 2.3 | 8.3 |
| C | 8.5 | 2.8 | 8.3 |
| D | 8.2 | 3.1 | 7.8 |
| E | 7.8 | 3.7 | 7.1 |
| F | 7.3 | 4.1 | 6.7 |
| G | 7.0 | 4.3 | 6.3 |
| H | 7.2 | 3.2 | 5.4 |
| I | 7.7 | 3.7 | 5.1 |

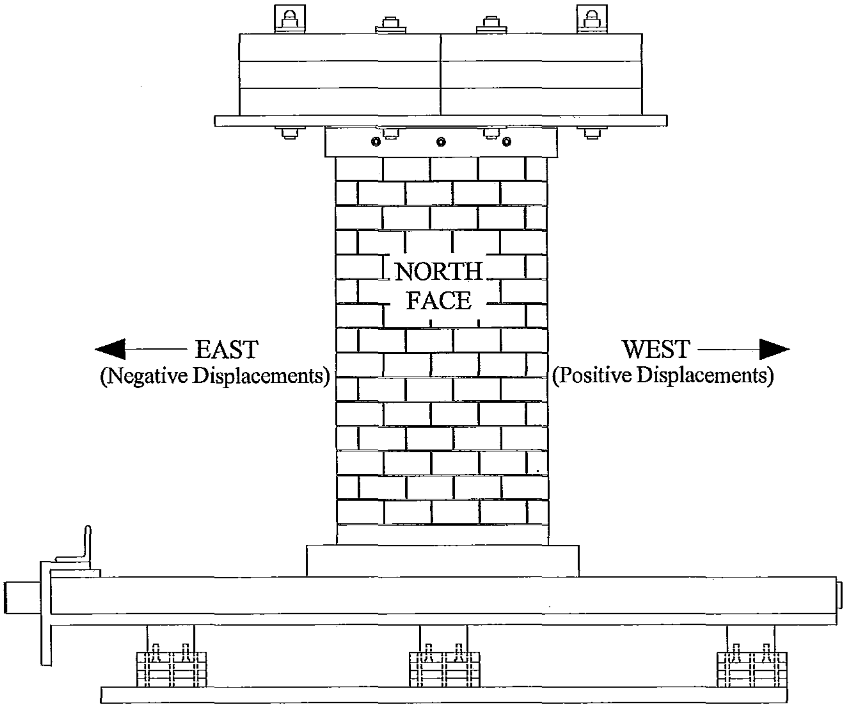

Figure 3.1: Orientation of the wall with depicted east (negative) and west (positive) directions

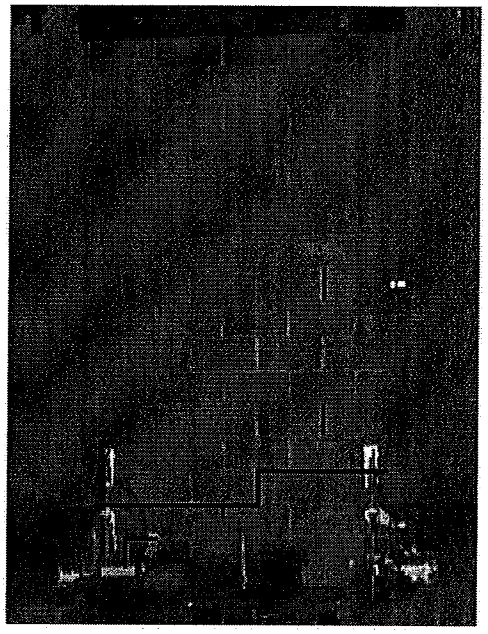

a) Crack pattern after addition of the concrete base

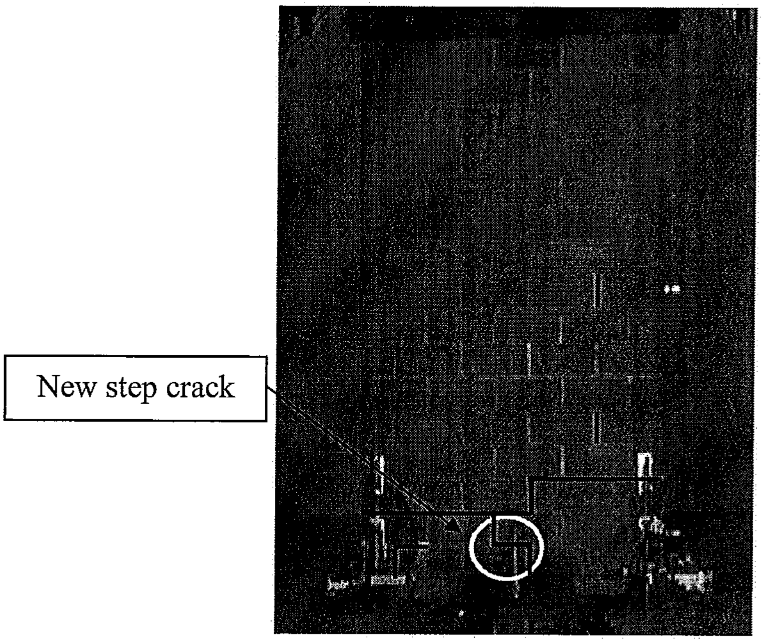

b) Final crack pattern after Run I

Figure 3.2: Crack propagation of Wall IA for selected runs

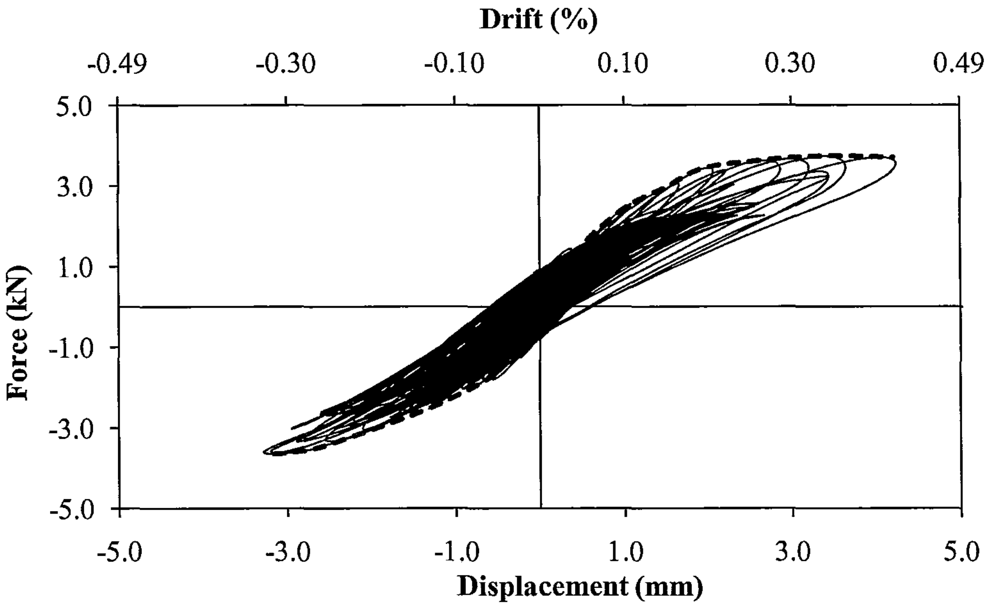

Figure 3.3: Wall IA hysteresis plot of all runs

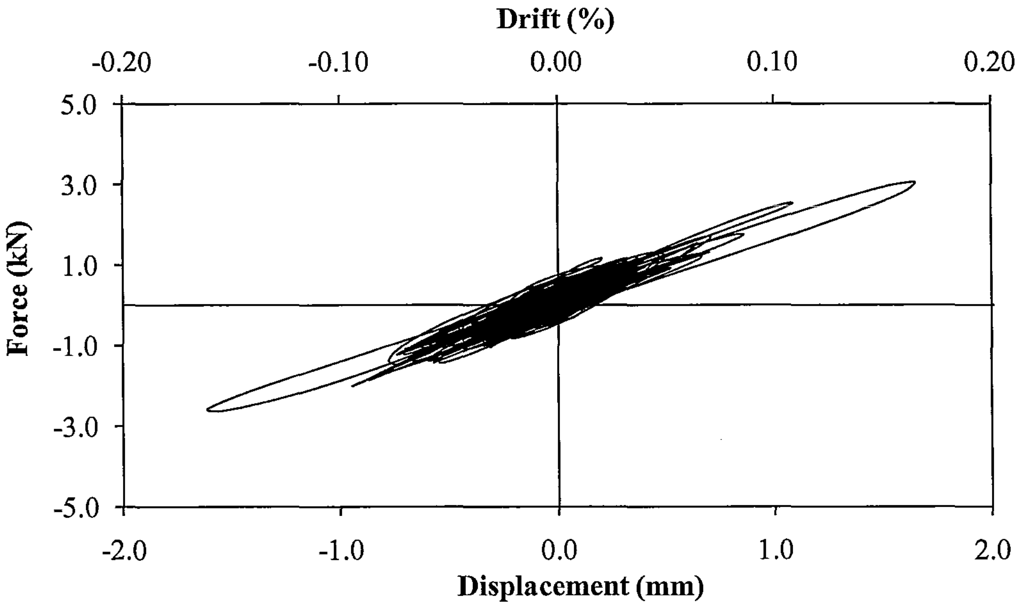

Figure 3.4: Wall IA Run E hysteresis showing energy dissipation and change of stiffness

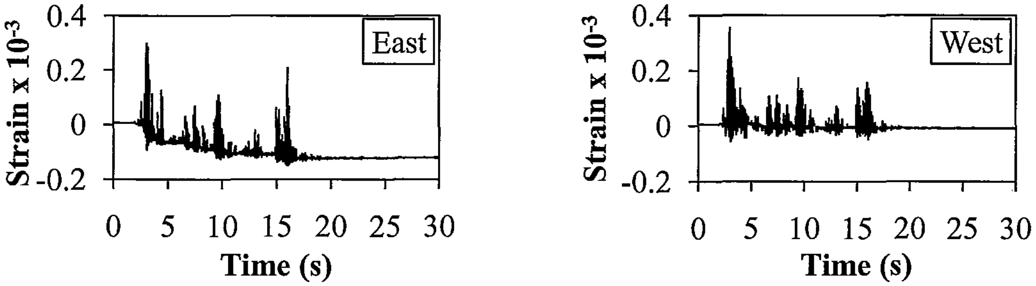

a) Run D time-history

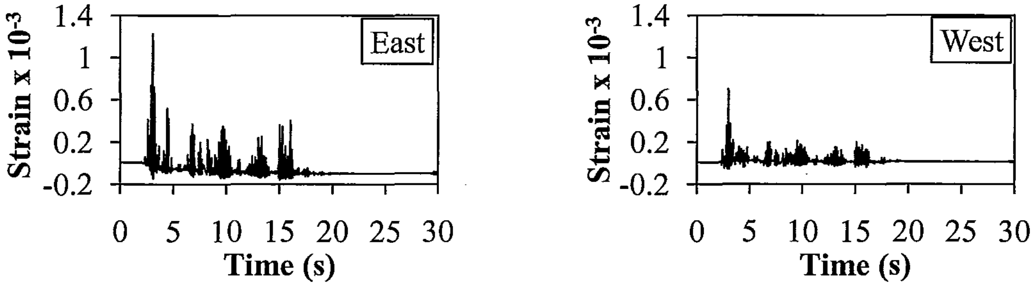

b) Run E time-history

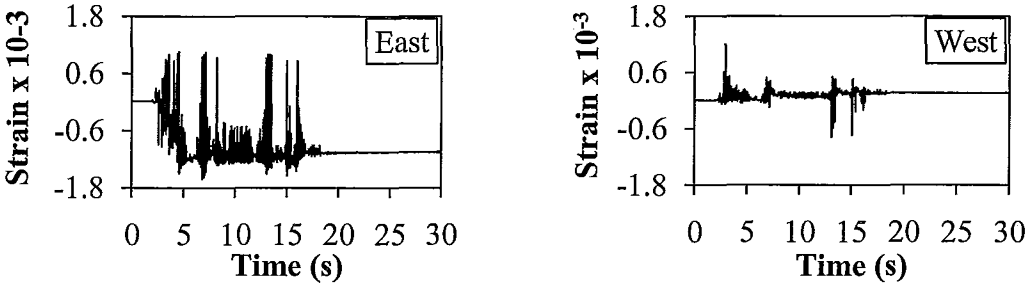

c) Run G time-history

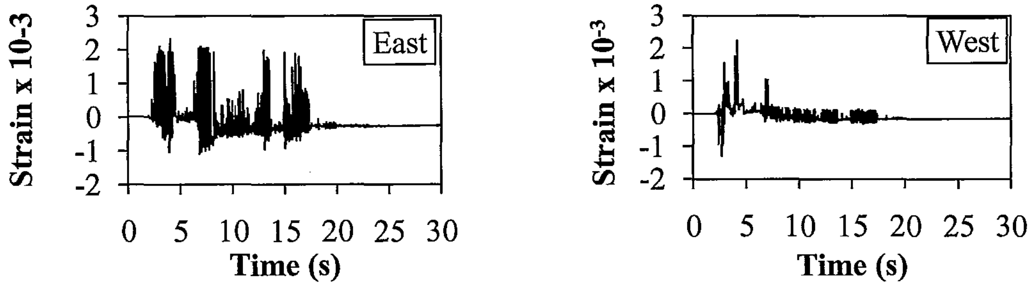

d) Run H time-history

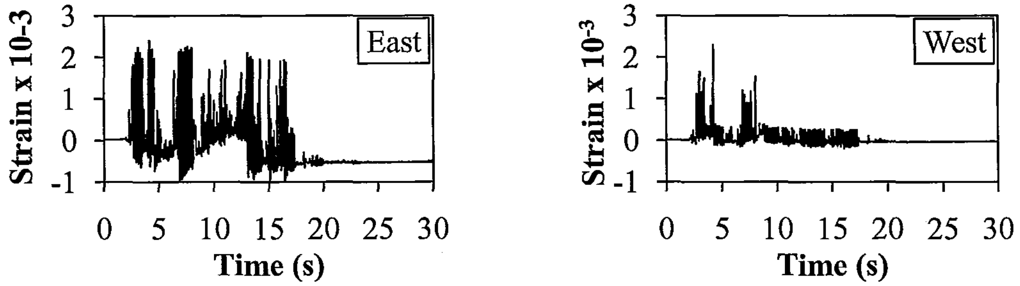

e) Run I time-history

Figure 3.5: Strain time-history of Wall IA vertical reinforcement for selected runs

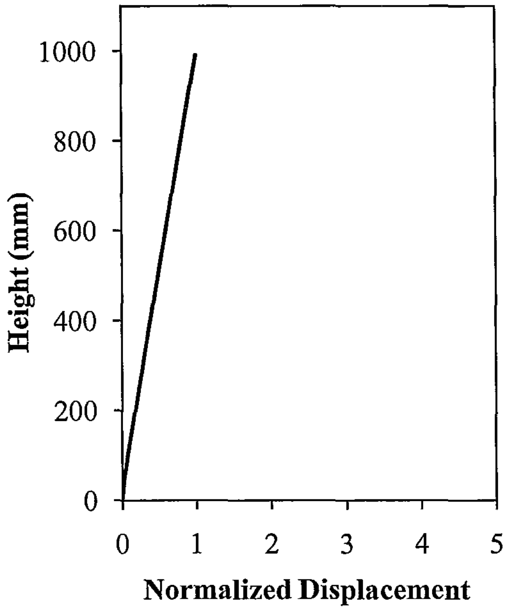

Figure 3.6: Mode shape of Wall IA at peak response during Run I

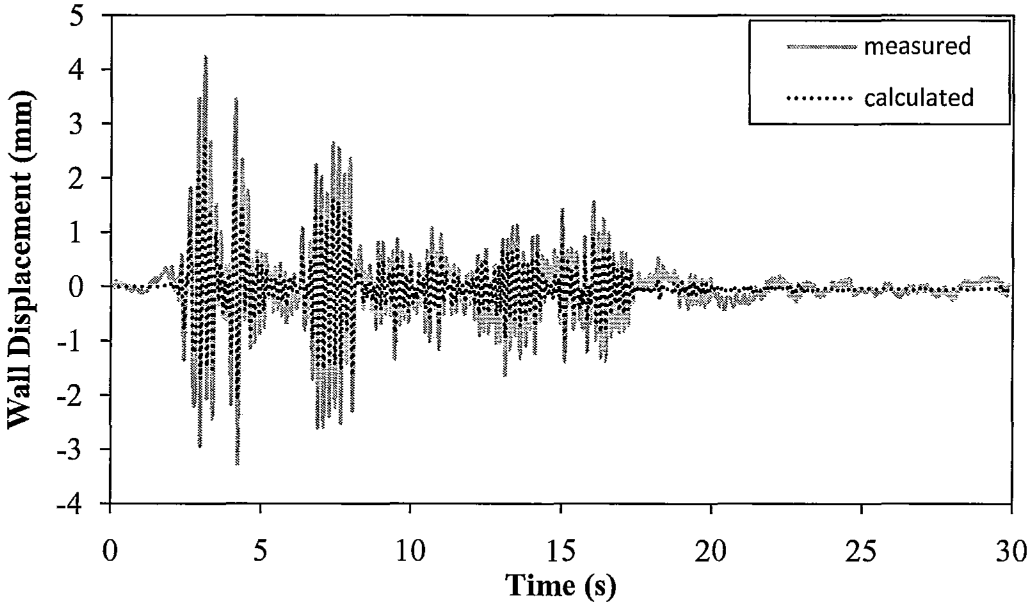

Figure 3.7: Time-history comparison between measured and calculated displacement due to the rocking of Wall IA

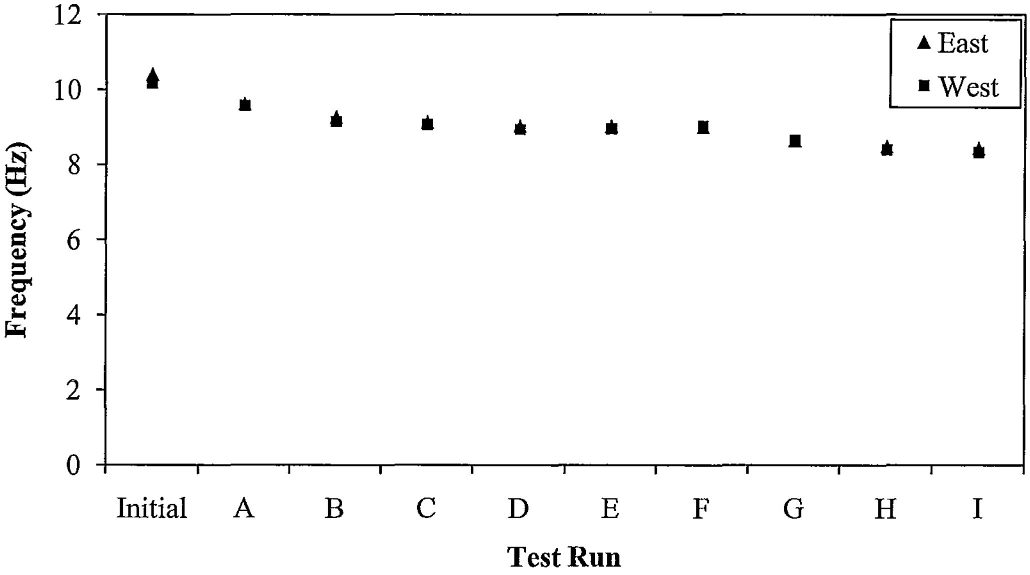

Figure 3.8: Hammer tap test frequency of Wall IA

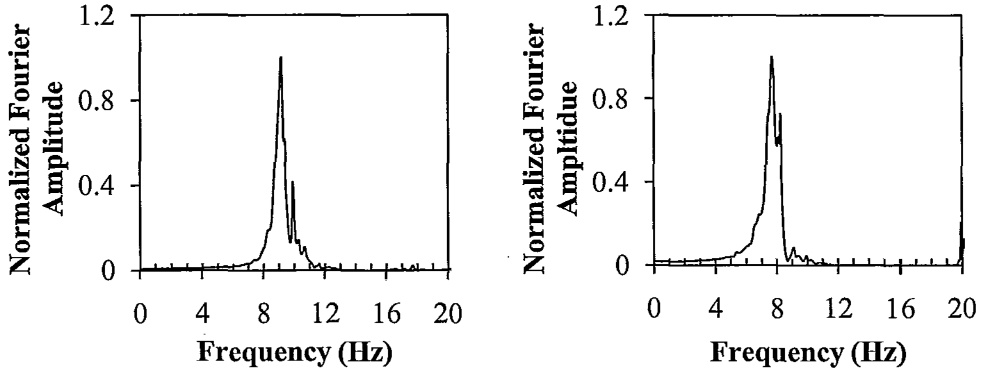

a) Run A

b) Run D

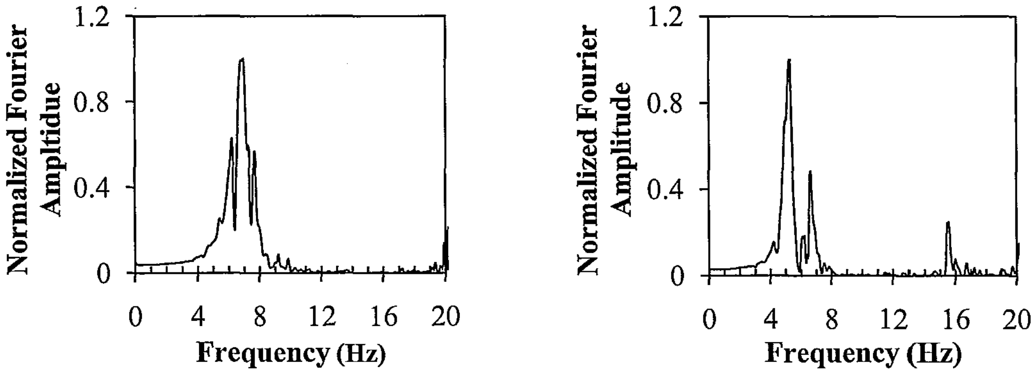

c) Run F

d) Run I

Figure 3.9: Frequency of Wall IA during several runs calculated by the FFT

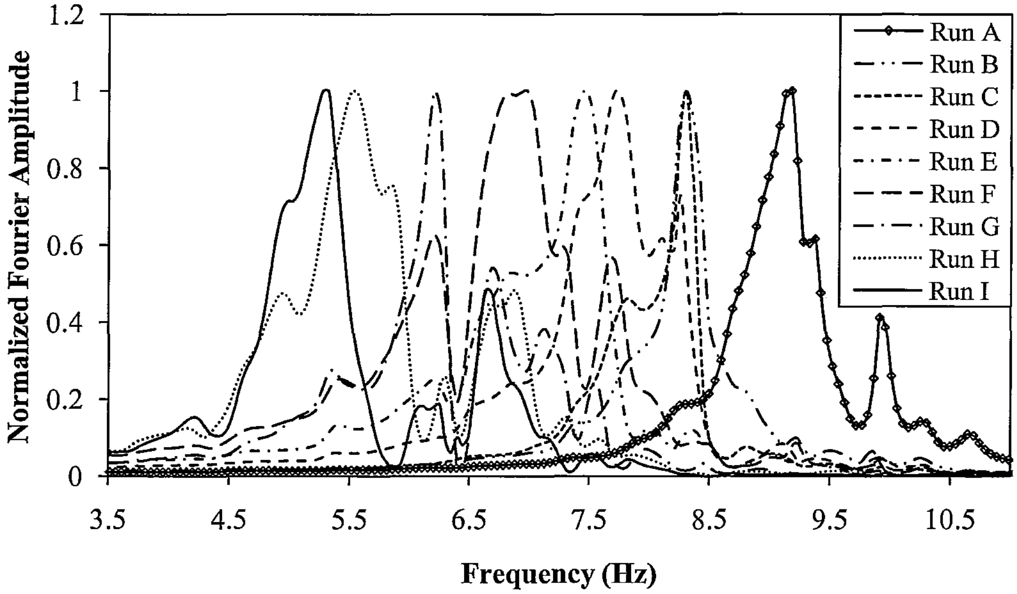

Figure 3.10: Frequency of Wall IA with all runs superimposed on the same graph calculated by the FFT

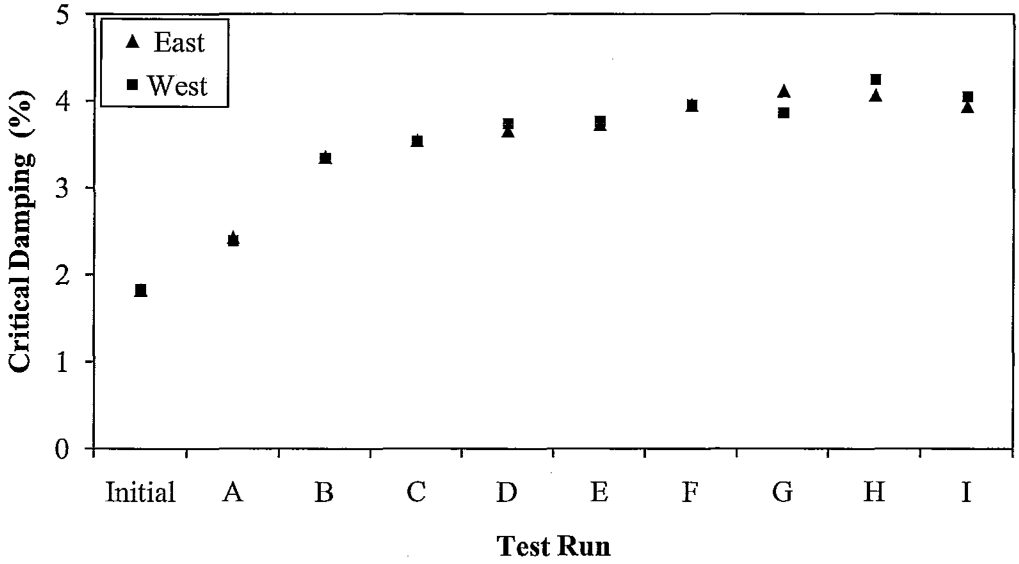

Figure 3.11: Critical damping of Wall IA runs calculated from the hammer tap test

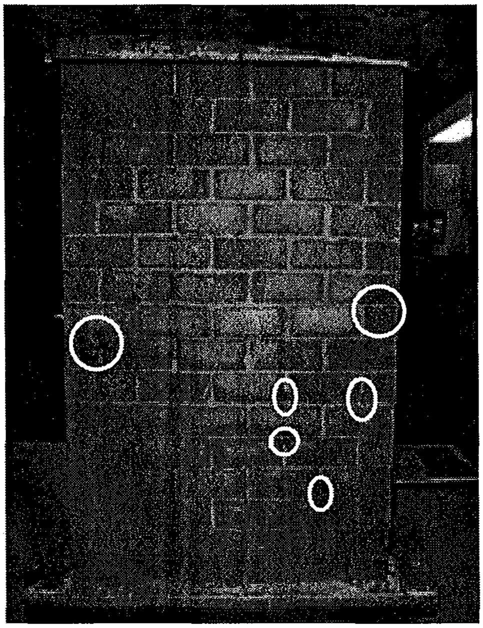

Figure 3.12: Location of mortar chips on the South face of Wall IB

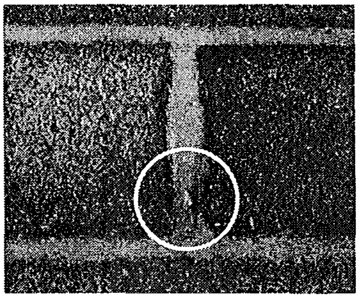

Figure 3.13: Close-up of a mortar chip

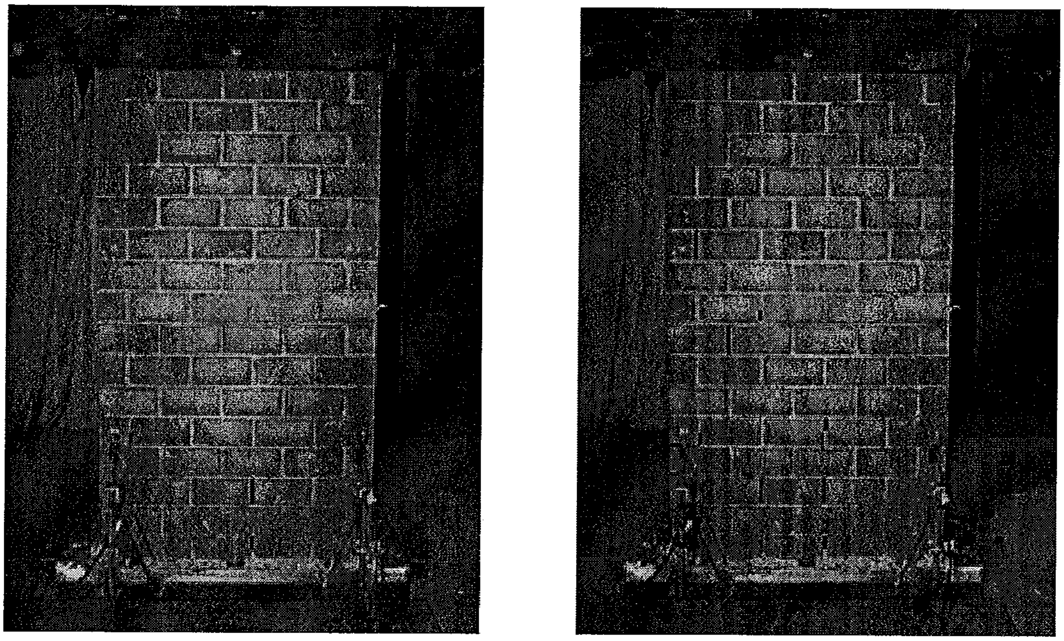

a) Run B

b) Run D

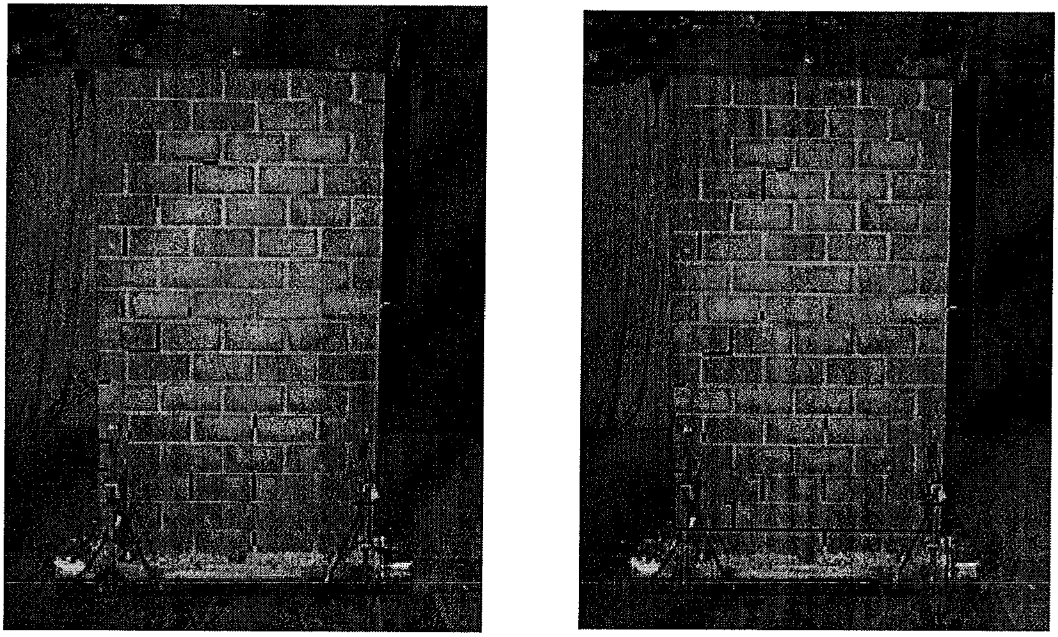

c) Run F

d) Run I

Figure 3.14: Crack propagation of Wall IB for selected runs

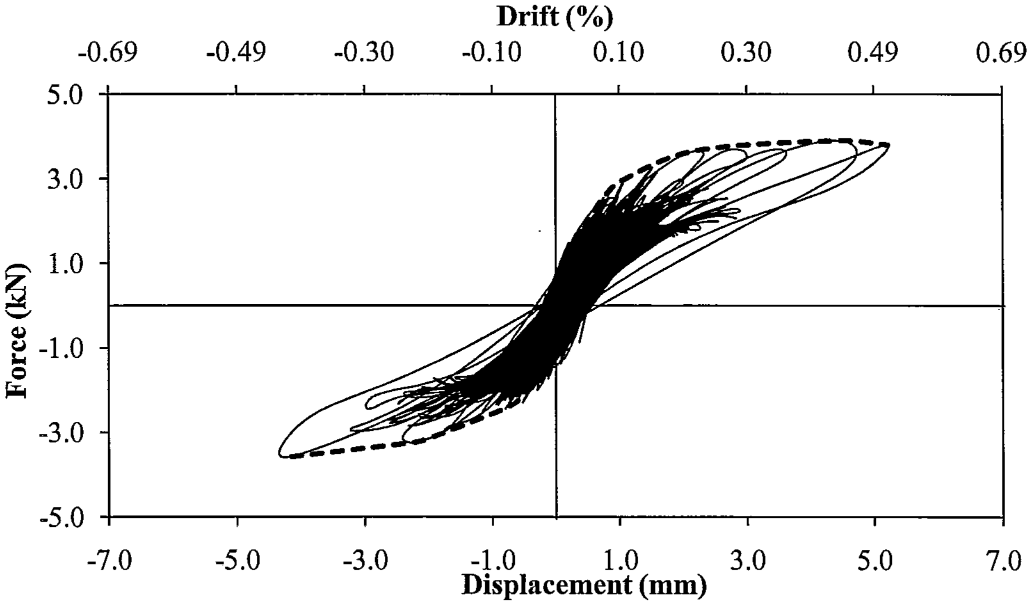

Figure 3.15: Wall IB hysteresis plot of all runs

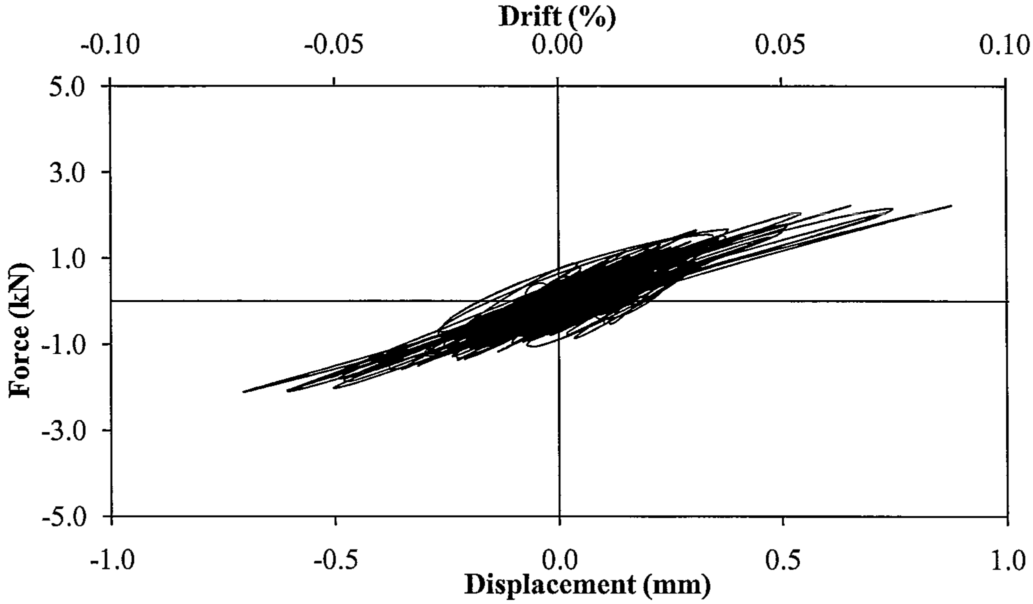

Figure 3.16: Wall IB Run D hysteresis showing change of stiffness

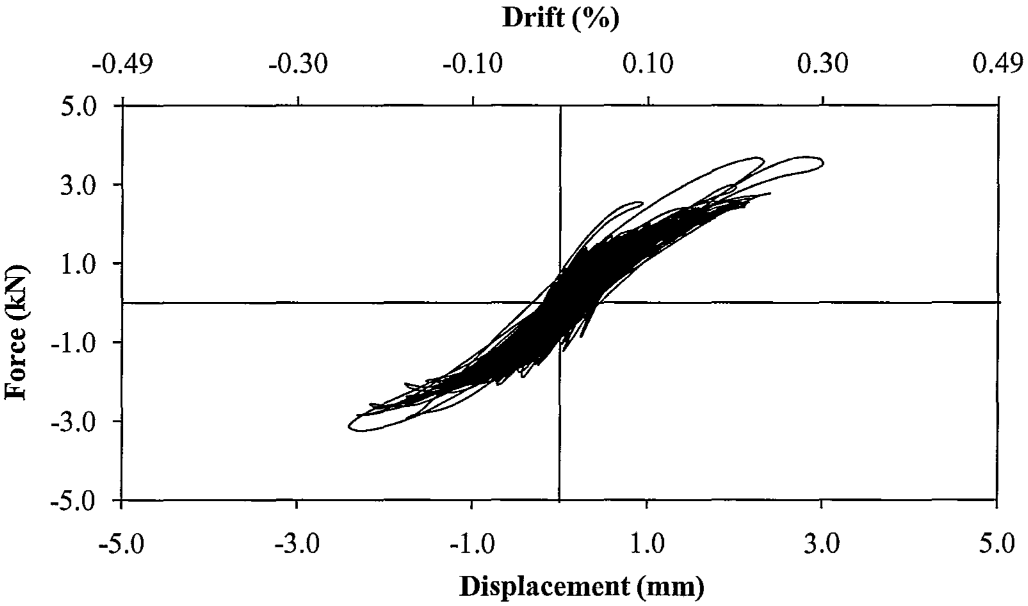

Figure 3.17: Wall IB Run H hysteresis showing energy dissipation

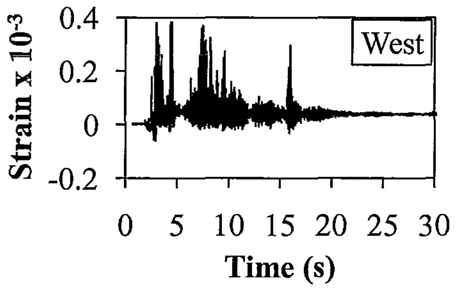

a) Run G time-history

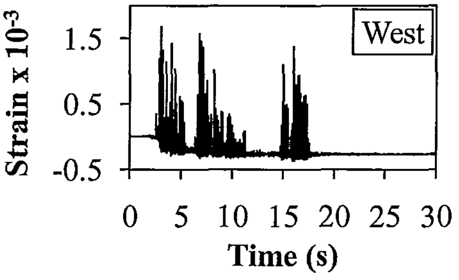

b) Run H time-history

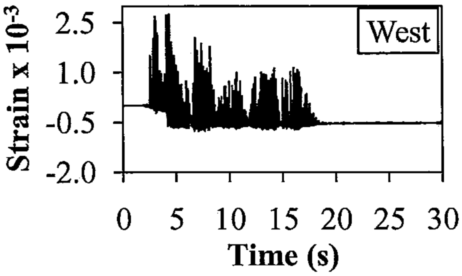

c) Run I time-history

Figure 3.18: Strain time-history of Wall IB vertical reinforcement for selected runs

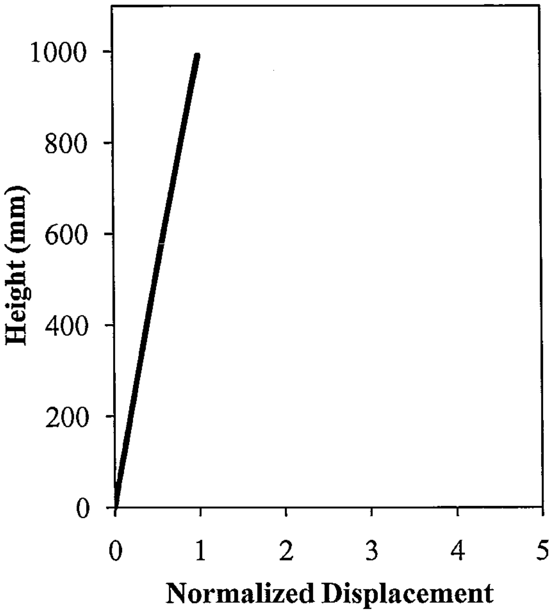

Figure 3.19: Mode shape of Wall IB at peak response during Run I

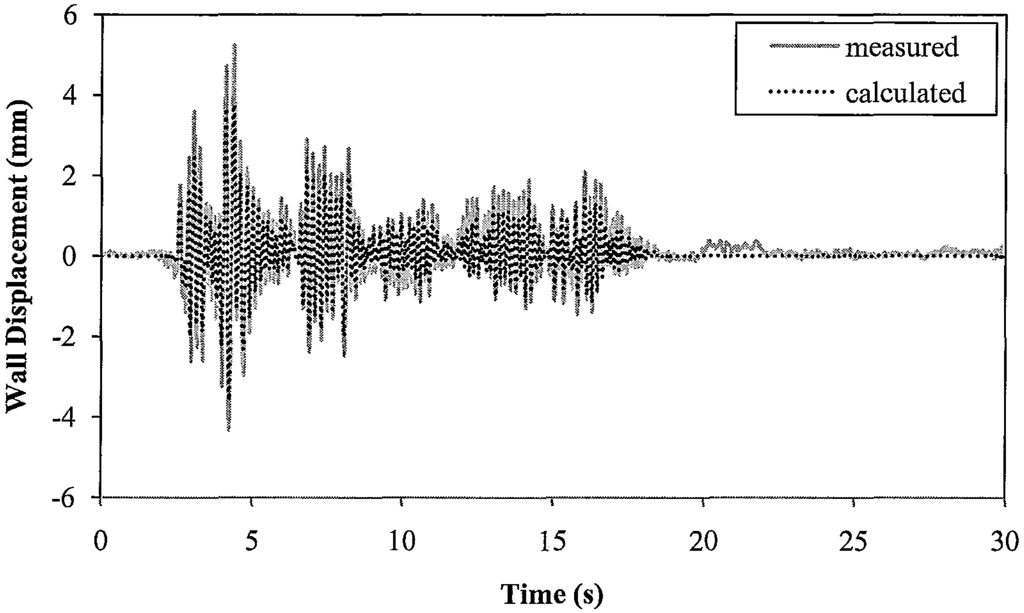

Figure 3.20: Time-history comparison between measured and calculated displacements due to the rocking of Wall IB

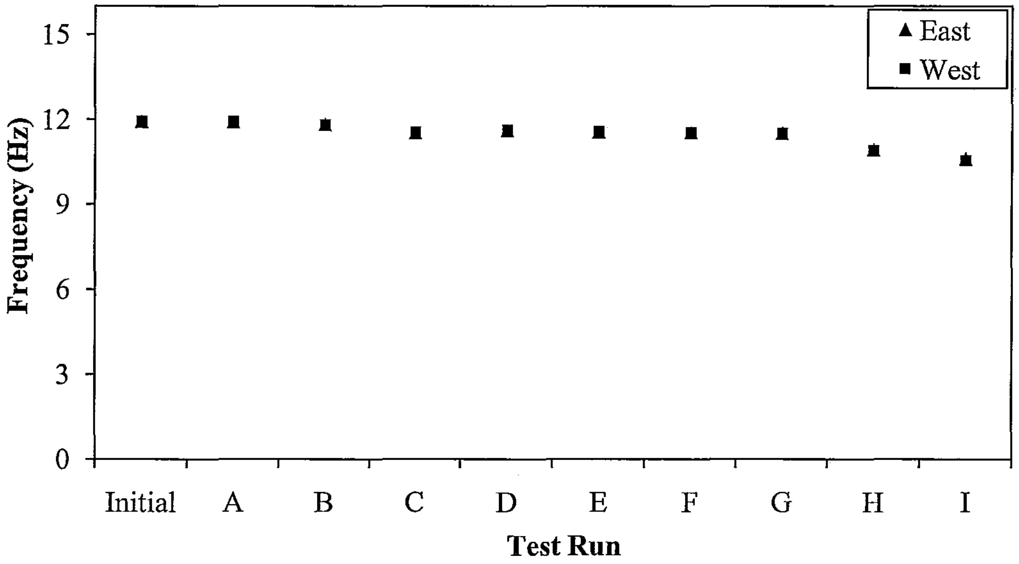

Figure 3.21: Hammer tap test frequency of Wall IB

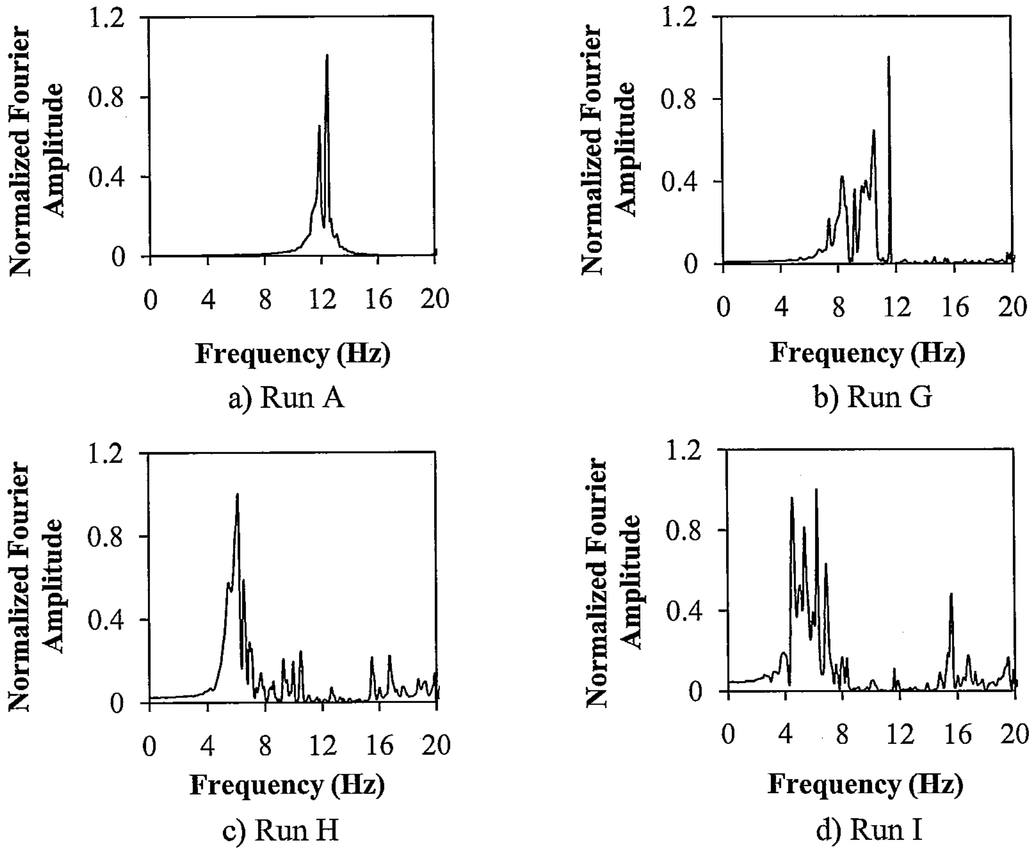

Figure 3.22: Frequency of Wall IB during several runs calculated by the FFT

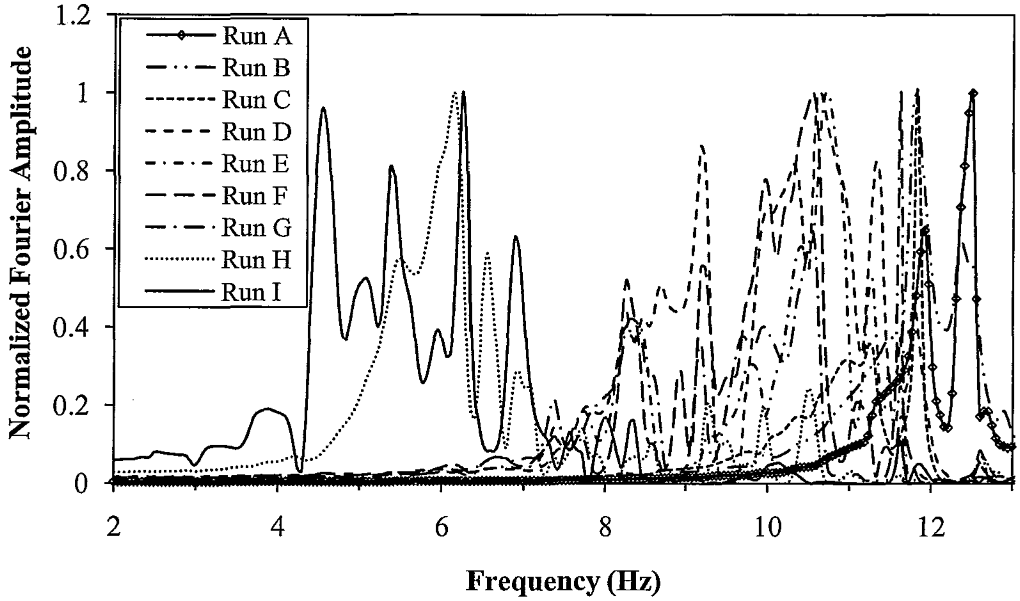

Figure 3.23: Frequency of Wall IB with all runs superimposed on the same graph calculated by the FFT

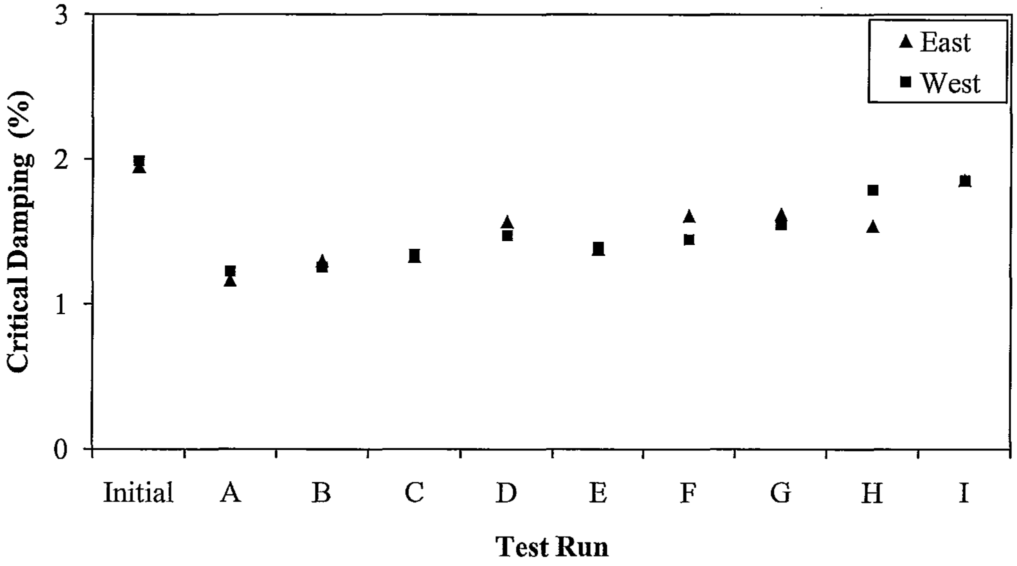

Figure 3.24: Critical damping of Wall IB runs calculated from the hammer tap test

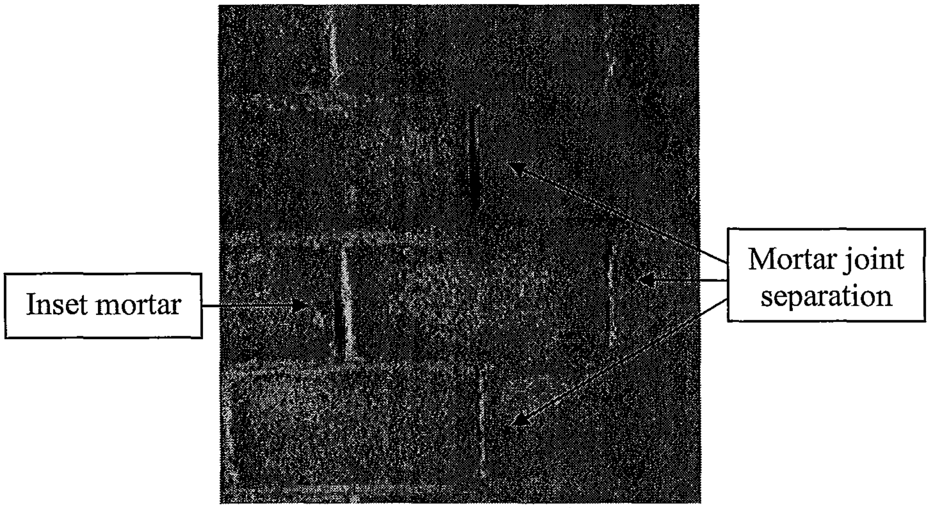

Figure 3.25: Inset and separated mortar joints on the South face

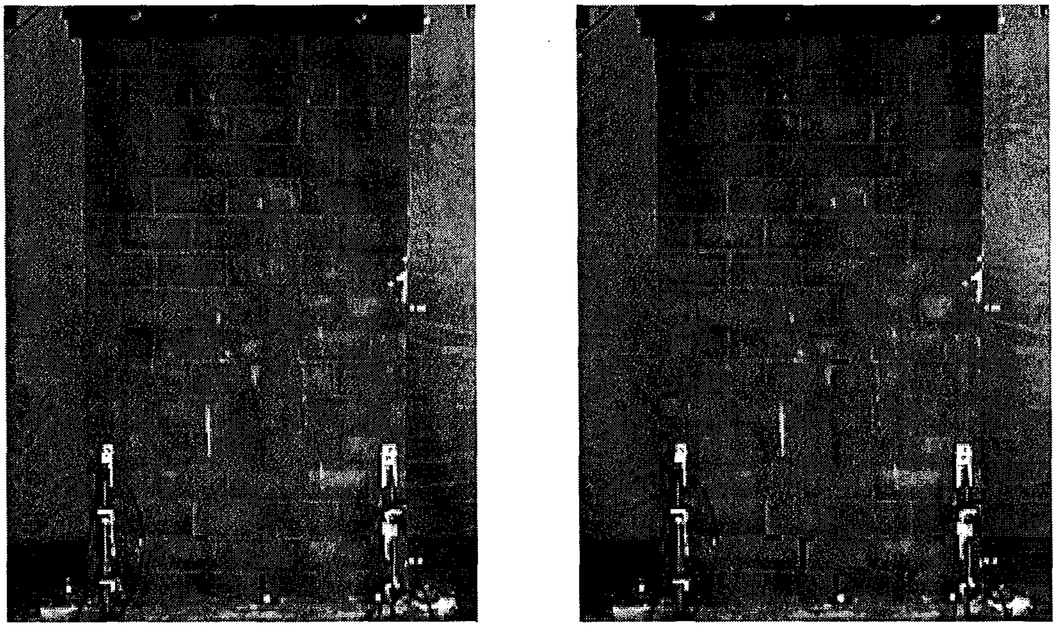
a) Run G

b) Run H

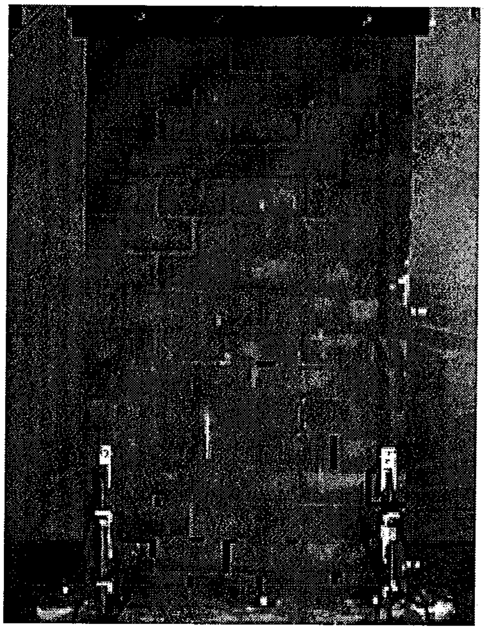

c) Run I

Figure 3.26: Crack propagation of Wall IIA for selected runs

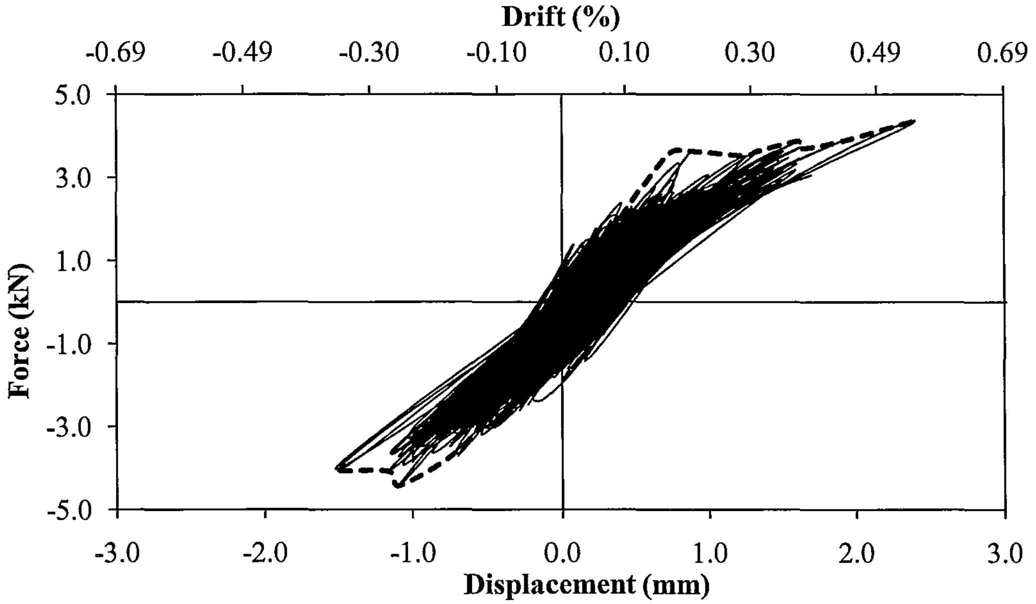

Figure 3.27: Wall IIA hysteresis plot of all runs

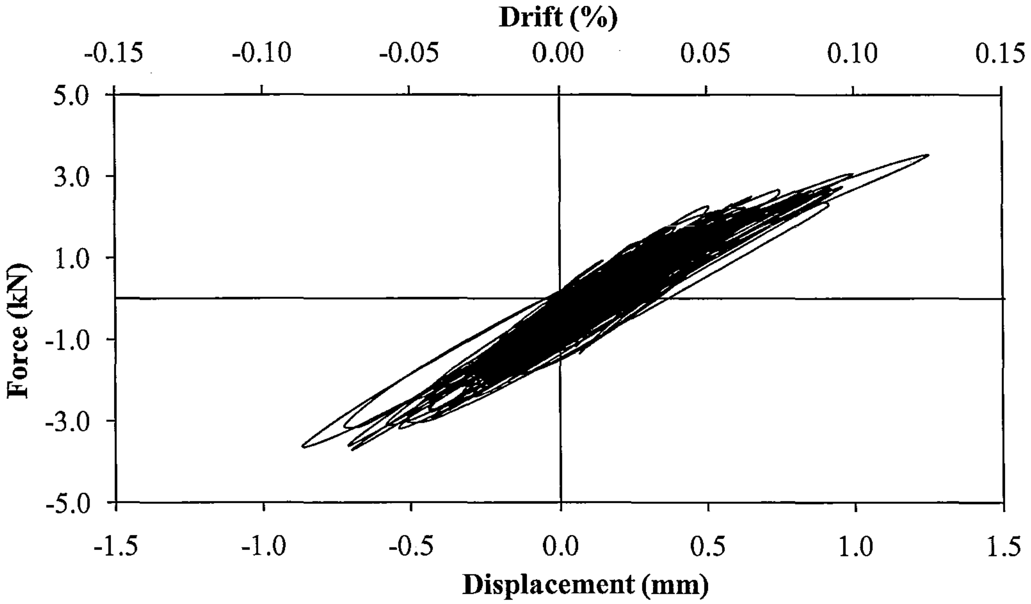

Figure 3.28: Wall IIA Run F hysteresis showing change of stiffness

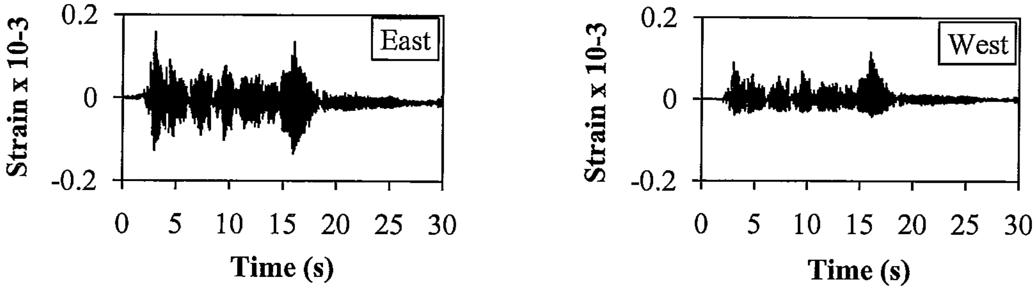

Figure 3.29: Strain time-history of Wall IIA vertical reinforcement for Run I

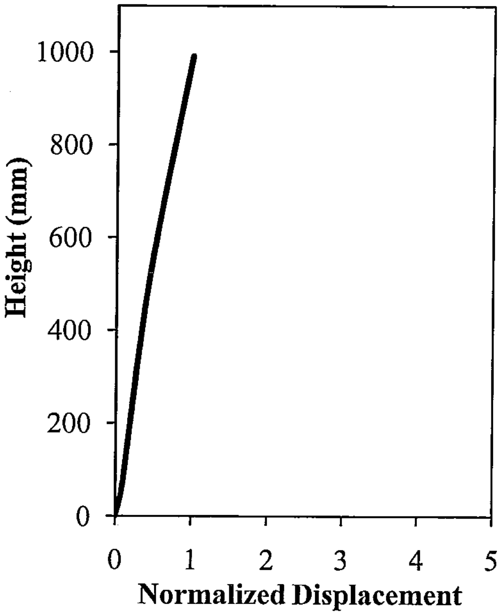

Figure 3.30: Mode shape of Wall IIA at peak response during Run I

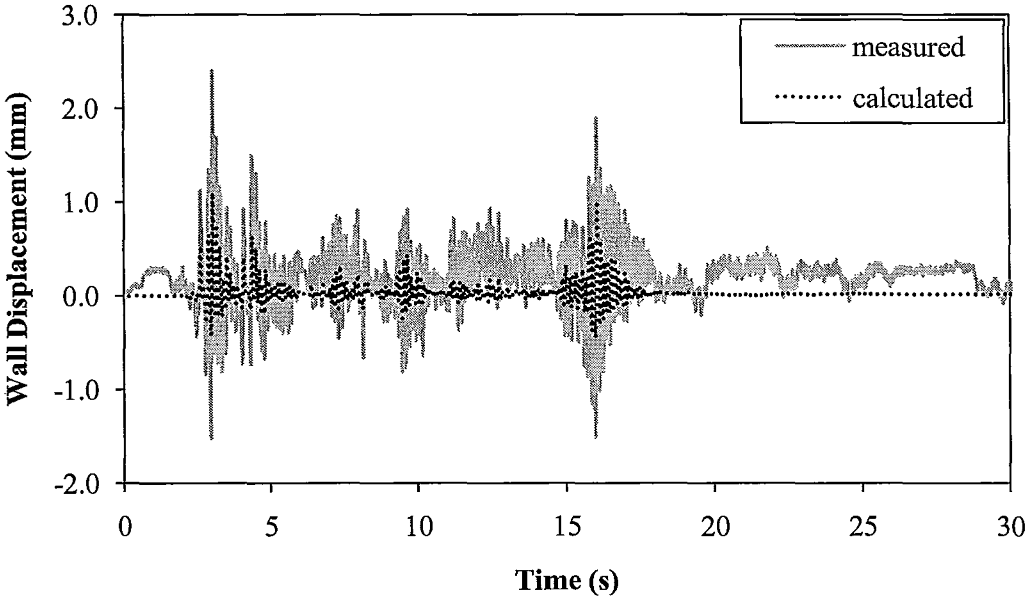

Figure 3.31: Time-history comparison between measured and calculated displacements due to the rocking of Wall IIA

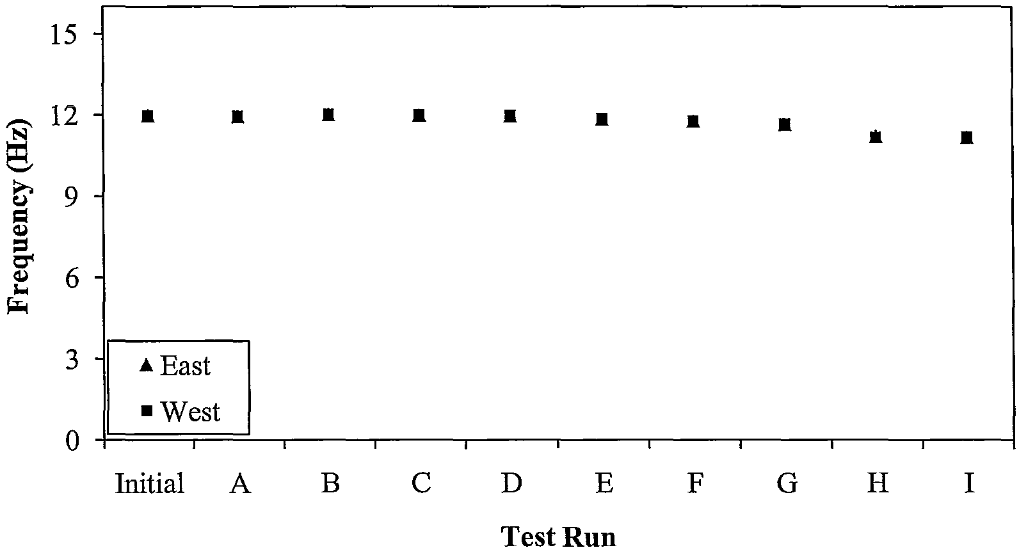

Figure 3.32: Hammer tap test frequency of Wall IIA

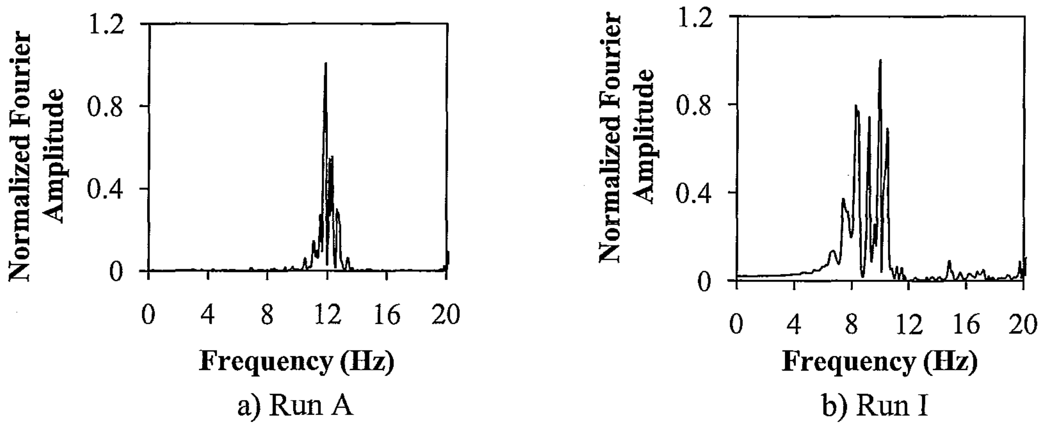

a) Run A

b) Run I

Figure 3.33: Frequency of Wall IIA during several runs calculated by the FFT

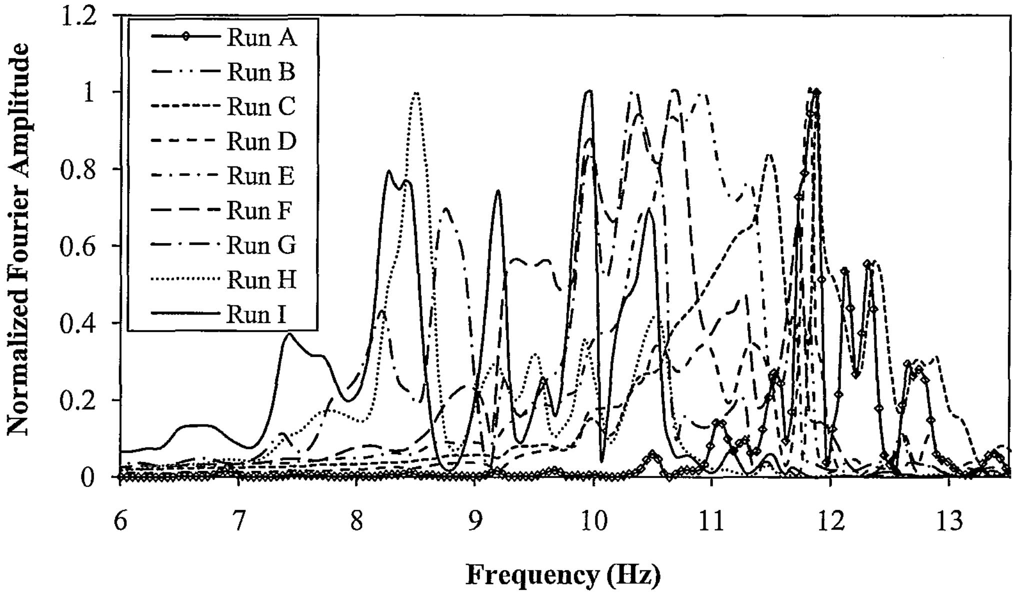

Figure 3.34: Frequency of Wall IIA with all runs superimposed on the same graph calculated by the FFT

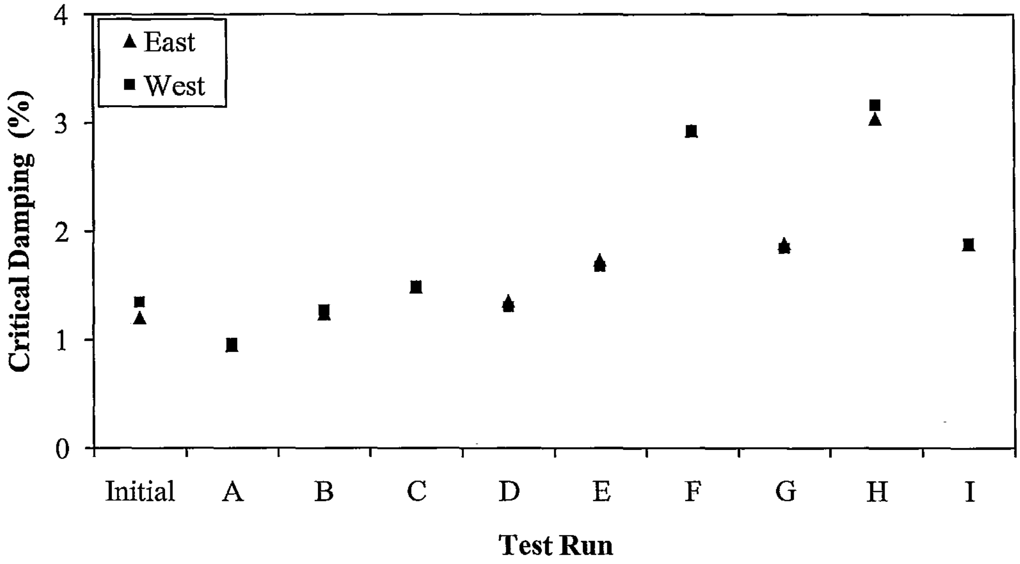

Figure 3.35: Critical damping of Wall IIA runs calculated from the hammer tap test

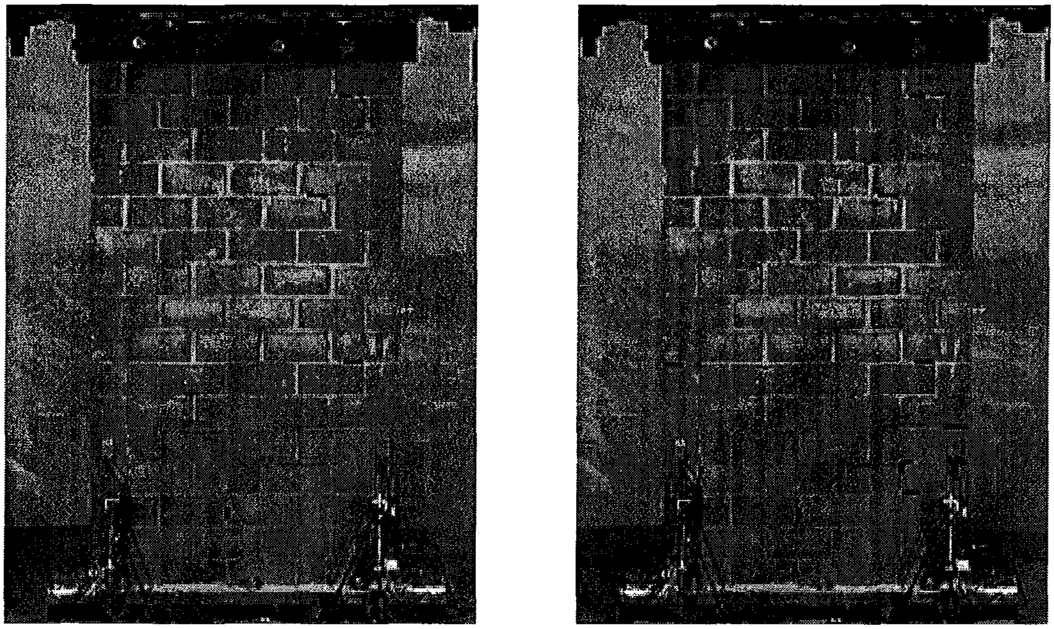

a) Initial b) Run E

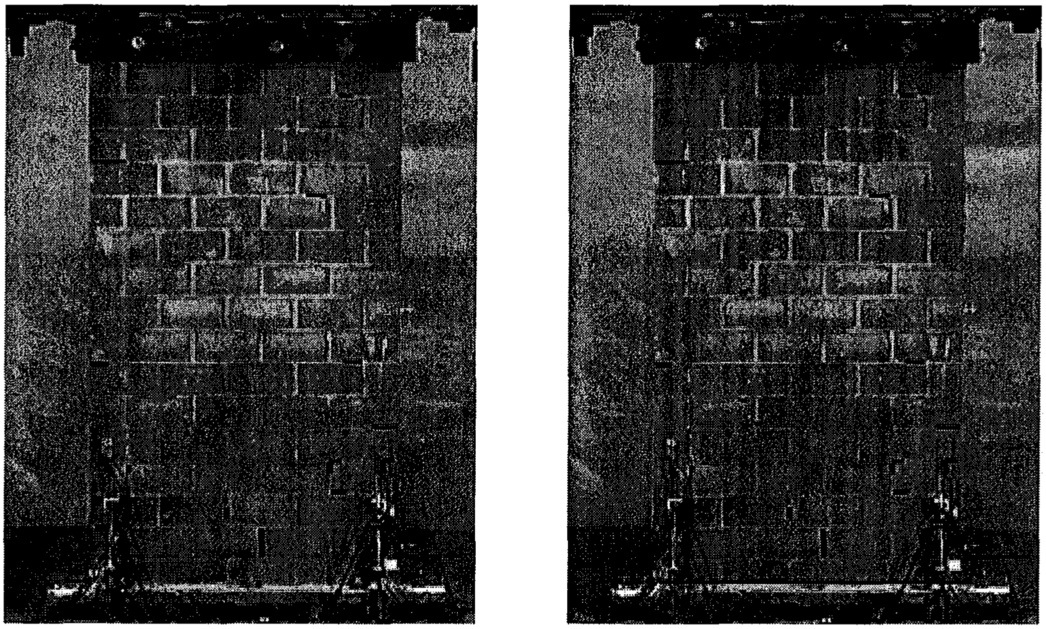

c) Run F d) Run I

Figure 3.36: Crack propagation of Wall IIB for selected ru

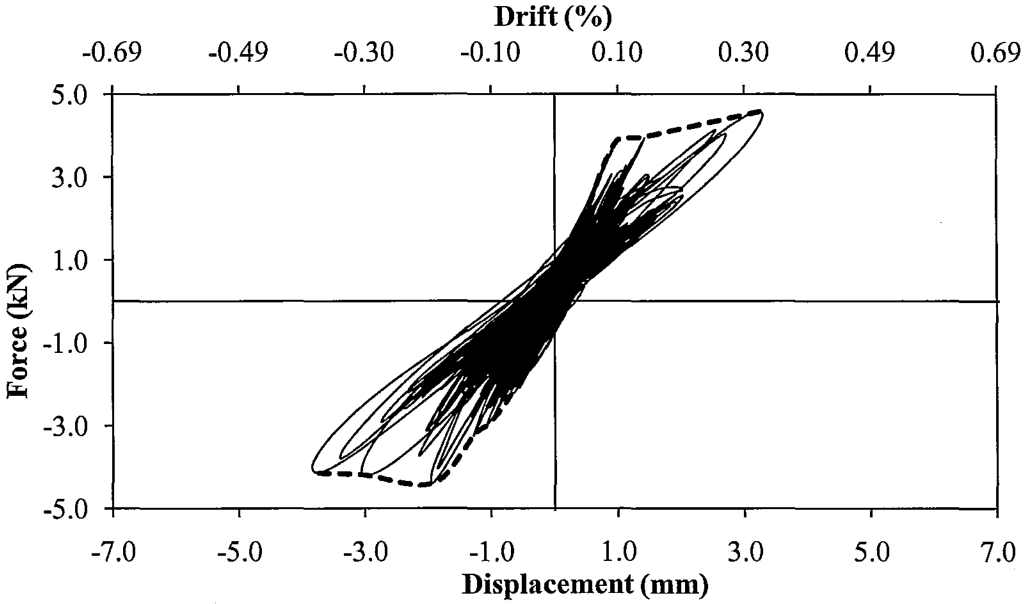

Figure 3.37: Wall IIB hysteresis plot of all runs

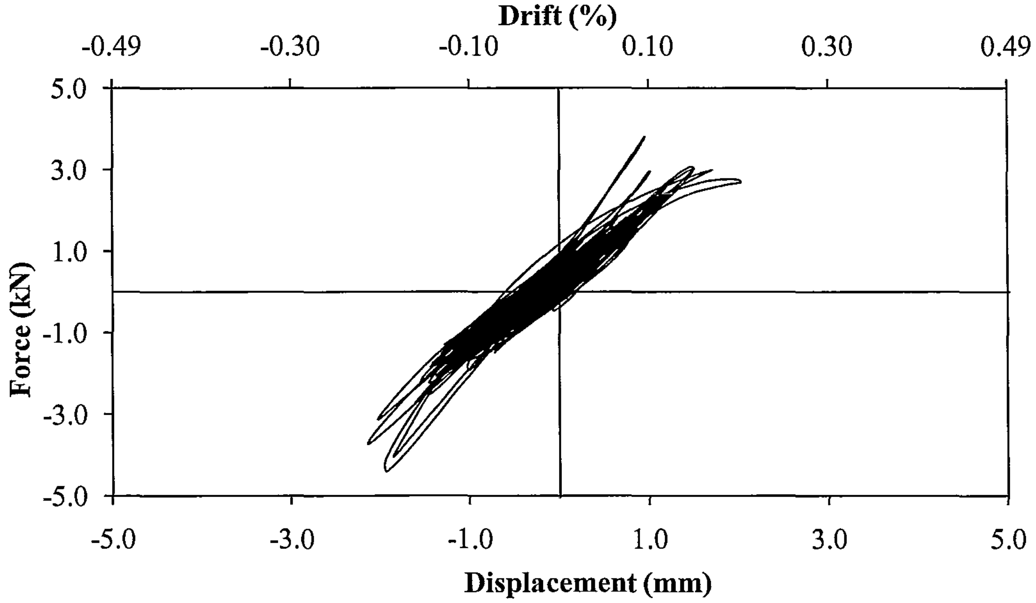

a) Run H

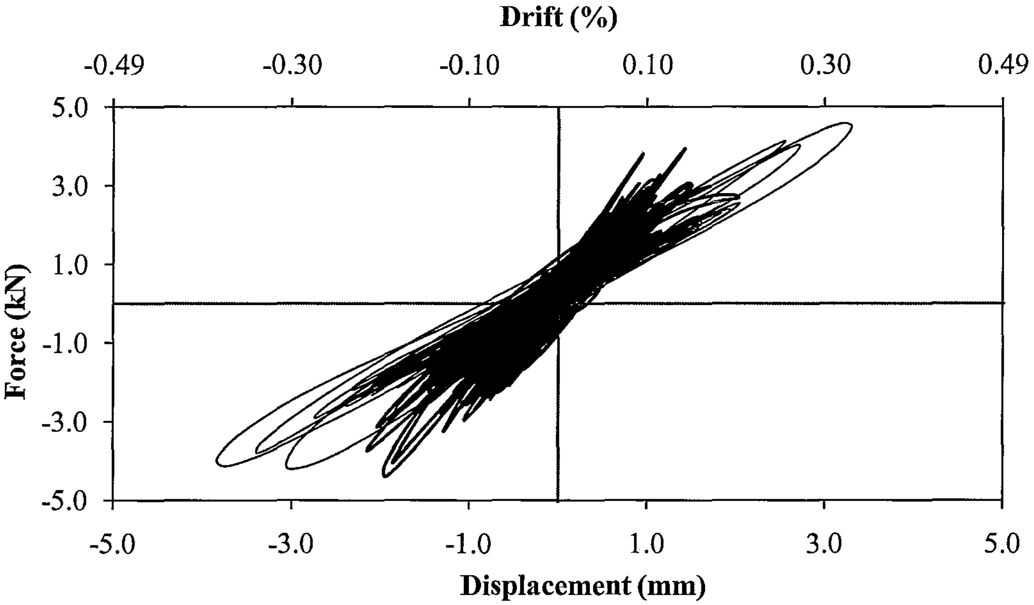

b) Run I

Figure 3.38: Wall IIB Run H and I showing change of stiffness and energy dissipation

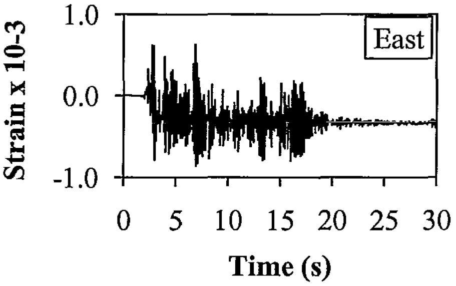

a) Run H time-history

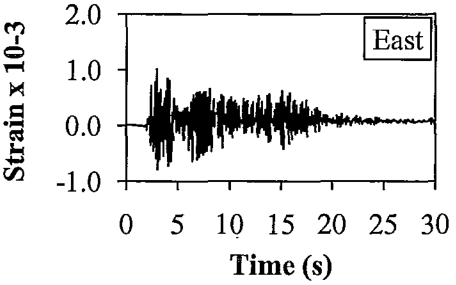

b) Run I time-history

Figure 3.39: Strain time-history of Wall IIB vertical reinforcement for selected runs

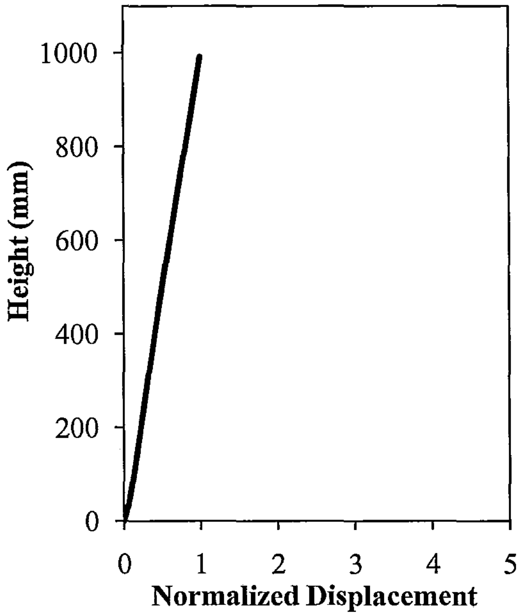

Figure 3.40: Mode shape of Wall IIB at peak response during Run I

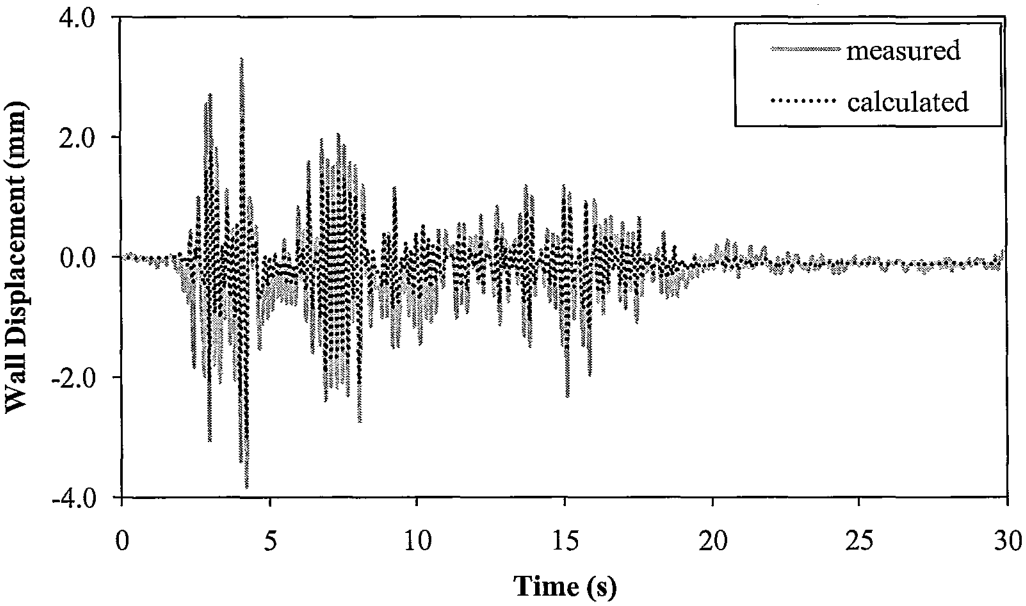

Figure 3.41: Time-history comparison between measured and calculated displacements due to the rocking of Wall IIB

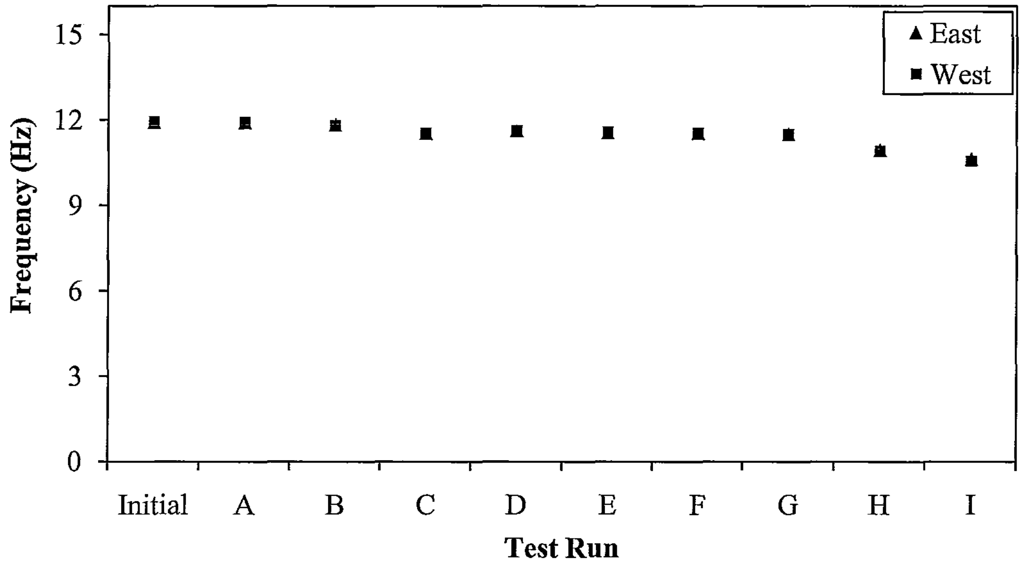

Figure 3.42: Hammer tap test frequency of Wall IIB

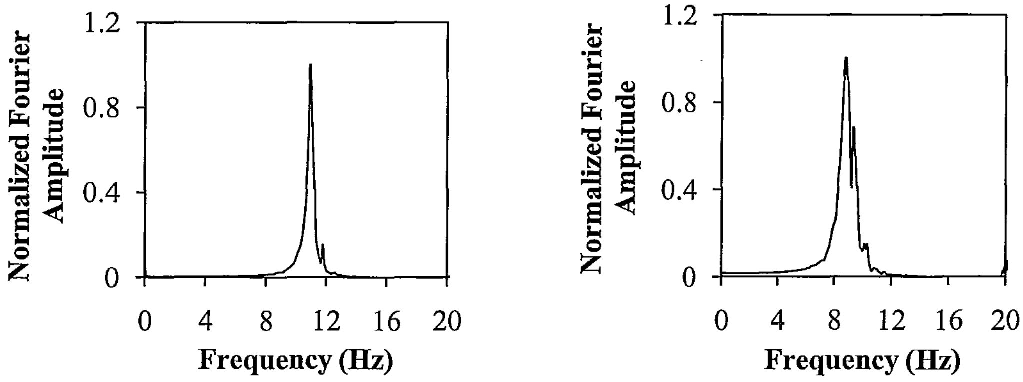

a) Run A

b) Run E

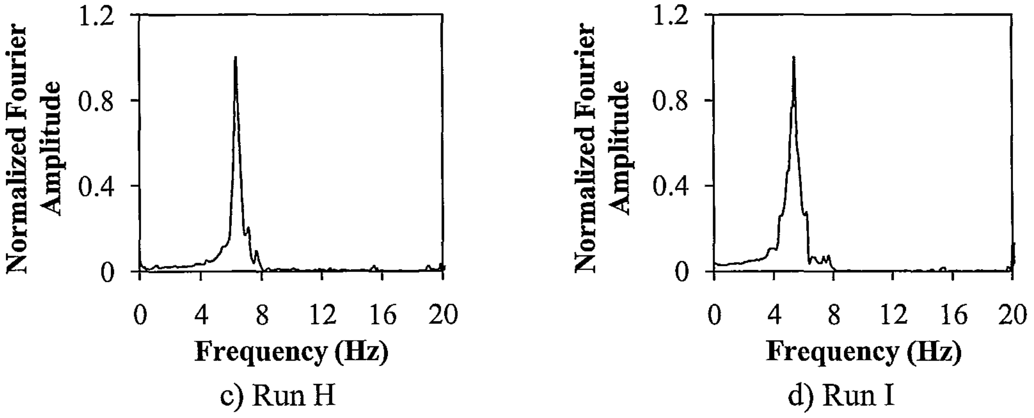

c) Run H

d) Run I

Figure 3.43: Frequency of Wall IIB during several runs calculated by the FFT

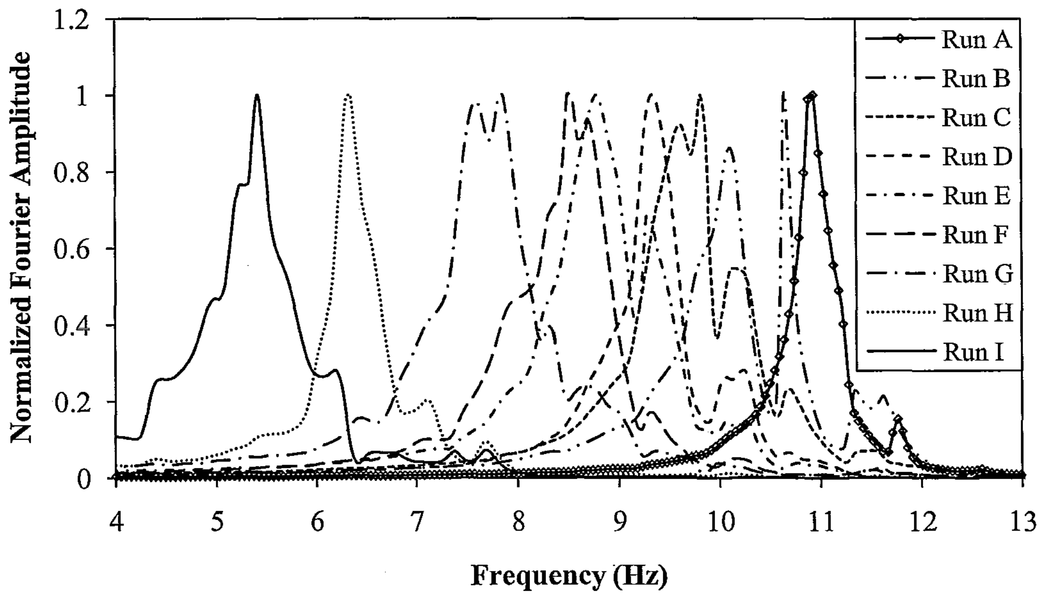

Figure 3.44: Frequency of Wall IIB with all runs superimposed on the same graph calculated by the FFT

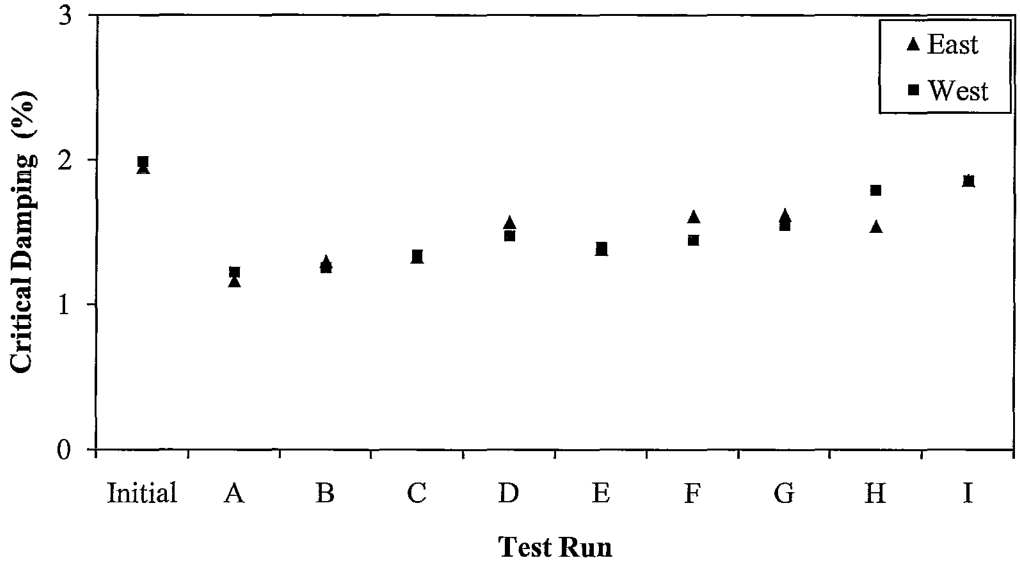

Figure 3.45: Critical damping of Wall IIB runs calculated from the hammer tap test

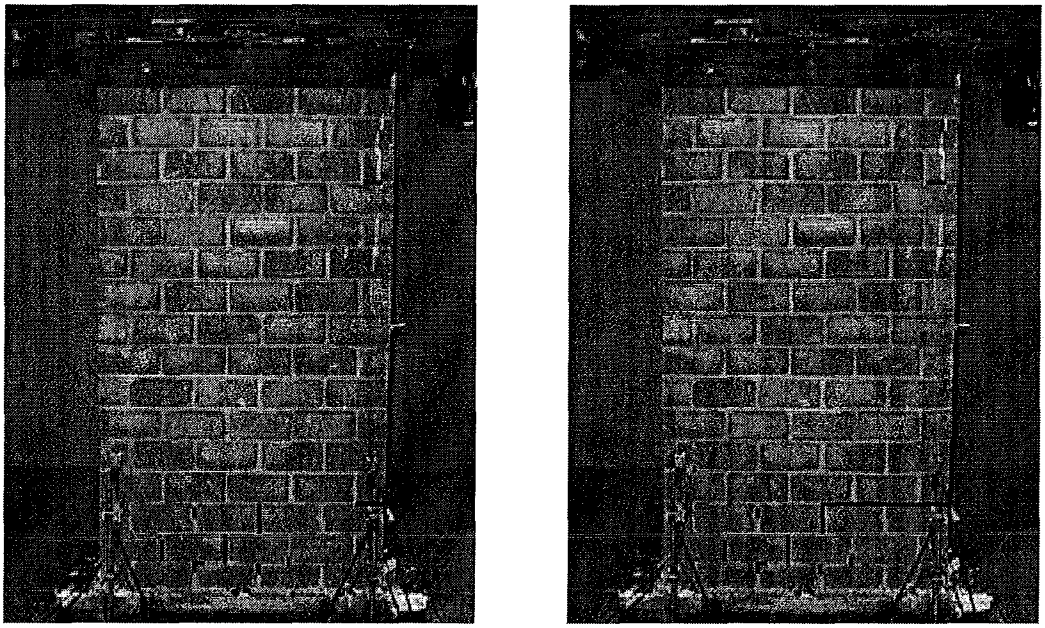

a) Initial

b) Run C

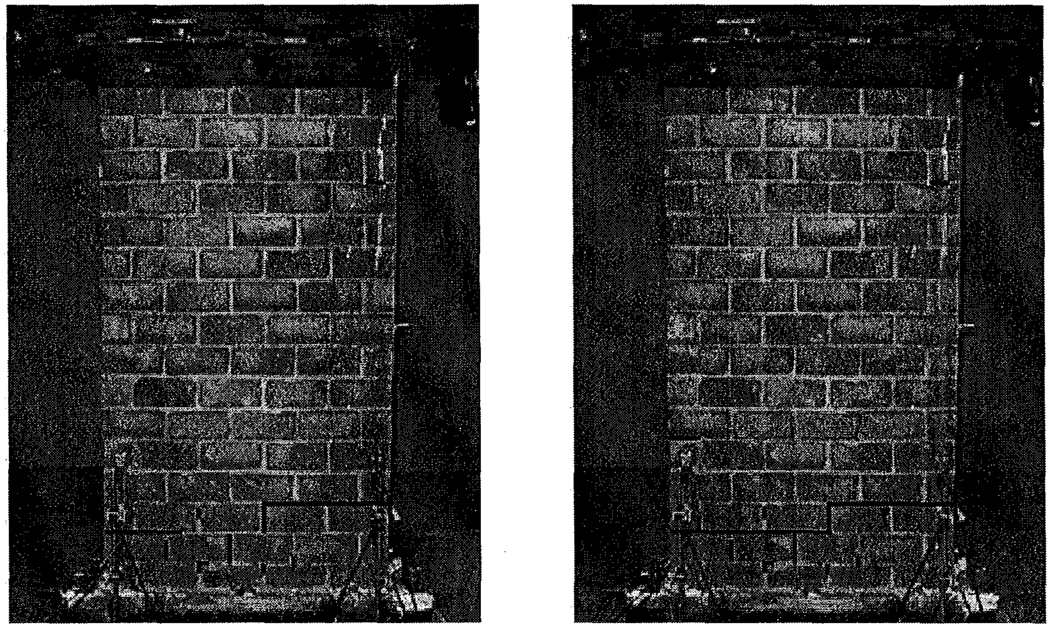

c) Run F d) Run H

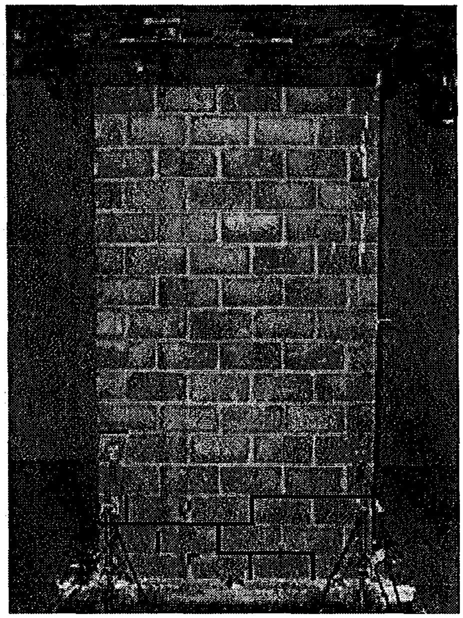

e) Run I

Figure 3.46: Crack propagation of Wall IIIA for selected runs

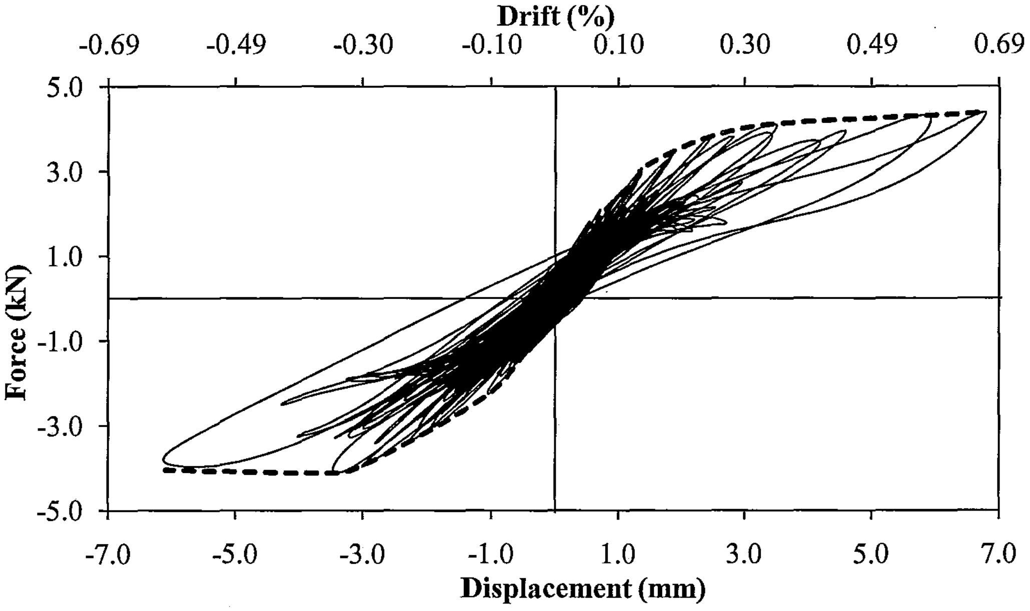

Figure 3.47: Wall IIIA hysteresis plot of all runs

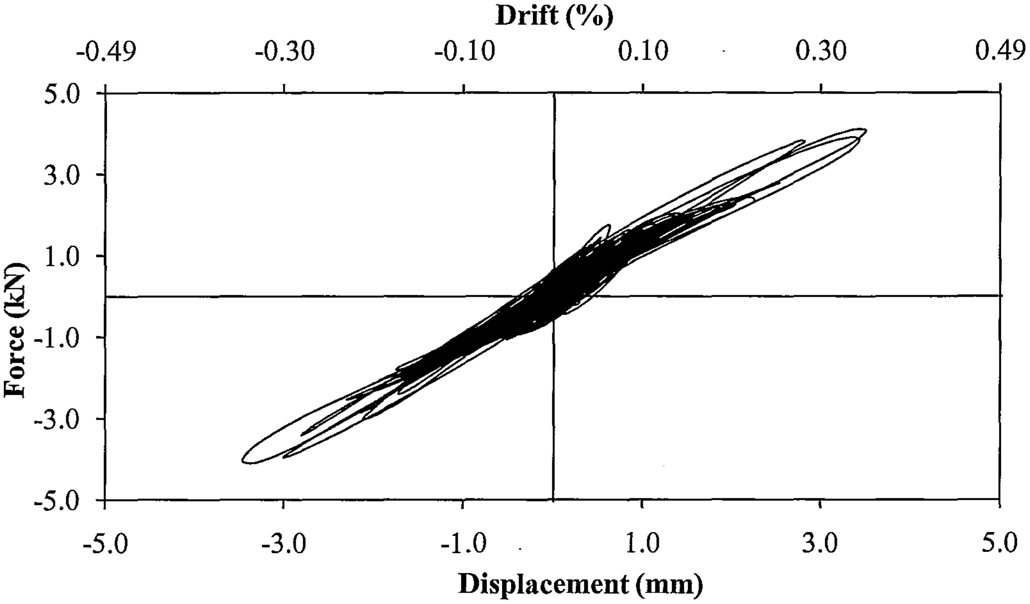

a) Run H

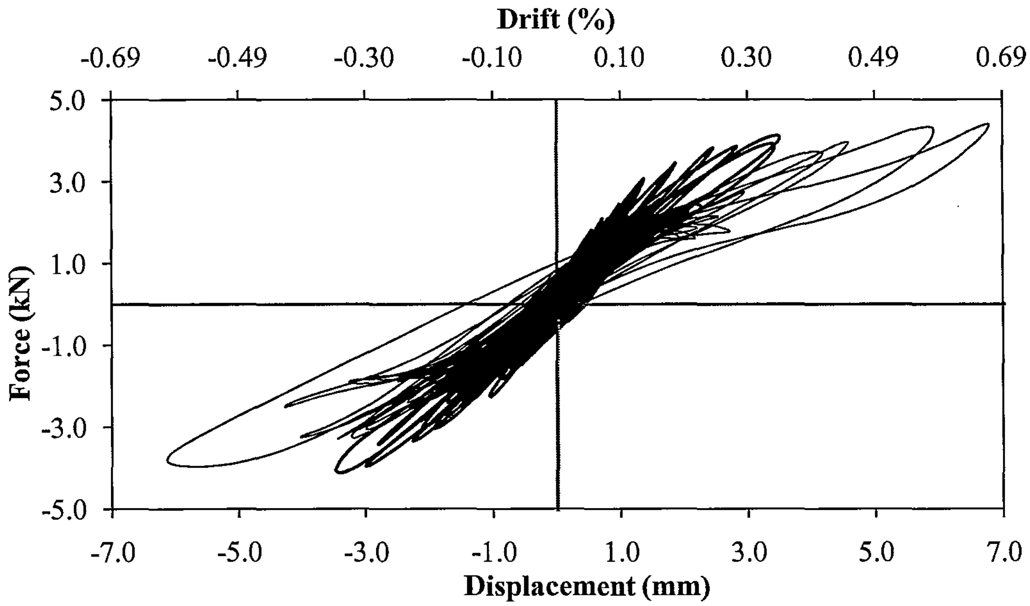

b) Run I

Figure 3.48: Wall IIIA Run H and I showing change of stiffness and energy dissipation

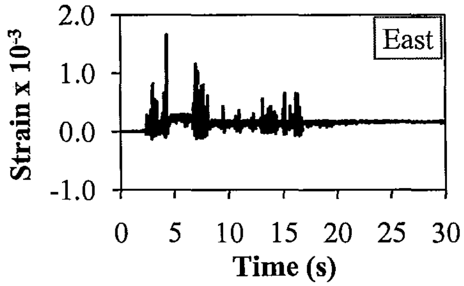

a) Run H time-history

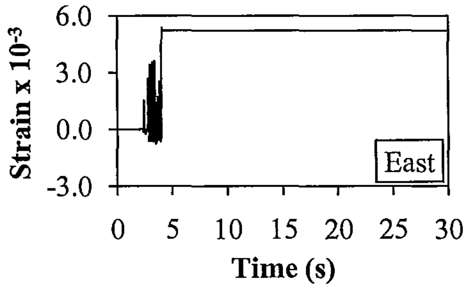

b) Run I time-history

Figure 3.49: Strain time-history of Wall IIIA vertical reinforcement for selected runs

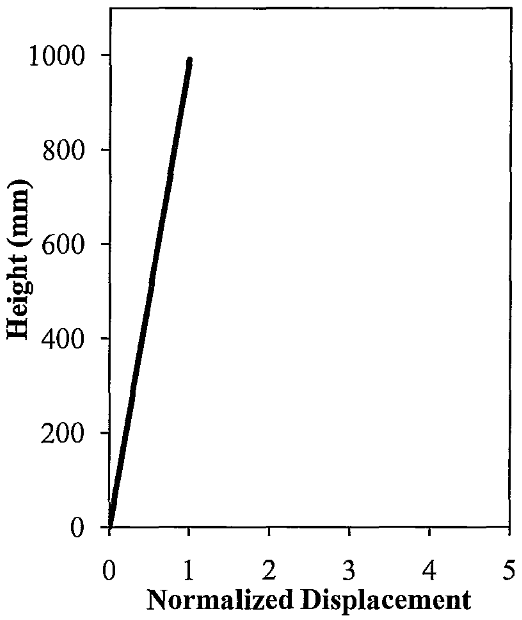

Figure 3.50: Mode shape of Wall IIIA at peak response during Run I

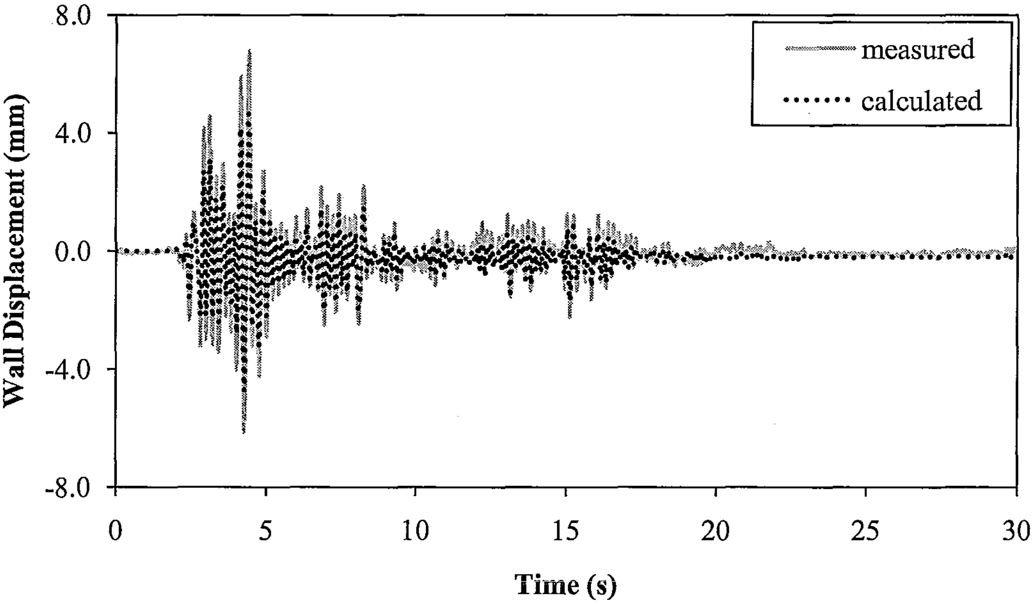

Figure 3.51: Time-history comparison between measured and calculated displacements due to the rocking of Wall IIIA

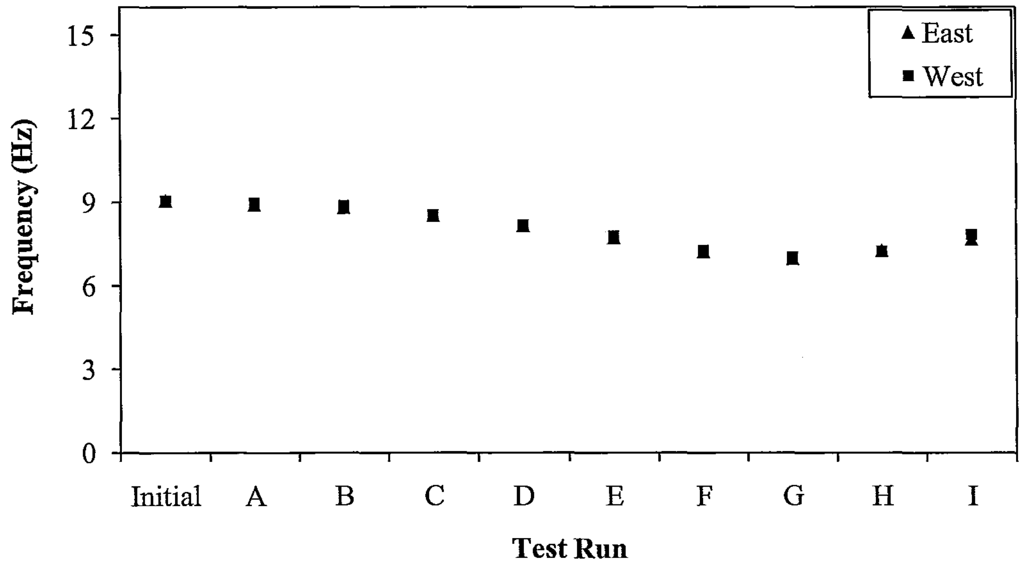

Figure 3.52: Hammer tap test frequency of Wall IIIA

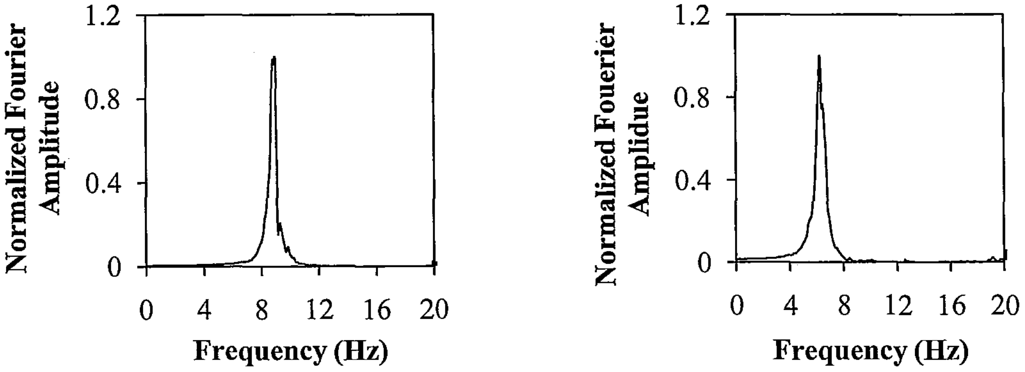

a) Run A

b) Run G

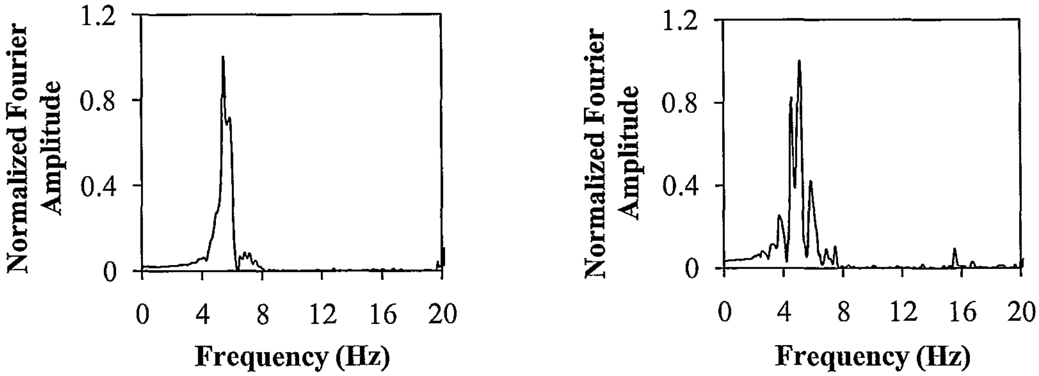

c) Run H

d) Run I

Figure 3.53: Frequency of Wall IIIA during several runs calculated by the FFT

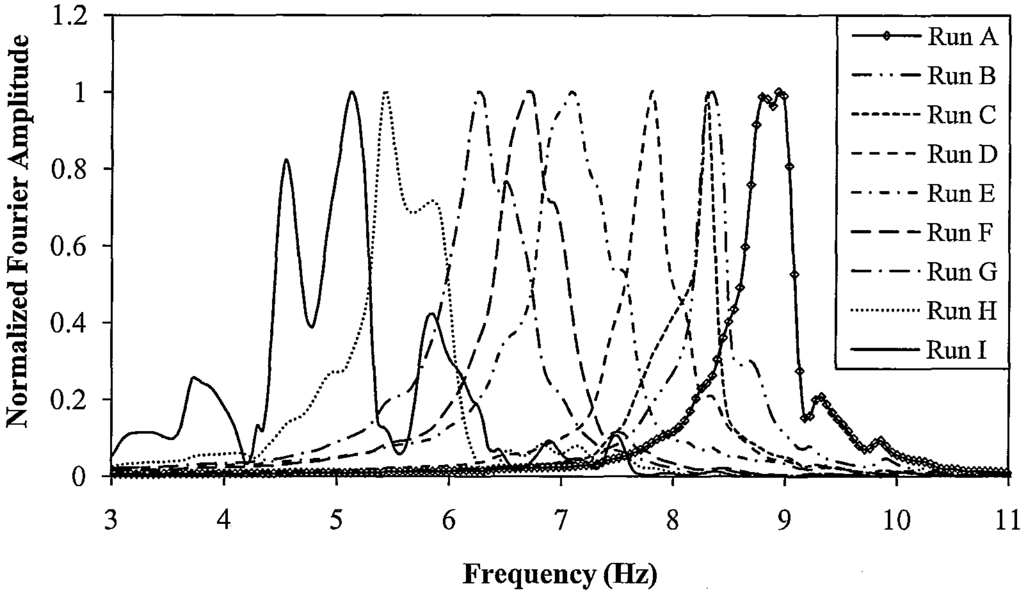

Figure 3.54: Frequency of Wall IIIA with all runs superimposed on the same graph calculated by the FFT

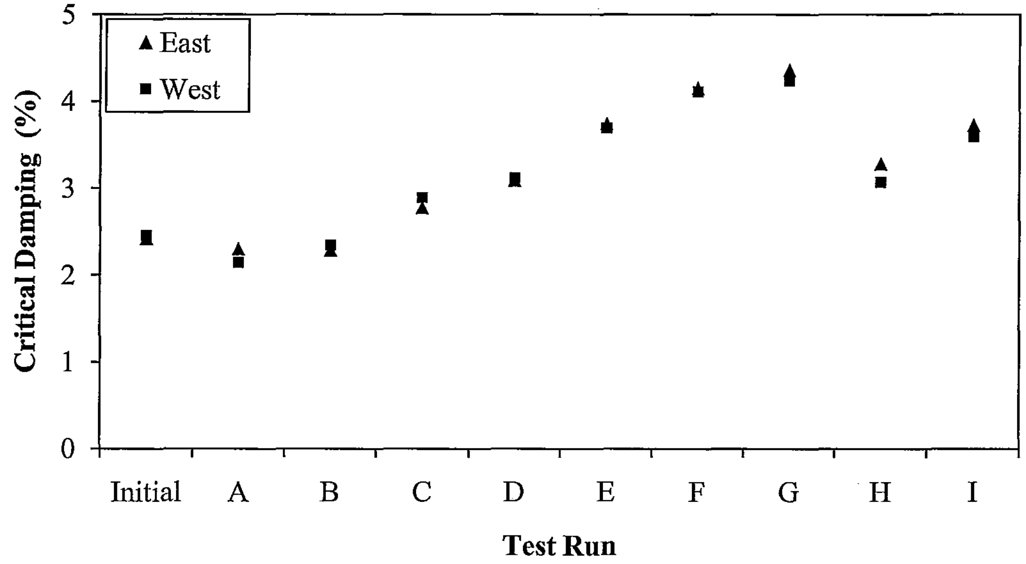

Figure 3.55: Critical damping of Wall IIIA runs calculated from the hammer tap test

# CHAPTER 4: ANALYSIS

## 4.1 Introduction

In this chapter the test results are analyzed and compared to draw some conclusions related to the performance of nominally reinforced partially grouted masonry shear walls under seismic loading. A matrix of five test specimens was designed to study the effects of vertical reinforcement area and spacing without the use of horizontal reinforcement. The amount of reinforcement in the walls had less area and larger spacing than required by Canadian masonry design standard, CSA S304.1 (2004), except for the spacing in the two walls where a third reinforcing bar was present mid-length of the wall.

The most important aspects when dealing with the seismic performance of masonry walls are the general load-displacement behaviour and associated failure mode, lateral load capacity, stiffness, period, displacement ductility and load reduction factors. The above mentioned aspects are discussed in detail.

The secant stiffness was calculated from the load-displacement envelopes, which included the initial and final stiffness. The measured initial and cracked stiffness values were compared to calculated values. The period of the walls was determined from three methods; hammer tap test, FFT and secant stiffness. Corresponding initial and final periods were compared from the outlined methods. An idealized bilinear envelope suggested by Paulay and Priestley (1992) was used to estimate the yield point and displacement ductility of the walls. Once the displacement ductility was evaluated, the load reduction factors were calculated based on the concept of equal energy. This concept was used since the period of the walls was close to or less than the period of peak response (Drysdale et al. 1999).

## 4.2 Overall Hysteretic Response

Type I and III walls had spacing of 1,563 mm at full scale which exceeded the limit of 1,200 mm. They had vertical reinforcing ratios of 0.12% and 0.20%, respectively. Type II walls had spacing of 782 mm at full scale and were within the spacing limit of 1,200 mm. Their vertical reinforcing ratio was 0.17%. The load-displacement envelopes were plotted from the maximum response of each individual run.

The hysteresis envelopes of all five walls are presented in Figure 4.1. All the walls had varied initial stiffness depending on the amount of pre-existing damage due to shrinkage, handling and construction. A closer view of the envelopes is shown in Figure 4.2 at lower drift values. Overall, Type I and III walls had similar response while Type II walls (three cell reinforcement arrangement) had attained higher initial stiffness and higher lateral loads.

Type II walls had a sharper and more defined yield point than compared to Type I and III walls. There was almost no stiffness degradation at lower drift levels. After reaching a certain drift limit, the stiffness changed abruptly due to a decrease in lateral load carrying capacity for both positive and negative displacement directions. In addition, gradual stiffness degradation was more pronounced in the negative displacement direction.

Type III wall with the larger end cell reinforcement was able to attain larger lateral displacements and slightly higher lateral loads than compared to the smaller diameter reinforced Type I walls. Both wall types had gradual stiffness degradation and more developed yield plateaus than that of Type II walls.

All the walls experienced a rocking mechanism when a mortar crack developed across the full length of the wall. No crushing of the masonry and development of shear cracks occurred during testing. Once the full length mortar crack developed, the wall was held in place only by the reinforcement. Type II walls had extra resistance to the development of rocking motion because of the additional anchorage provided by the mid-length reinforcement and grout. The complete response of the walls was not able to be captured due to the limited capacity of the actuator.

## 4.3 Lateral Load Capacity

The calculated flexural and shear capacities of the walls were based on their material properties as determined and discussed in the Experimental Program chapter. Reduction factors were taken as unity. The calculated flexural moment capacity was divided by the total height (from the concrete base to the center of gravity of the mass) to find the ultimate resisting lateral force. The shear capacity of the wall was calculated using the CSA S304.1 (2004). Flexural failure of the walls was expected as their shear capacity was higher.

Calculated and measured lateral loads at yield and ultimate load are presented in Table 4.1. The maximum measured lateral loads of the wall specimens were slightly higher in the positive displacement direction. A direct comparison cannot be made between the measured and predicted ultimate loads since the complete response of the walls was not fully developed due to limited capacity of the actuator driving the shake table platform.

An idealized bilinear envelope was used to predict the yield strength. The method was developed by Paulay and Priestley (1992), which estimates the effective stiffness from the secant to the actual load-displacement curve at 75% of the maximum lateral load. The constant yield plateau was taken as the maximum lateral force obtained during testing. Once the bilinear envelope was developed, the first yield of the reinforcement bars was estimated from the load-displacement curve at the point of yield of the idealized curve.

Table 4.2 shows the measured yield strengths as percentages of the predicted values. The average measured yield of Type I and II walls ranged from 88% to 102% of the predicted yield, while the Type III wall had a measured average yield equal to 67% of the predicted yield. Both Type I and II walls attained yield loads that were closer to their predicted values than the Type III wall with the largest reinforcing ratio of 0.20%. The vertical reinforcement of the Type III wall had a yield stress of 516 MPa than compared to 393 MPa for Type I and II walls.

## 4.4 Stiffness

The secant stiffness of the walls was calculated from the load-displacement envelopes as a ratio between the lateral force and top displacement of the wall. Figure 4.3 presents the secant stiffness versus drift plot for positive and negative directions. A closer view of the plot is shown in Figure 4.4 for low level drift values up to 0.2% (2.0 mm). At low drift levels, the walls had varied initial stiffness and erratic degradation. As the drift level increased, the stiffness degradation trends became smoother. They converged to a similar cracked stiffness value with the exception of Wall IIB, which was not able to attain as high drift levels. The lack of the smooth stiffness degradation at lower drift levels was the consequence of earthquake loading and the wall type. More gradual stiffness degradation would result, especially at lower drift levels, for displacement controlled cyclic tests.

To better show the comparison between the walls, the secant stiffness was normalized by its corresponding maximum value. The normalized stiffness is presented in Figure 4.5, along with a close-up view in Figure 4.6 at lower drift levels. Overall, the walls had similar trend of stiffness degradation with the exception of Walls IIA and IIB in the positive direction at low drift levels. The two walls did not have any stiffness degradation between 0.05% to 0.1% drift, as seen by the horizontal plateaus.

The measured initial stiffness was determined from the linear portion of the load-displacement envelope attained during the first Run, A (lowest amplitude earthquake). The predicted initial stiffness, $k_{initial}$, was calculated by Eq. 4.1.

$$k = \frac{1}{\Delta_f + \Delta_s} = \frac{1}{\frac{h^3}{3E_{m.}I_{initial}} + \frac{1.2h}{G_m.A_e}} \qquad \text{Eq. 4.1}$$

The flexural deformation component, $\Delta_f$, consists of the height, h, modulus of elasticity of the masonry, $E_{m.}$, and un-cracked moment of inertia of the specimen, $I_{initial}$. The shear deformation component, $\Delta_s$, consists of the height, h, shape factor of 1.2 assuming a rectangular section, area of the masonry wall cross-section, $A_e$, and modulus of rigidity, $G_m$, which is equal to $0.4E_{m.}$. The elastic moduli used in Eq. 4.1 were 19,346 MPa and 19,000 MPa for two cell and three cell wall configurations, respectively. The associated $k_m$ factor, relating the modulus of elasticity and compressive strength, as defined by $E_m = k_m f'_m$, was 581 and 583 for two and three cell wall configurations, respectively. The cracked stiffness was calculated by taking the equilibrium of moment areas on opposite sides of the centroid of the transformed cracked section. Once the neutral axis was found, the moment of inertia of the cracked section was calculated about its centroid. The moment of inertia, $I_{cr}$, and area of the cracked section based on depth of compression zone of the cracked cross-section was substituted in Eq. 4.1 to find the cracked stiffness, $k_{cr}$.

Table 4.3 presents the measured and predicted initial and cracked stiffness values of the walls. The measured cracked stiffness was estimated from the secant stiffness at the maximum point of the load-displacement envelopes. The predicted initial stiffness of all three wall types was over 18 kN/mm, while the measured initial stiffness varied from 3.0 kN/mm to 5.8 kN/mm depending on the initial conditions of the wall before start of testing. Table 4.4 presents the measured stiffness as percentages of the predicted values. The measured initial stiffness of the walls varied from 16% to 32% of their predicted initial stiffness values. This may be attributed to the construction of the walls and the boundary conditions at the top and bottom of the walls. The measured cracked stiffness of the walls varied from 30% to 225% of their predicted values. If Walls IIA and IIIA were omitted, the measured cracked stiffness would range from 74% to 113% of their predicted values.

The comparison between the measured initial and final cracked stiffness is presented in Table 4.5. On average, the cracked stiffness ranged from 17% to 41% of their measured initial stiffness values. If Type II walls were excluded, the cracked stiffness would range from 17% to 25% of their measured initial values. This showed that Type II walls had sustained the least amount of damage.

## 4.5 Period

The period of a structure is an essential value to have in seismic design. It will influence the amount of force attracted to the structure during earthquake loading. The period or frequency is related to the circular frequency calculated from the stiffness and mass a structure. The tested walls had the mass lumped at the top while the wall itself provided the stiffness. Equations 4.2 to 4.4 are utilized to estimate the frequency or period of the walls (Chopra 1995).

$$\omega_n = \sqrt{k/m} \qquad \text{Eq. 4.2}$$

$$f_n = {}^{\omega_n}/_{2\pi} \qquad \text{Eq. 4.3}$$

$$T_n = {}^{1}/_{f_n} = {}^{2\pi}/_{\omega_n} \qquad \text{Eq. 4.4}$$

The frequencies of the walls were determined from several methods as already discussed. The first was the hammer tap test, which was only able to estimate the frequency at ambient vibrations. As the damage of the wall accumulated, the hammer tap tests were unable to produce a response that accounted for reduced stiffness of the wall. However, the hammer tap tests were able to estimate representative initial frequencies of the walls. The second method involved the Fast Fourier transform (FFT), which was based on the acceleration response of the wall and the ground acceleration during the runs. The third method estimated the frequencies using the secant stiffness from the load-displacement envelopes.

The period versus drift is presented in Figure 4.7 for both positive and negative directions. They were calculated from the secant stiffness of the walls using Eq. 4.2 to 4.4. Generally, the period of the walls increased linearly with increasing drift values. Table 4.6 shows the measured and predicted initial and cracked periods. The large differences between the measured and predicted periods were already discussed in the last section pertaining to stiffness, which were attributed to the construction and boundary conditions. Table 4.7 shows the average initial period of the walls calculated from the three methods (secant stiffness, FFT, and hammer tap test). The walls had an initial period ranging from 0.08 seconds to 0.11 second. All methods were in good agreement.

The periods were divided by their corresponding largest value to obtain the normalized periods. They are presented in Figure 4.8. In addition, bolded markers are shown on the graph corresponding to the drift level at yield. Generally, all the walls had similar trend of period increase. At lower drift levels, the walls had a non-linear trend. As the drifts increased, the trends became linear. Wall IIA had the largest slope or rate of period increase, while Wall IIIA had the slowest rate of period increase.

The final or cracked periods of the walls are presented in Table 4.8 as determined from the FFT and secant stiffness. The hammer tap test was not included as it was unable to estimate representative periods. The final period of the walls ranged from 0.12 seconds to 0.23 seconds. The periods between the two methods were similar with the exception Wall IB and Wall IIIA where they varied by 0.05 seconds and 0.03 seconds, respectively. Comparisons between the initial and final periods of the walls are presented in Table 4.9. The initial periods of the walls increased by a factor of 2 or more as determined from the secant stiffness method, with the exception of Wall IIA where the period only increased by a factor of 1.45. Using the FFT method, the initial periods were increased by a factor that ranged from 1.77 to 2.02, again with the exception of Wall IIA, where the period only increased by a factor of 1.44.

## 4.6 Displacement Ductility and Load Reduction Factor

Ductility is an indicator of inelastic deformations beyond peak load without significant loss in strength and stiffness. Displacement ductility is defined as:

$$\mu_\Delta = d_u/d_y \qquad \text{Eq. 4.5}$$

where $d_u$ is the maximum post yield lateral displacement and $d_y$ is the lateral displacement at yield. Through the inelastic deformations, a structure is able to dissipate energy. Based on the ductility and energy dissipating capabilities, structures do not need to be designed to remain in the elastic range.

An idealized bilinear envelope suggested by Paulay and Priestley (1992) was used to estimate the displacement ductility of the walls. The initial slope and constant yield plateau were already determined and discussed in the previous capacity section. As such, only the ultimate displacement needed to be found. The usual approach to determine the ultimate displacement is at the point where the wall resists 75% of the maximum lateral load on the descending branch of the actual load-displacement curve. Based on the secant stiffness and ultimate displacements, an idealized ultimate strength is determined by equating the area under actual and idealized curves. Since the complete response of the walls was not attained due to the limited capacity of the actuator, the maximum displacement was taken as the largest displacement attained during the last Run, I. From the idealized displacement values at yield and ultimate load, the ductility of the walls were calculated for both positive and negative displacement regions. The ductility values are presented in the second and third columns of Table 4.10. All the walls had developed displacement ductility over two with the exception of Walls IA and IIA in the negative region. Larger displacement ductility values were attained in the positive directions.

The load reduction factor, $R_d$, is the ratio of the equivalent elastic and inelastic loads. Most of the time, structures are designed for lower lateral forces due to economic reasons. The load reduction factor determines the amount of force reduction based on the displacement ductility. Different relationships exist between the displacement ductility and load reduction factor depending on the period of the structure and the period of peak response of the earthquake. The natural period of the walls was close to or less than the period of peak response of the simulated El-Centro earthquake; hence, the equal energy concept was used to determine the $R_d$ values (Drysdale et al. 1999 and Paulay and Priestley 1992). The load reduction is defined as:

$$R_d = \sqrt{2 * \mu_\Delta - 1} \qquad \text{Eq. 4.6}$$

where $\mu_\Delta$ is the displacement ductility of the wall.

The fourth column of Table 4.10 presents the load reduction factors. The load reductions factors were only calculated for the larger ductility level, which was in the positive displacement region. The load reduction factors were similar, ranging from 1.9 to 2.6. Wall IB had the largest load reduction factor of 2.6.

## 4.7 Closure

The main focus of this study was to asses the performance of partially grouted nominally reinforced concrete masonry shear walls having less steel and larger spacing than specified by the CSA S304.1 (2004), for seismic requirements. Reduced scale walls were constructed to study their behaviour under dynamic loading of the 1940 El-Centro earthquake N-S component. Key aspects of the wall were examined pertaining to the general response of the walls, load carrying capacity, stiffness, period, displacement ductility and load reduction factors. The following analysis and conclusions of the above aspects are summarized:

1. Rocking type behaviour was present in all the walls during higher amplitude earthquake runs. No significant shear cracking and crushing of masonry occurred during testing.
2. Before the start of rocking, the hysteresis loops were small and narrow. After the onset of rocking, the loops increased in size. The walls were able to dissipate energy through the rocking motion.
3. The load-displacement response between the two end cell and three end cell reinforcement arrangements were different. The three cell wall arrangement had larger initial stiffness and higher lateral load. Full response of the walls was not attained due to the limited capacity of the actuator.

4. The measured average first yield strengths determined from the idealized bilinear curve of Type I and II walls were 88% to 102% of their predicted first yield. Type III wall had a measured first yield equal to 67% of the predicted first yield.

5. In general, the walls had similar stiffness degradation. The measured initial average stiffness of the wall was between 16% and 32% of the predicted initial stiffness. The final measured stiffness values were reduced by 17% to 41% of the initial measured stiffness at maximum drifts.

6. The periods of the walls were increased by factor of 2 or more with the exception of Wall IIA. Generally, the period of the walls increased linearly for increasing drift levels.

7. All the walls had developed displacement ductility over two in the positive displacement region.

8. The load reduction factors were calculated from the positive displacement region ductility. The R values ranged from 1.9 to 2.6.

Table 4.1: Measured and predicted lateral load capacities

| Wall Specimen | Measured Load[3] (kN) | | Predicted Load (kN) | | | |
|---|---|---|---|---|---|---|
| | **Ultimate[1]** | **Yield[2]** | **Ultimate[1]** | **Yield** | **Shear Sliding** | **Shear Diag.** |
| IA | 3.74<br>(3.65) | 3.23<br>(3.15) | 3.86 | 3.55 | 7.88 | 9.26 |
| IB | 3.89<br>(3.60) | 3.20<br>(3.05) | | | | |
| IIA | 4.36<br>(4.42) | 3.65<br>(3.87) | 4.75 | 3.91 | 12.01 | 9.26 |
| IIB | 4.59<br>(4.40) | 3.90<br>(4.08) | | | | |
| IIIA | 4.38<br>(4.11) | 3.70<br>(3.65) | 6.00 | 5.55 | 7.88 | 9.26 |

[1] Predicted and measured ultimate loads not directly comparable

[2] Determined from idealized bilinear curve

[3] The values inside brackets represent negative displacement region

Table 4.2: Comparison of measured/predicted yield strenghts

| Wall Specimen | Measured / Predicted Yield Strength (%) | | |
|---|---|---|---|
| | **Positive Region** | **Negative Region** | **Average** |
| IA | 91 | 88.7 | 90 |
| IB | 90 | 85.9 | 88 |
| IIA | 93 | 99.0 | 96 |
| IIB | 100 | 104 | 102 |
| IIIA | 68 | 66 | 67 |

Table 4.3: Measured and predicted secant stiffness

| **Wall Specimen** | **Measured Stiffness[1] (kN/mm)** | | **Predicted Stiffness (kN/mm)** | |
|---|---|---|---|---|
| | **Initial** | **Cracked** | **Initial** | **Cracked** |
| IA | 3.9<br>(4.0) | 0.9<br>(1.1) | 18.2 | 1.0 |
| IB | 4.6<br>(4.6) | 0.7<br>(0.9) | | |
| IIA | 5.2<br>(5.8) | 1.8<br>(2.7) | 18.4 | 1.2 |
| IIB | 4.4<br>(4.1) | 1.4<br>(1.1) | | |
| IIIA | 3.3<br>(3.0) | 0.7<br>(0.7) | 18.7 | 2.2 |

[1] The values inside brackets represent negative displacement region

Table 4.4: Comparison of measured/predicted initial and cracked stiffness

| **Wall Specimen** | **Measured / Predicted Stiffness[1] (%)** | |
|---|---|---|
| | **Initial** | **Cracked** |
| IA | 22<br>(22) | 89<br>(113) |
| IB | 25<br>(25) | 74<br>(86) |
| IIA | 28<br>(32) | 151<br>(225) |
| IIB | 24<br>(22) | 116<br>(90) |
| IIIA | 18<br>(16) | 30<br>(31) |

[1] The values inside brackets represent negative displacement region

Table 4.5: Measured cracked/initial stiffness

| **Wall Specimen** | **Cracked / Initial Measured Stiffness (%)** | | |
|---|---|---|---|
| | **Positive Displacement Region** | **Negative Displacement Region** | **Average** |
| IA | 22 | 28 | 25 |
| IB | 16 | 18 | 17 |
| IIA | 35 | 47 | 41 |
| IIB | 32 | 27 | 30 |
| IIIA | 19 | 22 | 21 |

Table 4.6: Measured and predicted period of the walls

| **Wall Specimen** | **Measured Period$^{1,2}$ (s)** | | **Predicted Period (s)** | |
|---|---|---|---|---|
| | **Initial** | **Cracked** | **Initial** | **Cracked** |
| IA | 0.09<br>(0.09) | 0.20<br>(0.18) | 0.04 | 0.19 |
| IB | 0.09<br>(0.09) | 0.22<br>(0.20) | | |
| IIA | 0.08<br>(0.08) | 0.14<br>(0.11) | 0.04 | 0.17 |
| IIB | 0.09<br>(0.09) | 0.16<br>(0.18) | | |
| IIIA | 0.10<br>(0.11) | 0.23<br>(0.23) | 0.04 | 0.13 |

[1] Based on secant stiffness from load displacement plots

[2] Terms in brackets represent negative displacement region

Table 4.7: Initial period comparison

| **Wall Specimen** | **Initial Period (sec)** | | |
|---|---|---|---|
| | **Secant Stiffness**[1] | **FFT** | **Tap Test** |
| IA | 0.09 | 0.11 | 0.10 |
| IB | 0.09 | 0.08 | 0.08 |
| IIA | 0.09 | 0.08 | 0.08 |
| IIB | 0.08 | 0.09 | 0.08 |
| IIIA | 0.11 | 0.11 | 0.11 |

[1] average between positive and negative displacement regions values

Table 4.8: Final period comparison

| **Wall Specimen** | **Final Period (sec)** | |
|---|---|---|
| | **Secant Stiffness**[1] | **FFT** |
| IA | 0.19 | 0.19 |
| IB | 0.21 | 0.16 |
| IIA | 0.13 | 0.12 |
| IIB | 0.17 | 0.18 |
| IIIA | 0.23 | 0.20 |

[1] average between positive and negative displacement regions

Table 4.9: Final/initial period comparison

| **Wall Specimen** | **Final / Initial Period (%)** | |
|---|---|---|
| | **Secant Stiffness**[1] | **FFT** |
| IA | 200 | 195 |
| IB | 233 | 200 |
| IIA | 145 | 144 |
| IIB | 200 | 202 |
| IIIA | 290 | 177 |

[1] average between positive and negative displacement regions

Table 4.10: Displacement ductility and corresponding load reduction factors

| **Wall Specimen** | $\mu_\Delta$[1] |  | $R_d$[2] |
|---|---|---|---|
|  | **Positive Displacement Region** | **Negative Displacement Region** |  |
| IA | 2.4 | 1.5 | 1.9 |
| IB | 3.9 | 2.4 | 2.6 |
| IIA | 2.7 | 1.8 | 2.1 |
| IIB | 2.9 | 2.2 | 2.2 |
| IIIA | 3.1 | 2.3 | 2.3 |

[1] Ductility calculated from the maximum displacement attained during testing

[2] Based on equal energy approach from the larger displacement ductility values

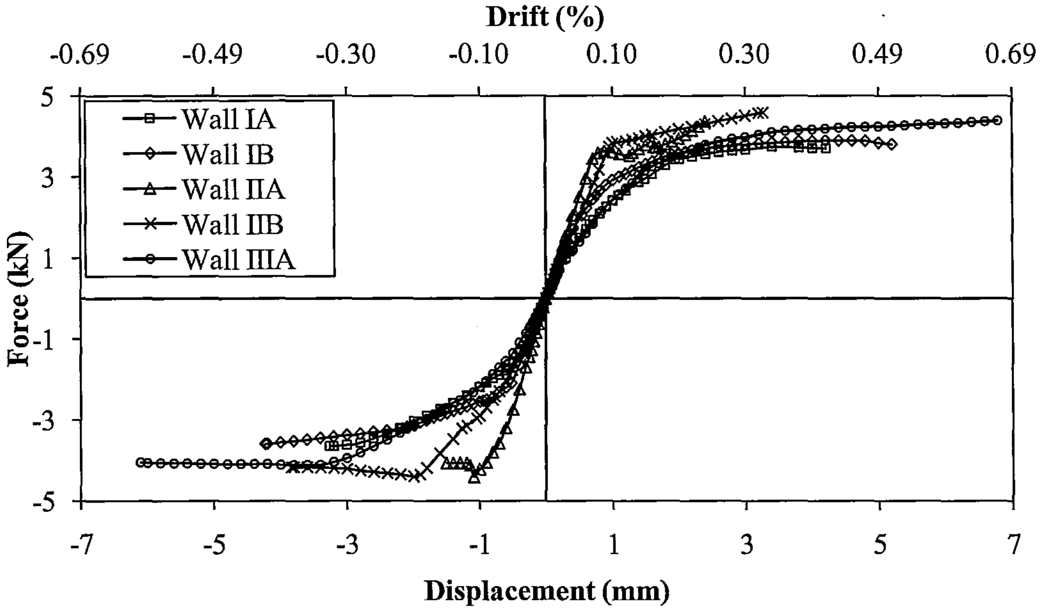

Figure 4.1: Hysteresis envelopes of all walls

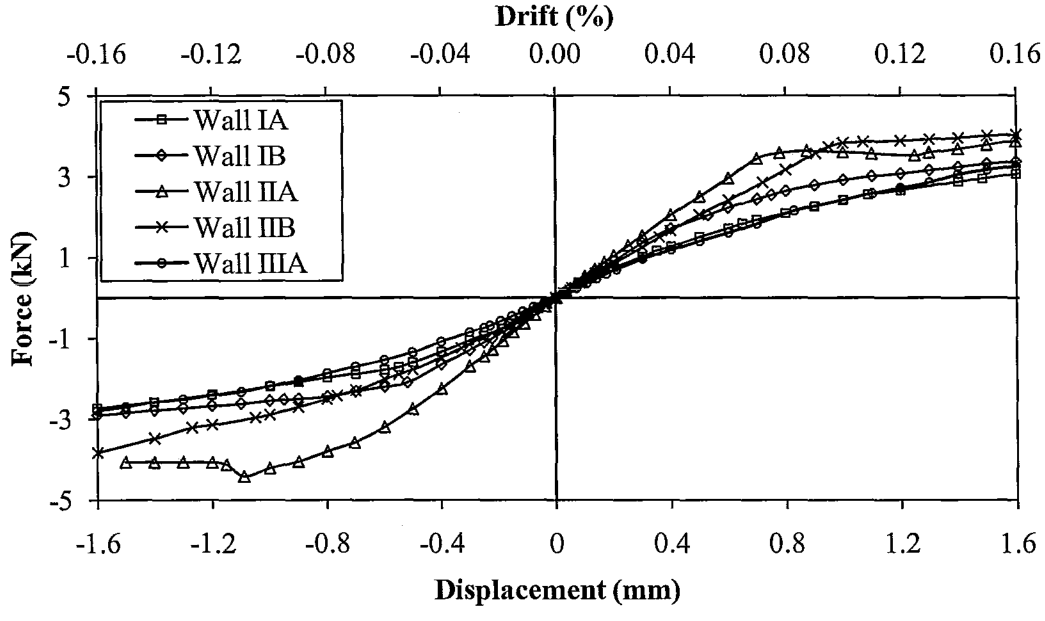

Figure 4.2: Initial hysteresis envelopes at low level drifts

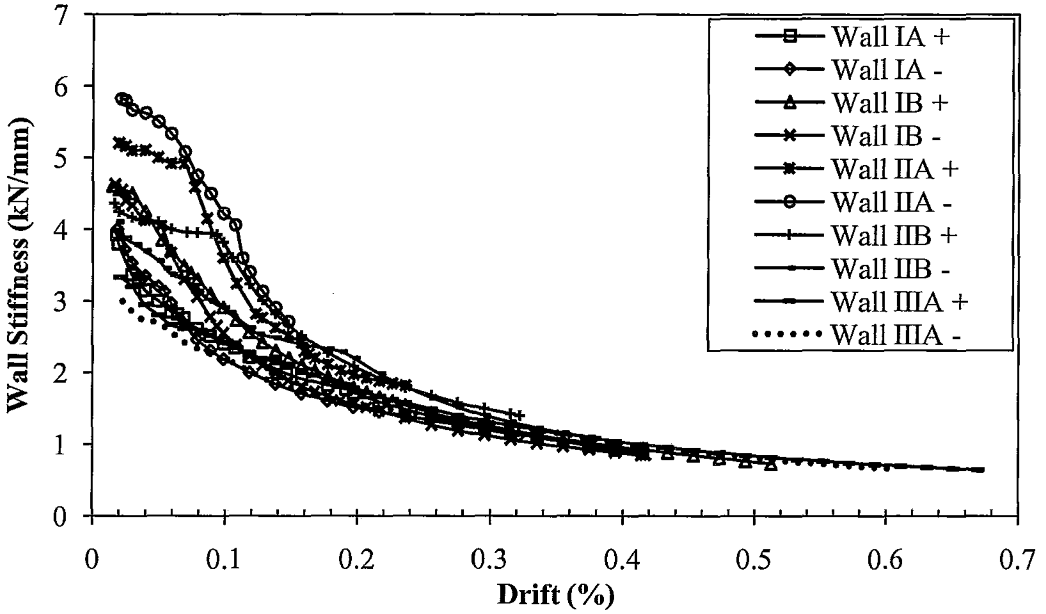

Figure 4.3: Secant stiffness versus drift

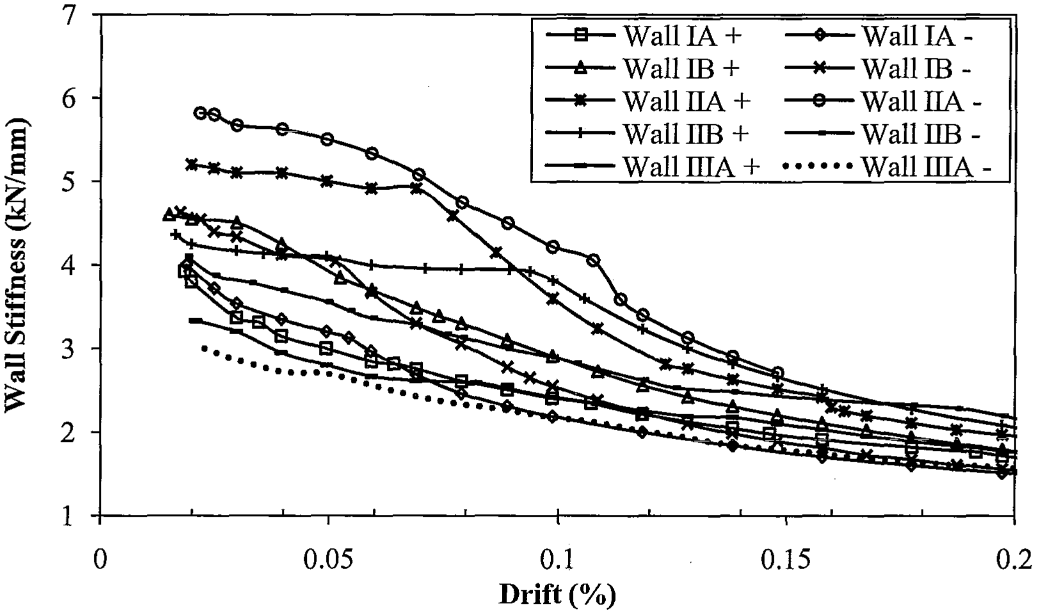

Figure 4.4: Secant stiffness at low level drifts

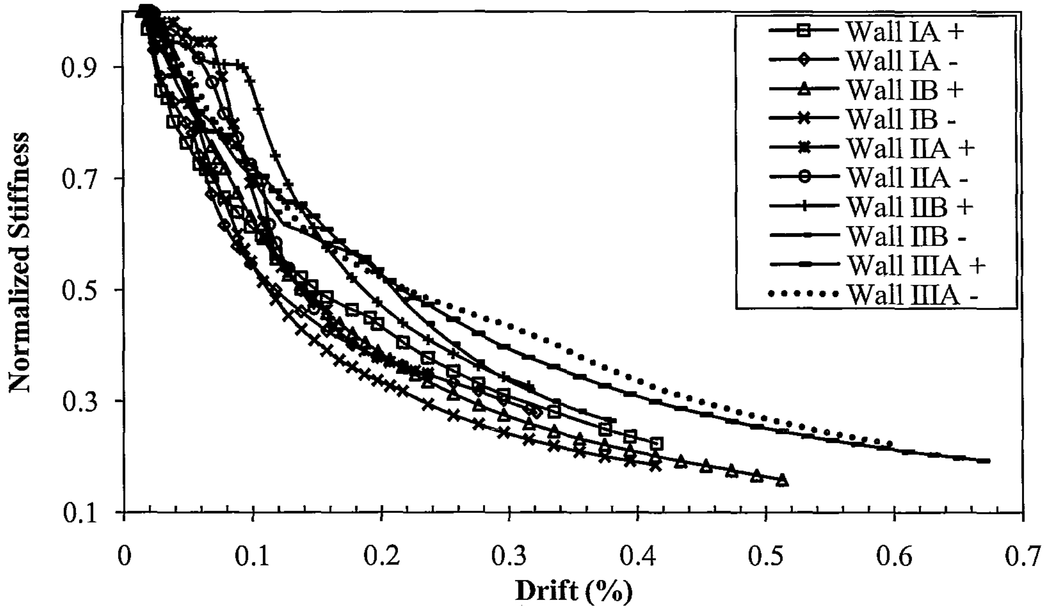

Figure 4.5: Normalized secant stiffness versus drift

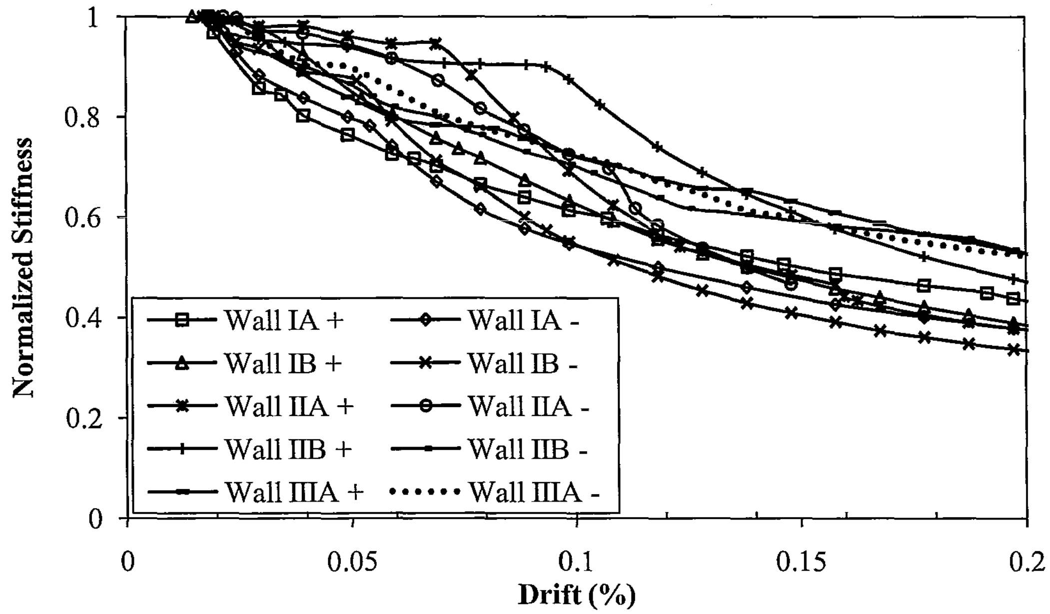

Figure 4.6: Normalized secant stiffness at low level drifts

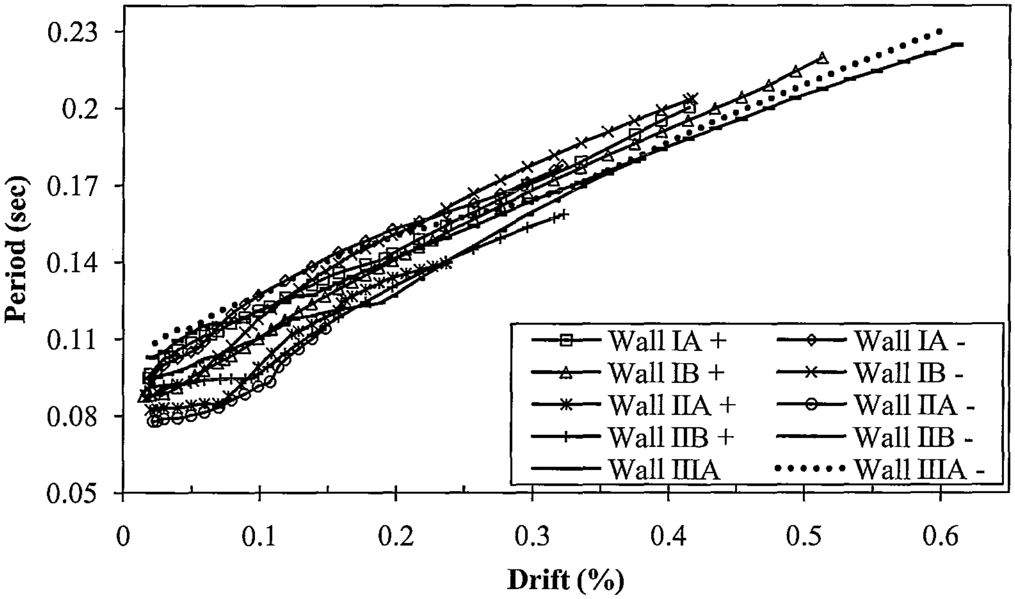

Figure 4.7: Period versus drift

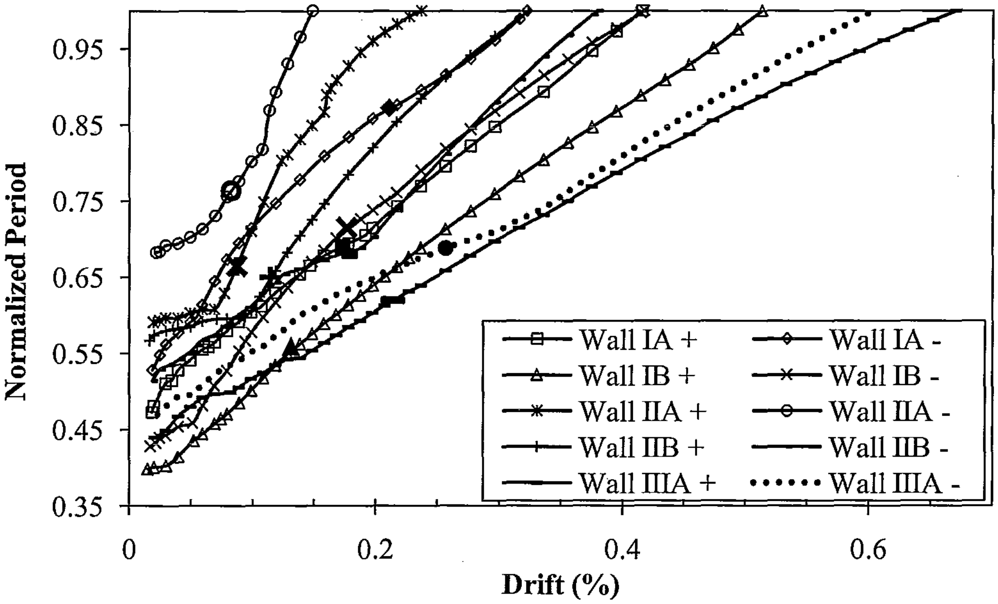

Figure 4.8: Normalized period versus drift

# CHAPTER 5: SUMMARY AND CONCLUSIONS

## 5.1 Summary

The experimental program was initiated with the objective to study the performance of nominally reinforced partially grouted shear walls under simulated dynamic loading on a shake table. Five walls were subjected to nine increasing amplitude runs of the 1940 El-Centro earthquake N-S component. This earthquake was selected because of its extended use as a benchmark reference and its high response close to the natural frequency of the walls. The walls were constructed from reduced scale model blocks due to the limited capacity of the shake table. Direct reduced scale modeling techniques pertaining to dynamic loading were utilized to study the behaviour of the walls.

The partially grouted masonry shear walls were constructed having less steel and larger spacing than specified by the current Canadian masonry standard, CSA S304.1 (2004), for seismic hazard index equal to and greater than 0.35. The walls were grouped into three Types, I, II and III based on their vertical reinforcement ratio corresponding to 0.12%, 0.17% and 0.20%, respectively. Type I and III walls had the end cells of the wall reinforced with spacing of 469 mm (corresponding to 1,563 mm at full scale). This spacing exceeded the limit permitted by the Canadian masonry standard, CSA S304.1 (2004). Type II walls had a smaller spacing of 235 mm (corresponding to 782 mm at full scale) since an additional reinforcing bar was present mid-length of the wall.

Constituent testing was completed to determine the properties of the mortar, grout and steel reinforcement, along with pull-out and compression prism tests. The results were discussed and summarized. Details of the test setup, instrumentation and loading procedure were provided.

The results of the individual walls were discussed in Chapter 3. Each wall had a discussion pertaining to the observations and progression of cracking, load-displacement response, mode shape, frequency and damping values.

Chapter 4 presented collective analyses of characteristics involving the behaviour and response, load carrying capacity, stiffness, period, displacement ductility and lateral load reduction factors.

## 5.2 Conclusions

### 5.2.1 Wall Behaviour and Response

The general behaviour of the shear walls was dominated by rocking motion. As the amplitude of the simulated earthquake was increased, a weak horizontal mortar plane started to develop until a full length mortar crack was formed. The location of the full length mortar crack was concentrated in the bottom part of the wall, ranging from the base to the fourth mortar joint course. Essentially, once the mortar crack developed, the wall became separated from the bottom section and began to rock. At that point the wall was held in place only by the vertical reinforcement. The full response of the wall was not attained due to the limited capacity of the actuator. However, all the walls were subject to the same increasing amplitude earthquake runs, which made comparison possible.

Some walls developed mortar step cracks in addition to the full length horizontal mortar crack. With the exception of these two damage patterns, no crushing of masonry and development of shear cracks occurred during testing. There were other minor mortar cracks present. Most of the cracks were concentrated in the bottom sections while some were located further up the walls.

The envelopes of Type I and III walls had similar response that consisted of gradual stiffness degradation and constant yield plateaus. Type II walls had increased stiffness and higher maximum lateral force with no yield plateaus. The damping of the walls started to become evident after the onset rocking. Once the rocking of the wall began, the area inside the loops became larger. The rocking motion was able to dissipate energy instead of the more common diagonal cracking and crushing of masonry.

### 5.2.2 Lateral Load Capacity

Flexural failure of the walls was expected as the predicted shear strength was higher. The flexural and shear strengths were calculated based on the Canadian masonry standard, CSA S304.1 (2004). A direct comparison was not possible between the measured and predicted ultimate loads since the complete response of the walls was not fully developed due to limited capacity of the actuator. The predicted yield strengths were determined from an idealized bilinear envelope. The average measured yield strengths ranged from 88% to 102% of the calculated yields for Type I, II walls, while the Type III wall attained an average yield equal to 67% of the calculated yield.

### 5.2.3 Stiffness

In general, all the walls had similar trend of stiffness degradation after 0.20% drift. The measured initial stiffness was found to vary between 16% and 32% of the predicted initial stiffness. The secant stiffness decreased gradually to values ranging from 17% to 41% of the measured initial stiffness at the maximum drift achieved during the last run.

### 5.2.4 Period

The initial periods of the walls were determined from three methods; hammer tap test, secant stiffness of the load-displacement envelope and the FFT between the acceleration response of the wall and the ground acceleration. The initial period of the walls ranged from 0.08 seconds to 0.11 seconds. All three methods were in good agreement. The progression of the period was calculated from the secant stiffness in order to calculate the period at incremental drift values. Generally, the period increased linearly as drift increased. The hammer tap test was only representative at ambient vibrations; hence, it was not used in the period analysis with the exception of the initial period. The initial periods of the walls were increased approximately by a factor of two or more with the exception of Wall IIA.

### 5.2.5 Displacement Ductility and Load Reduction Factor

The ductility of the walls was calculated from an idealized bilinear curve. Similarly, the load reduction factor, $R_d$, was calculated using the displacement ductility attained from the idealized bilinear curve. The natural periods of the walls were close to or less than the period of peak response of the simulated El-Centro earthquake; hence, the equal energy concept was used to determine the load reduction factors. The developed ductility of the walls was found to be greater than two with the exception of Walls IA and IIA in the negative displacement region. The load reduction factors were calculated for the larger positive displacement region. The values ranged from 1.9 to 2.6.

## 5.3 Recommendations for Future Work

Further research should be conducted regarding nominally reinforced partially grouted shears walls on the aspects of:

1. Testing walls to failure to determine the complete response.
2. Full scale comparison study of partially grouted shear walls completed under dynamic loading where facilities exist.
3. Further experimental data should be collected for varying levels of axial load, aspect ratios and reinforcement arrangements.

# REFERENCES

Abboud, Bechara E., Hamid, Ahmad A., and Harris, Harry G. (1990), "Small-Scale Modeling of Concrete Block Masonry Structures", Structural Journal, ACI, vol. 87, no. 2, pp. 145-155

Abrams, Daniel P., and Paulson, Thomas J. (1991), "Modeling Earthquake Response of Concrete Masonry Building Structures", Structural Journal, ACI, vol. 88, pp. 475-485

Al-Chaar, G.K., and Hasan, H.A. (2002), "Dynamic Response and Seismic Testing of CMU Walls Rehabilitated with Composite Material Applied to only one side", Structures & Buildings, vol. 152, no. 2, pp. 135-146

ASTM International, (2009), ASTM C140-09, Standard Test Methods for Sampling and Testing Concrete Masonry Units and Related Units, West Conshohocken, PA.

ASTM International, (2007), ASTM A82/A82M-07, Standard Specification for Steel Wire, Plain, for Concrete Reinforcement, West Conshohocken, PA.

ASTM International, (2003b), ASTM C1019-03, Standard Test Method for Sampling and Testing Grout, West Conshohocken, PA.

Bazant, Zdanek P., and Chen Er-Ping (1997), "Scaling of Structural Failure", Applied Mechanics Review 50, no 10, pp 593-627

Canadian Standards Association, (2004a), CSA A165.1, CSA Standards on Concrete Masonry Units, Toronto, Ontario

Canadian Standards Association, (2004b), CSA S304.1-04, Design of Masonry Structures, Mississauga, Ontario

Canadian Standards Association, (2004), CSA A179-04, Mortar and Grout for Unit Masonry, Mississauga, Ontario

Canadian Standards Association, (1990), CSA A369.1-M90, Method of Test for Compressive Strength of Masonry Prisms, Toronto, Ontario

Chopra, A.K (1995), "Dynamic of Structures", Prentice Hall

Drysdale, Robert G., and Hamid, Ahmad A. (2005), "Masonry Structures: Behaviour and Design", Canadian Edition, Canadian Masonry and Design Centre, Mississauga, Ontario

ElGawady, Mohamed A., Lestuzzi, Pierino, and Badoux, Marc (2005), "Performances of Masonry Walls Under In-plane Seismic Loading", TMS Journal December 2005, pp. 85-102

Elshafie, Hany, Hamid, Ahmad, and Nasr, El-sayed (2002), "Strength and Stiffness of Masonry Shear Walls with Opening", TMS Journal December 2002, pp. 49-60

Farrar, C. R., Baker, W. E., and Dove, R. C. (1994), "Dynamic Parameter Similitude for Concrete Models", ACI Structural Journal, Vol. 91, Iss. 1, pp. 90-99

Fattal, S. G. (1993a), "Strength of Partially Grouted Shear Walls under Lateral Loads", U.S. Department of Commerce, NISTIR 5147, National Institute of Standards and Technology, Gaithersburg, Maryland, June 1993

Fattal, S. G. (1993b), "The Effect of Critical Parameters on the Behavior of Partially Grouted Masonry Shear Walls under Lateral Loads", U.S. Department of Commerce, NISTIR 5116, National Institute of Standards and Technology, Gaithersburg, Maryland, June 1993

Ghanem, Gouda M., Salama, Amr E., Elmagd, Shreif Abu, and Hamid, Ahmad A. (1993), "Effect of Axial Cmpression on the Behavior of Partially Reinforced Masonry Shear Walls", The Sixth North American Masonry Conference, pp. 1145-1157

Haider, W., and Dhanasekar, M. (2004), "Experimental Study of Monotonically Loaded Wide Spaced Reinforced Masonry Shear Walls", Australian Journal of Structural Engineering, vol. 5, no. 2, pp. 101-118

Hamid, A. A., Ziab, G., and El Nawany O. (1987), "Modulus of Elasticity of Concrete Block Masonry", In Proceedings of the Fourth North American Masonry Conference, Los Angeles, CA., 1987, pp. 7/1-7/13

Hamid, A. A., and Chandrakeerthy, S.R. De S. (1992), "Compressive Strength of Partially Grouted Concrete Masonry Using Small Scale Wall Elements", TMS Journal August 1992, pp. 75-85

Harris, Harry G., and Sabnis, Gajanan M. (1999), "Structural Modeling and Experimental Techniques", Second Edition, CRC Press

Ingham, Jason M., Davidson, Barry J., Brammer, David R., and Voon, Kok C. (2001), "Testing and Codification of Partially Grout-filled Nominally-reinforced Concrete Masonry Subjected to In-plane Cyclic Loads", TMS Journal September 2001, pp. 83-96

Long, Larisa Maxine (2006), "Behaviour of Half-Scale Reinforced Concrete Masonry Shear Walls", M.A. Sc. Thesis, Department of Civil Engineering, McMaster University, Hamilton, Ontario

Maleki, Majid (2008), "Behaviour of Partially Grouted Reinforced Masonry Shear Walls Under Cyclic Reversed Loading", Ph.D. Thesis, Department of Civil Engineering, McMaster University, Hamilton, Ontario

Matsumura, A. (1985), "Effect of Shear Reinforcement in Concrete Masonry Walls", First Joint Technical Coordinating Committee on Masonry Research, U.S.-Japan Coordinated Earthquake Research Program, Tokyo, Japan, August 26-27, 1985, pp. 1-7

Mirza, M. S., Harris, H. G., and Sabnis, G. M. (1979), "Structural Models in Earthquake Engineering", In Proceedings of the Third Canadian Conference of Earthquake Engineering, June 4-6, Montreal, Quebec, Vol. 1, pp. 511-549

Noor, F.A., and Boswell, L.F. (1992), "Small Scale Modeling of Concrete Structures", Elsevier Science Publishers

Schultz, A. E. (1996), "Seismic Resistance of Partially-Grouted Masonry Shear Walls", Worldwide Advances in Structural Concrete and Masonry, pp. 211-222

Shing, P. Benson, Noland, J.L., Klamerus, E., and Spach, H. (1989), "Inelastic Behavior of Concrete Masonry Shear Walls", Journal of Structural Engineering, ASCE, Vol. 115, No. 9, September 1989

Thurston, S.J., and Hutchison, D.L. (1982), "Reinforced Masonry Shear Walls: Cyclic Load Tests in Contraflexure", Buletin of The New Zealand National Society for Earthquake Engineering, vol. 15, no. 1, March 1982 pp. 27-45

Turek, Martin, Ventura, Carlos E., and Kuan, Steven (2007), "In-Plane Shake-Table Testing of GFRP-Strengthened Concrete Masonry Walls", Earthquake Spectra, vol. 23, no. 1, pp. 223-237

Voon, K.C., (2007), "In Plane Sesimic Design of Concrete Masonry Structures", Ph.D. Thesis, Department of Civil and Environmental Engineering, The University of Auckland, New Zeleand

Voon, K.C., and Ingham, J.M. (2005), "Experimental Study of Partially Grouted Concrete Masonry Walls with Openings", In Proceedings, 10th Canadian Masonry Symposium, Banff, Alberta

Zarnic, R., Gostic, S., Crewe, A. J., and Taylor, C.A. (2001), "Shaking Table Tests of 1:4 Reduced-Scale Models of Masonry Infilled Reinforced Concrete Frame Buildings", Earthquake Engineering and Structural Dynamics, Vol. 30, pp. 819-834

# APPENDIX

## A1.1 Calculations

Properties for each wall type were calculated pertaining to the reinforcement ratio, axial stress, ultimate strength, yielding conditions, initial and cracked stiffness and frequency and cracking moment. The masonry and steel material properties and cross-sectional areas used in the calculations are presented in Tables A1.1, A1.2, and A1.3.

Table A1.1: Masonry properties

| Quantity | Masonry | |
|---|---|---|
| | Grouted | Ungrouted |
| Strength (MPa) | 27.8 | 34.8 |
| Modulus of Elasticity (MPa) | 16,770 | 20,038 |

Table A1.2: Steel properties

| Quantity | Steel Reinforcement | |
|---|---|---|
| | 3.66 mm Ø | 4.76 mm Ø |
| Area (mm$^2$) | 10.52 | 17.80 |
| Yield Strength (MPa) | 393 | 516 |
| Modulus of Elasticity (MPa) | 181,955 | 206,266 |
| Yielding Strain | 0.002160 | 0.002502 |

Table A1.3: Effective area and axial load

| Wall Type | Effective Area (mm$^2$) | Axial Load (kN) |
|---|---|---|
| I | 17,618 | 8.76 |
| II | 18,614 | 8.76 |
| III | 17,618 | 8.76 |

### A1.1.1 Type I Wall

The reinforcement arrangement is presented for the two cell 3.66 mm diameter steel arrangement:

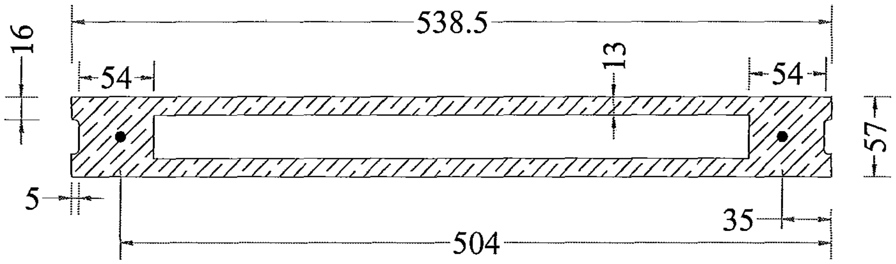

Figure A1.1: Two cell 3.66 mm diameter steel arrangement (hatched area, $A_m$ = 17,618 mm$^2$)

**Reinforcement ratio**

$$\rho_v = \frac{2 * A_s}{A_e} = \frac{2 * 10.52\ \text{mm}^2}{17{,}618\ \text{mm}^2} = 0.12\%$$

**Axial stress**

$$\sigma_{net} = \frac{P_d}{A_e} = \frac{8755.425\ \text{N}}{17{,}618\ \text{mm}^2} = 0.50\ \text{MPa}$$

**Flexural strength**

$$\beta_1 = 0.8 - 0.1\left(\frac{27.8-20}{10}\right) = 0.722$$

$$P_d = C - \sum T$$

$$P_d = 0.85 f'_m\,(b\beta_1 c) - A_s f_y - \left(\frac{34.8 - c}{c}\right)\varepsilon_u E_s A_s$$

$$c = 19.3\ \text{mm}$$

$$\mathrm{M_u} = \mathrm{C}\left(\frac{\ell_\mathrm{w}}{2} - \frac{\beta_1 \mathrm{c}}{2}\right) - \mathrm{T_1}\left(\frac{\ell_\mathrm{w}}{2} - 503.7\ \mathrm{mm}\right) - \mathrm{T_2}\left(\frac{\ell_\mathrm{w}}{2} - 34.8\ \mathrm{mm}\right)$$

$$\mathrm{M_u} = 4.46\ \mathrm{kN} * \mathrm{m}$$

$$\mathrm{V_u} = \frac{4.46\ \mathrm{kN} * \mathrm{m}}{1.16\ \mathrm{m}} = 3.86\ \mathrm{kN}$$

**First yield**

$$\mathrm{P_d} = \mathrm{C} - \sum \mathrm{T}$$

$$\mathrm{P_d} = 0.5\mathrm{f}'_\mathrm{m}\,(\mathrm{b_w kd}) + \mathrm{A_{sc}f_y} - \mathrm{A_s f_y}$$

$$\begin{aligned}\mathrm{P_d} = 0.5\frac{\mathrm{E_m}\varepsilon_\mathrm{s}(\mathrm{kd})}{(503.7\ \mathrm{mm} - \mathrm{kd})} &* [(58.5\mathrm{mm} * 57\ \mathrm{mm}) + 26\ \mathrm{mm} * (\mathrm{kd} - 58.5)] \\ &+ 10.52\ \mathrm{mm}^2 * \left(\frac{34.8 - \mathrm{c}}{503.7\ 0 - \mathrm{c}}\right) * 393\ \mathrm{MPa} - 10.52\ \mathrm{mm}^2 \\ &* 393\ \mathrm{MPa}\end{aligned}$$

$$\mathrm{kd} = 77.04\ \mathrm{mm}$$

$$\mathrm{M_y} = \mathrm{C}\left(\frac{\ell_\mathrm{w}}{2} - \frac{\mathrm{kd}}{3}\right) - \mathrm{A_{sc}f_y}\left(\frac{\ell_\mathrm{w}}{2} - 34.8\ \mathrm{mm}\right) - \mathrm{A_s f_y}\left(\frac{\ell_\mathrm{w}}{2} - 503.7\ \mathrm{mm}\right)$$

$$\mathrm{M_y} = 4.11\ \mathrm{kN} * \mathrm{m}$$

$$\mathrm{V_y} = \frac{4.11\ \mathrm{kN} * \mathrm{m}}{1.16\ \mathrm{m}} = 3.55\ \mathrm{kN}$$

**Sliding shear strength**

$$\begin{aligned}\mathrm{V_r} &= \mu \mathrm{P_2} \\ &= 1.0 * (0.9 * 8755.425\ \mathrm{N}) \\ &= 7.88\ \mathrm{kN}\end{aligned}$$

**Shear diagonal strength**

$$V_r = (v_m b_w d_v + 0.25P_d)\gamma_g$$

$$= \left(\left(0.16\left(2 - \frac{M_f}{V_f d_v}\right)\sqrt{f'_m}\right) b_w * 0.8\ell_w + 0.25P_d\right)\gamma_g$$

$$= 9.26 \text{ kN}$$

**Initial stiffness and frequency**

$$I_{initial} = \text{Flanges of Wall} + 2 \text{ End Cells} + 2 \text{ Transformed Steel}$$

$$I_{initial} = 464.62 \text{ x } 10^6 \text{ mm}^4$$

$$k_{initial} = \frac{1}{\Delta_f + \Delta_s} = \frac{1}{\frac{h^3}{3E_m.I_{initial}} + \frac{1.2h}{0.4E_m.A_{net}}}$$

$$\Delta_f = 0.000044602 \text{ mm/N}$$

$$\Delta_s = 0.000010296 \text{ mm/N}$$

$$k_{initial} = 18215.32 \text{ N/mm}$$

$$\omega_n = \sqrt{\frac{k_{initial}}{m}} = \sqrt{\frac{18215.32 \text{ x } 10^3 \text{ N/mm}}{892.5 \text{ kg}}} = 142.86 \text{ rad/s}$$

$$f_n = \frac{\omega}{2\pi} = 22.74 \text{ Hz}$$

**Cracked stiffness and frequency**

$$n = \frac{E_s}{E_m} = \frac{181955 \text{ MPa}}{16770 \text{ MPa}} = 9.2656$$

$$nA_s\left(\frac{d - kd}{kd}\right)f'_m = \frac{f'_m}{2}bkd$$

$$kd = 39.83 \text{ mm}$$

$$I_{cr} = \frac{b(kd)^3}{12} + bkd\left(\frac{kd}{2}\right)^2 + nA_s(d - kd)^2 = \frac{b(kd)^3}{3} + nA_s(d - kd)^2$$

$$I_{cr} = 22.174 \text{ x } 10^6 \text{ mm}^4$$

$$k_{cr} = \frac{1}{\Delta_f + \Delta_s} = \frac{1}{\frac{h^3}{3E_m I_{cr}} + \frac{1.2h}{0.4E_m A_e}}$$

where $A_e = kd * 57 \text{ mm}$

$\Delta_f = 0.000934577$ mm/N

$\Delta_s = 0.000079898$ mm/N

$k_{cr} = 985.73 \text{ N/mm}$

$$\omega_n = \sqrt{\frac{k_{cr}}{m}} = \sqrt{\frac{985.73 \text{ x } 10^3 \text{ N/mm}}{892.5 \text{ kg}}} = 33.23 \text{ rad/s}$$

$$f_n = \frac{\omega_n}{2\pi} = 5.29 \text{ Hz}$$

**Cracking conditions**

$$M_{cr} = \left(\frac{f_t + f_{cs}}{y_t}\right) * I_{initial}$$

$$M_{cr} = 1.49 \text{ kN} * \text{m}$$

$$V_{cr} = \frac{1.49 \text{ kN} * \text{m}}{1.16 \text{ m}} = 1.29 \text{ kN}$$

### A1.1.2 Type II Wall

The reinforcement arrangement is presented for the three cell 3.66 mm diameter reinforcement configuration:

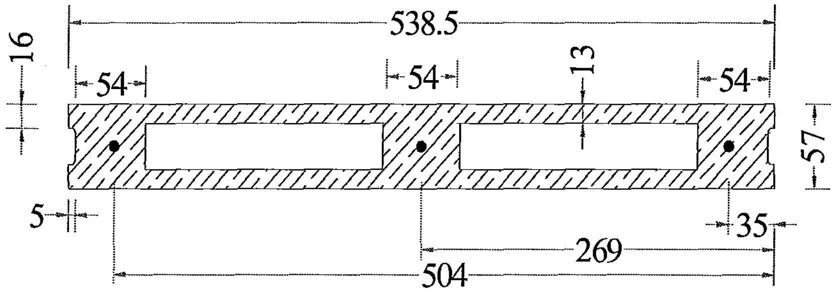

Figure A1.2: Three cell 3.66 mm diameter steel arrangement (hatched area, $A_m =$ 18,614 $mm^2$

**Reinforcement ratio**

$$\rho_v = \frac{3 * A_s}{A_e} = \frac{3 * 10.52\ mm^2}{18{,}614\ mm^2} = 0.17\%$$

**Axial stress**

$$\sigma_{net} = \frac{P_d}{A_e} = \frac{8755.425\ N}{18{,}614\ mm^2} = 0.47\ MPa$$

**Flexural strength**

$$\beta_1 = 0.8 - 0.1\left(\frac{27.8-20}{10}\right) = 0.722$$

$$P_d = C - \sum T$$

$$P_d = 0.85f'_m\,(b_w\beta_1 c) - 2 * A_s f_y - \left(\frac{34.8 - c}{c}\right)\varepsilon_u E_s A_s$$

$$c = 22.4\ mm$$

$$M_u = C\left(\frac{\ell}{2} - \frac{\beta_1 c}{2}\right) - T_1\left(\frac{\ell}{2} - 503.7\text{ mm}\right) - T_2\left(\frac{\ell}{2} - 34.8\text{ mm}\right)$$

$$M_u = 6.41\text{ kN} * \text{m}$$

$$V_u = \frac{5.49\text{ kN} * \text{m}}{1.16\text{ m}} = 4.75\text{ kN}$$

**First yield**

$$P_d = C - \sum T$$

$$P_d = 0.5f'_m\,(b_w kd) + A_{sc}f_y - A_{s1}f_y - A_{s2}f_y$$

$$\begin{aligned} P_d = 0.5\frac{E_m\varepsilon_s(kd)}{(503.7\text{ mm} - kd)} &* [(58.5\text{mm} * 57\text{ mm}) + 26\text{ mm} * (kd - 58.5)] \\ &+ 10.52\text{ mm}^2 * \left(\frac{34.8 - c}{503.7\ 0 - c}\right) * 393 - 10.52\text{ mm}^2 * 393\text{ MPa} \\ &- 10.52\text{ mm2} * \left(\frac{269.25 - c}{503.7\ 0 - c}\right) * 393\text{ MPa} \end{aligned}$$

$$kd = 83.18\text{ mm}$$

$$M_y = C\left(\frac{\ell}{2} - \frac{kd}{3}\right) - A_{sc}f_y\left(\frac{\ell}{2} - 34.8\text{ mm}\right) - A_{s1}f_y\left(\frac{\ell}{2} - 503.7\text{ mm}\right)$$

$$M_y = 4.52\text{ kN} * \text{m}$$

$$V_y = \frac{4.52\text{ kN} * \text{m}}{1.16\text{ m}} = 3.91\text{ kN}$$

**Sliding shear strength**

$$\begin{aligned} V_r &= \mu P_2 \\ &= 1.0 * [(0.9 * 8755.425\text{ N}) + (393\ MPa * 10.52\ mm^2)] \\ &= 12.01\text{ kN} \end{aligned}$$

**Shear diagonal strength**

$$V_r = (v_m b_w d_v + 0.25P_d)\gamma_g$$

$$= \left(\left(0.16\left(2 - \frac{M_f}{V_f d_v}\right)\sqrt{f'_m}\right) b_w * 0.8\ell_w + 0.25P_d\right)\gamma_g$$

$$= 9.26 \text{ kN}$$

**Initial stiffness and frequency**

$$I_{initial} = \text{Flanges of Wall} + 2 \text{ End Cells} + \text{Mid Cell} + 2 \text{ Transformed Steel}$$

$$I_{initial} = 464.708 \text{ x } 10^6 \text{ mm}^4$$

$$k_{initial} = \frac{1}{\Delta_f + \Delta_s} = \frac{1}{\frac{h^3}{3E_m I_{initial}} + \frac{1.2h}{0.4E_m A_e}}$$

$$\Delta_f = 0.000044594 \text{ mm/N}$$

$$\Delta_s = 0.000009745 \text{ mm/N}$$

$$k_{initial} = 18402.885 \text{ N/mm}$$

$$\omega_n = \sqrt{\frac{k_{intial}}{m}} = \sqrt{\frac{18402.885 \text{ x } 10^3 \text{ N/mm}}{892.5 \text{ kg}}} = 143.595 \text{ rad/s}$$

$$f_n = \frac{\omega_n}{2\pi} = 22.85 \text{ Hz}$$

**Cracked stiffness and frequency**

$$n = \frac{E_s}{E_m} = \frac{181955 \text{ MPa}}{16770 \text{ MPa}} = 9.2656$$

$$nA_s\left(\frac{d_1 - kd}{kd}\right)f'_m + nA_s\left(\frac{d_2 - kd}{kd}\right)f'_m = \frac{f'_m}{2}bkd$$

$$kd = 48.1 \text{ mm}$$

$$I_{cr} = \frac{b(kd)^3}{12} + bkd\left(\frac{kd}{2}\right)^2 + nA_s(d_1 - kd)^2 + nA_s(d_2 - kd)^2$$

$$I_{cr} = \frac{b(kd)^3}{3} + nA_s(d_1 - kd)^2 + nA_s(d_2 - kd)^2$$

$$I_{cr} = 27.10821 \text{ x } 10^6 \text{ mm}^4$$

$$k_{cr} = \frac{1}{\Delta_f + \Delta_s} = \frac{1}{\frac{h^3}{3E_mI_{cr}} + \frac{1.2h}{0.4E_mA_e}}$$

where $A_e = kd * 57$ mm

$\Delta_f = 0.000764466$ mm/N

$\Delta_s = 0.000066161$ mm/N

$k = 1203.9089$ N/mm

$$\omega_n = \sqrt{\frac{k_{cr}}{m}} = \sqrt{\frac{1203.9089 \text{ x } 10^3 \text{ N/mm}}{892.5 \text{ kg}}} = 36.7276 \text{ rad/s}$$

$$f_n = \frac{\omega_n}{2\pi} = 5.845 \text{ Hz}$$

**Cracking conditions**

$$M_{cr} = \left(\frac{f_t + f_{cs}}{y_t}\right) * I_{initial}$$

$$M_{cr} = 1.47 \text{ kN} * \text{m}$$

$$V_{cr} = \frac{1.47 \text{ kN} * \text{m}}{1.16 \text{ m}} = 1.27 \text{ kN}$$

### A1.1.3 Type III Wall

The reinforcement arrangement is presented for the two cell 4.76 mm diameter steel arrangement:

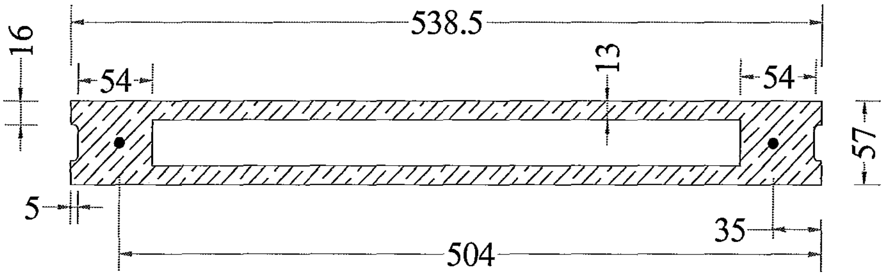

Figure A1.3: Two cell 4.76 mm diameter steel arrangement (hatched area, $A_m = 17{,}618\ \text{mm}^2$)

**Reinforcement ratio**

$$\rho_v = \frac{2 * A_s}{A_e} = \frac{2 * 10.52\ \text{mm}^2}{17{,}618\ \text{mm}^2} = 0.12\%$$

**Axial stress**

$$\sigma_{net} = \frac{P_d}{A_e} = \frac{8755.425\ \text{N}}{17{,}618\ \text{mm}^2} = 0.50\ \text{MPa}$$

**Flexural strength**

$$\beta_1 = 0.8 - 0.1\left(\frac{27.8 - 20}{10}\right) = 0.722$$

$$P_d = C - \sum T$$

$$P_d = 0.85 f_m' \left(b_w \beta_1 c\right) - A_s f_y - \left(\frac{34.8 - c}{c}\right) \varepsilon_u E_s A_s$$

$c = 24.5$ mm

$$\mathrm{M_u} = \mathrm{C}\left(\frac{\ell}{2} - \frac{\beta_1 \mathrm{c}}{2}\right) - \mathrm{T}\left(\frac{\ell}{2} - 503.7\ \mathrm{mm}\right) - \mathrm{T}\left(\frac{\ell}{2} - 34.8\ \mathrm{mm}\right)$$

$$\mathrm{M_u} = 6.92\ \mathrm{kN} * \mathrm{m}$$

$$\mathrm{V_u} = \frac{6.92\ \mathrm{kN} * \mathrm{m}}{1.16\ \mathrm{m}} = 5.97\ \mathrm{kN}$$

**First yield**

$$\mathrm{P_d} = \mathrm{C} - \sum \mathrm{T}$$

$$\mathrm{P_d} = 0.5\mathrm{f}'_{\mathrm{m}}\,(\mathrm{bkd}) + \mathrm{A_{sc}f_y} - \mathrm{A_sf_y}$$

$$\mathrm{P_d} = 0.5\frac{\mathrm{E_m}\varepsilon_{\mathrm{s}}(\mathrm{kd})}{(503.7\ \mathrm{mm} - \mathrm{kd})} * [(58.5\mathrm{mm} * 57\ \mathrm{mm}) + 26\ \mathrm{mm} * (\mathrm{kd} - 58.5)] + 17.80\ \mathrm{mm}^2 * \left(\frac{34.8 - \mathrm{c}}{503.7\ 0 - \mathrm{c}}\right) * 393 - 17.80\ \mathrm{mm}^2 * 516\ \mathrm{MPa}$$

$$\mathrm{kd} = 87.3\ \mathrm{mm}$$

$$\mathrm{M_y} = \mathrm{C}\left(\frac{\ell}{2} - \frac{\mathrm{kd}}{3}\right) - \mathrm{A_{sc}f_y}\left(\frac{\ell}{2} - 34.8\ \mathrm{mm}\right) - \mathrm{A_sf_y}\left(\frac{\ell}{2} - 503.7\ \mathrm{mm}\right)$$

$$\mathrm{M_y} = 6.41\ \mathrm{kN} * \mathrm{m}$$

$$\mathrm{V_y} = \frac{6.41\ \mathrm{kN} * \mathrm{m}}{1.16\ \mathrm{m}} = 5.55\ \mathrm{kN}$$

**Sliding shear strength**

$$\mathrm{V_r} = \mu \mathrm{P_2}$$

$$= 1.0 * (0.9 * 8755.425\ \mathrm{N})$$

$$= 7.88\ \mathrm{kN}$$

**Shear diagonal strength**

$$V_r = (v_m b_w d_v + 0.25P_d)\gamma_g$$

$$= \left(\left(0.16\left(2 - \frac{M_f}{V_f d_v}\right)\sqrt{f'_m}\right) b_w * 0.8\ell_w + 0.25P_d\right)\gamma_g$$

$$= 9.26 \text{ kN}$$

**Initial stiffness and frequency**

$I_{initial}$ = Flanges of Wall + 2 End Cells + 2 Transformed Steel

$$I_{initial} = 478.58 \text{ x } 10^6 \text{ mm}^4$$

$$k_{initial} = \frac{1}{\Delta_f + \Delta_s} = \frac{1}{\frac{h^3}{3E_m I_{initial}} + \frac{1.2h}{0.4E_m A_e}}$$

$$\Delta_f = 0.000043301 \text{ mm/N}$$

$$\Delta_s = 0.000010296 \text{ mm/N}$$

$$k_{initial} = 18657.6 \text{ N/mm}$$

$$\omega_n = \sqrt{\frac{k_{initial}}{m}} = \sqrt{\frac{18657.6 \text{ x } 10^3 \text{ N/mm}}{892.5 \text{ kg}}} = 144.58 \text{ rad/s}$$

$$f_n = \frac{\omega_n}{2\pi} = 23.01 \text{ Hz}$$

**Cracked stiffness and frequency**

$$n = \frac{E_s}{E_m} = \frac{206266 \text{ MPa}}{16770 \text{ MPa}} = 12.3$$

$$nA_s\left(\frac{d - kd}{kd}\right) f_{mgr} = \frac{f_{mgr}}{2} bkd$$

$$kd = 60.66 \text{ mm}$$

$$I_{cr} = \frac{b(kd)^3}{12} + bkd\left(\frac{kd}{2}\right)^2 + nA_s(d - kd)^2$$

$$I_{cr} = \frac{b(kd)^3}{3} + nA_s(d - kd)^2$$

$$I_{cr} = 50.709 \text{ x } 10^6 \text{ mm}^4$$

$$k_{cr} = \frac{1}{\Delta_f + \Delta_s} = \frac{1}{\frac{h^3}{3E_m I_{cr}} + \frac{1.2h}{0.4E_m A_e}}$$

where $A_e = kd * 57$ mm

$\Delta_f = 0.000408671$ mm/N

$\Delta_s = 0.000052462$ mm/N

$$k_{cr} = 2168.569 \text{ N/mm}$$

$$\omega_n = \sqrt{\frac{k_{cr}}{m}} = \sqrt{\frac{2168.569\text{x } 10^3 \text{ N/mm}}{892.5 \text{ kg}}} = 49.29 \text{ rad/s}$$

$$f_n = \frac{\omega_n}{2\pi} = 7.845 \text{ Hz}$$

**Cracking conditions**

$$M_{cr} = \left(\frac{f_t + f_{cs}}{y_t}\right) * I_{initial}$$

$$M_{cr} = 1.49 \text{ kN} * \text{m}$$

$$V_{cr} = \frac{1.49 \text{ kN} * \text{m}}{1.16 \text{ m}} = 1.29 \text{ kN}$$